Romero, Mary Jacquiline Romero (2012) *Orbital angular momentum entanglement.* PhD thesis.

http://theses.gla.ac.uk/3812/

Copyright and moral rights for this thesis are retained by the author

A copy can be downloaded for personal non-commercial research or study, without prior permission or charge

This thesis cannot be reproduced or quoted extensively from without first obtaining permission in writing from the Author

The content must not be changed in any way or sold commercially in any format or medium without the formal permission of the Author

When referring to this work, full bibliographic details including the author, title, awarding institution and date of the thesis must be given

Glasgow Theses Service
http://theses.gla.ac.uk/
theses@gla.ac.uk

Orbital Angular Momentum Entanglement

Mary Jacquiline Romero

MSc

Submitted in fulfilment of the requirements for the degree of

Doctor of Philosophy

School of Physics and Astronomy

College of Science and Engineering

University of Glasgow

December 2012

Abstract

Entanglement in higher dimensions is an attractive concept that is a challenge to realise experimentally. To this end, the entanglement of the orbital angular momentum (OAM) of photons holds promise. The OAM state-space is discrete and theoretically unbounded. In the work that follows, we investigate various aspects of OAM entanglement. We show how the correlations in OAM and its conjugate variable, angular position, are determined by phase-matching and the shape of the pump beam in spontaneous parametric down-conversion. We implement tests of quantum mechanics which have been previously done for other variables. We show the Einstein-Podolsky-Rosen paradox for OAM and angle, supporting the incompatibility of quantum mechanics with locality and realism. We demonstrate violations of Bell-type inequalities, thereby discounting local hidden variables for describing the correlations we observe. We show the Hardy paradox using OAM, again highlighting the nonlocal nature of quantum mechanics. We demonstrate violations of Leggett-type inequalities, thereby discounting nonlocal hidden variables for describing correlations. Lastly, we have looked into the entanglement of topological vortex structures formed from a special superposition of OAM modes and show violations of Bell-type inequalities confined to a finite, isolated volume.

Contents

List of Figures

List of Tables

Acknowledgements

The four years I have spent working in a dark laboratory (most of the time) has been very fruitful, and I owe much thanks to a lot of people. This is my small attempt at expressing my gratitude, I hope those I forget will not take offence!

To Synergy Scholarship, for providing me with the funds for my PhD.

To Miles, for his constant guidance in both the good days and bad days. It is difficult to imagine how our student-supervisor relationship could have been better. Needless to say, I have learned a lot from him.

To Steve, for all his sage advice, with and outwith physics. It is comforting to know that I can always go to Strathclyde if I need help on things I do not understand.

To Sonja, for being very supportive from the very beginning (from the time I first sent my email when I was still looking for a PhD position!). She is very much a model to me how I can be a good scientist and a good mother, too.

To Jonathan and Barry, for their patience in teaching me all I need to know experiment-wise. I could not have made it on my own without all those hours I spent with them in the dark!

To Kevin, for his initial help with the optical vortices.

To Daniele, for all his efforts maintaining our experiment and all his offerings to our deity (one just needs to look on our office board).

To everyone else I have had the honour of working with in my papers: Bob, Mark, Monika, Anand, Alison, Filippo, Dave, Melanie, Kiko, Lixiang and Andrew, it has been most rewarding.

To members of the Optics Group, past and present, for their worthwhile company, for providing emergency bits and bobs (when I needed them) and all the cakes and chocolates I am sure I do not need. I apologise for not listing names, as I am sure I will forget some, but you know who you are!

To my parents and sisters, for all their love and support, which I could very much feel regardless of the distance.

To Melo and Narra, for bringing change when I needed it. They are my constant reminder to smell the flowers (because they do, literally). Every day has a perfect ending because I have them.

To God, for the peace I will not find anywhere else, Ad majorem Dei gloriam.

Author's Declaration

I hereby declare that this thesis is the result of my own work, except where explicit reference is made to the work of others, and has not been presented in any previous application for a degree at this or any other institution.

Mary Jacquiline Romero

Publications

1. **Violation of a Bell inequality in two-dimensional orbital angular momentum state-spaces**, J. Leach, B. Jack, **J. Romero**, M. Ritsch-Marte, R. W. Boyd, A. K. Jha, S. M. Barnett, S. Franke-Arnold and M. J. Padgett, *Optics Express* **17** 8287 (2009)

2. **Holographic ghost imaging and the violation of a Bell inequality**, B. Jack, J. Leach, **J. Romero**, S. Franke-Arnold, M. Ritsch-Marte, S. M. Barnett, M. J. Padgett, *Physical Review Letters* **103** 083602 (2009)

3. **Entanglement of arbitrary superpositions of modes within two-dimensional orbital angular momentum state spaces**, B. Jack, A. M. Yao, J. Leach, **J. Romero**, S. Franke-Arnold, D. G. Ireland, S. M. Barnett, M. J. Padgett, *Physical Review A* **81** 043844 (2010)

4. **Quantum correlations in optical angle orbital angular momentum variables**, J. Leach, B. Jack, **J. Romero**, A. K. Jha, A. M. Yao, S. Franke-Arnold, D. G. Ireland, R. W. Boyd, S. M. Barnett, and M. J. Padgett, *Science* **329** 662-665 (2010)

5. **Violation of Leggett inequalities in orbital angular momentum subspaces**, **J. Romero**, J. Leach, B. Jack, S. M. Barnett, M. J. Padgett and S. Franke-Arnold, *New Journal of Physics* **12** 123007 (2010)

6. **Entangled optical vortex links**, **J. Romero**, J. Leach, B. Jack, M. R. Dennis, S. Franke-Arnold, S. M. Barnett and M. J. Padgett, *Physical Review Letters* **106** 100407 (2011)

7. **Bounds and optimisation of orbital angular momentum bandwidths within parametric down-conversion systems**, F. M. Miatto, D. Giovannini, **J. Romero**, S. Franke-Arnold, S. M. Barnett and M. J. Padgett, *European Physical Journal D* **66** 178 (2012)

8. **Determining the dimensionality of bipartite orbital-angular-momentum entanglement using multi-sector phase masks** , D. Giovannini, F. M. Miatto, **J. Romero**, S. M. Barnett, J. P. Woerdman and M. J. Padgett, *New Journal of Physics* **14** 073046 (2012)

9. **Increasing the dimension in high-dimensional two-photon orbital angular momentum entanglement**, **J. Romero**, D. Giovannini, S. Franke-Arnold, S. M. Barnett and M. J. Padgett, *Physical Review A* **86** 012334 (2012)

10. **Orbital angular momentum correlations with a phase-flipped Gaussian mode pump beam**, **J. Romero**, D. Giovannini, M. G. McLaren, E. J. Galvez, A. Forbes, and M. J. Padgett, *Journal of Optics* **14** 085401 (2012)

11. **Hardys nonlocality proof using twisted photons**, L. Chen and **J. Romero**, *Opt Express* **19** 21687 (2012)

Nothing is real.

–John Lennon

Chapter 1

Introduction

Entanglement is one of the most nonclassical manifestations of quantum mechanics, there is just no counterpart for it in classical mechanics. There is a great body of work on entanglement, most prominently concerning the two-dimensional state space of photon polarisation. We study entanglement in a much bigger playground by exploiting the orbital angular momentum of photons, which is theoretically infinite-dimensional. Entanglement in higher dimensions is rich, and as the work which follows will show, surprisingly accessible when explored with photon orbital angular momentum. Endowed with this potential, we just have to get smarter!

1.1 Quantum Mechanics, Entanglement and Nonlocality

The history of quantum mechanics would require a thesis in itself and I will not attempt to give a full account here, just enough to appreciate how successful and esoteric the theory still stands, more than one hundred years after its inception.

Quantum mechanics was born from the investigation of the black-body spectral distribution. The quantum hypothesis by Planck was no less than revolutionary [12]. It paved the way to Einstein's interpretation of the photoelectric effect, which gives us the first notions of a "light quantum," or naively, a wave behaving like a particle [13]. In 1924, de Broglie suggested the converse, that material particles can display wave-like behaviour and postulated a relationship between momentum and wavelength [14]. De Broglie's work inevitably led Schrödinger to develop quantum mechanics as we now know it, in which the energy levels are eigenvalues of a differential operator [15]. Schrödinger's theory, together with contributions from Born, Jordan and Dirac turned out to be successful in explaining the properties of the hydrogen and helium atoms, or in fact anything for which some potential function is known [16, 17]. However, the theory gives only probabilities, and is therefore inherently statistical.

The statistical nature of quantum mechanics led Einstein, Podolsky and Rosen (EPR) to ask the question "Can quantum-mechanical description of physical reality be considered complete?" in their landmark paper in 1935 [18]. We should emphasise that they were not questioning the correctness of

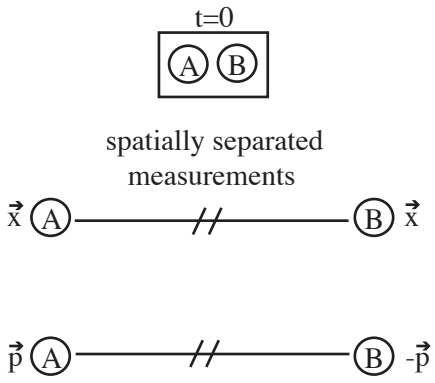

Figure 1.1: EPR states allows perfect correlations (anticorrelations) for two non-commuting observables such as position ($\vec{x}$) and momentum ($\vec{p}$).

quantum mechanics, only its completeness. In doing so, they gave the first description of entanglement, or as Einstein calls it, the "spooky action at a distance." They proposed an EPR state– two subsystems, A and B (fig. 1.1) which have interacted in the past and whose properties (e.g. position, momentum) remain correlated even if they have been spatially separated. The EPR state, although perfectly consistent with quantum mechanics, has been a challenge to implement in the laboratory, and experimental proofs of entanglement had to wait until later years [19]. Naturally, the focus of entanglement experiments is to show that correlations exist between the entangled systems, i.e., that one can predict the outcome of measurements on B based on knowledge of the properties of A, and vice versa. However, a more important point is that these correlations cannot be duplicated by any classical formalism, and entanglement is what is responsible for this inability [20]. The correlation in EPR states implies that the knowledge about the

whole system is maximal even if the knowledge about the individual subsystems is minimal. In a way, Schrödinger himself has hinted at the importance of separability in any definition of entanglement when he said, "The best possible knowledge of a whole does not include the best possible knowledge of its parts – and this is what keeps coming back to haunt us." Paraphrasing Schrödinger, entanglement is *the* departure from classical thought [21, 22].

For simplicity, we consider only pure states. Any pure state $|\Psi\rangle$ consisting of two subsystems A and B which can be written as

$$|\Psi\rangle = |u\rangle_A |v\rangle_B \tag{1.1}$$

where $|u\rangle$ and $|v\rangle$ are state vectors of A and B respectively, is *not* entangled [23]. For the state (1.1), we can write down a state for system A or system B alone, or we can think of it as "the property of system A is *separable* from system B." According to the superposition principle, any superposition of the sort of (1.1) is also an allowed state. For example, the state

$$|\Psi\rangle = \frac{1}{\sqrt{2}} \left(|u\rangle_A |v\rangle_B \pm |v\rangle_A |u\rangle_B \right) \tag{1.2}$$

is an allowed state. These superpositions, which can not be written as product states, are then entangled [23]. Due to the nature of the observed correlations in entangled systems (measurements are spatially separated yet measurement on one subsystem apparently affects measurement on the other) nonlocality is often discussed in connection with entanglement. However, nonlocality does not play any role in the definition of entanglement.

With entangled states being a reality in the laboratory, it transpires that

nature allows correlations of spatially separated observations. As a growing body of work has shown, shared randomness (which could have been established at the source of the entangled systems) is not enough for these correlations [19]. The correlations can exist even when the two systems are space-like separated. We call this counterintuitive phenomenon nonlocality, but we should distinguish it from entanglement [24]. Entangled systems, which are completely described in quantum mechanics exhibit nonlocality, but quantum mechanics is not the only nonlocal theory. There are alternative nonlocal theories [19] which have been tested, or are waiting to be tested (if indeed they are testable!).

Needless to say, entanglement and nonlocality are unsettling from the point of view of Newtonian mechanics. Determinism and locality are concepts so obviously true from our everyday experiences in the macroscopic world. It is not surprising that quantum mechanics, although a satisfactory description of entanglement and nonlocality, has been met with a lot of controversy. Alternative theories to quantum mechanics exist. However, theoretical predictions derived from quantum theory have been confirmed in various experiments, such that it is difficult to question its validity [19, 25]. The interpretation of quantum mechanics is another active area of research, which we will not discuss here. We simply adopt the mainstream interpretation that the wave function is a complete description of any physical system, and Born's rule gives the probability of measurement outcomes [26].

1.2 The photon

Maxwell's equations to describe electromagnetic fields, and later on, the quantum theory of radiation are successful in treating a variety of optical phenomena. The notion of a photon (the quantum of radiation) is neat, but unnecessary for most situations [27, 28, 29]. Interestingly, the name "photon" was coined by Lewis, a physical chemist, to refer to a physical particle which transfers radiation from one atom to another [30]. Although Lewis was mistaken, the name has caught on and the notion of photons albeit controversial, is here to stay.

Given that optics theory has its roots in the 17th-18th century (with treatises by Descartes and Newton, just to name a few), we have good control over light [31]. The ease with which we can generate and measure single photons nowadays makes photons an ideal system with which to explore entanglement. For example, polarisation can be easily measured with a polariser, or in our case, spatial modes can be easily measured with holograms. Photons do not interact with most systems (this also presents a limitation for some applications!) and this makes their entanglement resilient. Indeed, polarisation entanglement of photons has been shown over kilometer-range distances [32].

Photons are endowed with a number of properties. As examples, we can measure linear position or momentum [33], time of arrival or energy [34]. In this work, we focus on angular momentum, more specifically on orbital angular momentum. Although we frequently describe the angular momentum of light as arising from the spin angular momentum of the photon, the recognition of optical angular momentum does not rely on the notion

of the photon itself. In 1909 Poynting wrote about the wave motion of a revolving shaft and used mechanical analogies to establish that for circularly polarised light, the ratio of the optical energy to the angular momentum was equal to the angular frequency [35]. He even suggested a possible experiment to observe light's torque, where a stack of quarter-waveplates could extract angular momentum from the light as it was converted from circular to linear polarisation. A variant of this proposed experiment was actually performed in 1936 by Beth, who used polarised light from a tungsten bulb to set a quartz waveplate suspended from a quartz fibre into rotation [36]. Beyond these macroscopic experiments, light's angular momentum is apparent from the interaction of light with atomic and molecular systems. An atomic dipole transition implies a change of $\hbar$ in the angular momentum of the atomic state, necessitating that the emitted light carries this angular momentum away from the source. However, higher order transitions need more than $\hbar$, a quadrupole transition requires an angular momentum exchange of $2\hbar$ and hence we recognise that a single photon can carry an angular momentum in excess of $\hbar$. Drawing on analogies with both mechanical and electron systems, an early discussion of these questions was published in 1932 by Darwin (grandson of Charles Darwin). In that work, whilst recognising that a localisation of the photon is not allowed within the context of the uncertainty principle, Darwin suggested that angular momentum could be carried away by an emitted photon that is created (slightly) outside of the atom [37]. Within a ray optical picture, the angular momentum arises from the linear momentum of the light acting about a small radius vector of a magnitude of the order of the optical wavelength.

In the subsequent decades it seems that light carrying larger amounts of angular momentum was firmly associated with higher order atomic and nuclear transitions [38]. This understanding changed in 1992, when Allen et al. published their seminal paper establishing that laser beams with a helical phase carried an orbital angular momentum that was additional to, and independent of, that associated with spin angular momentum [39]. The subsequent generation of these helically-phased beams, and investigation of their mechanical effects [40, 41] have clearly established that, in the paraxial approximation, angular momentum can be separated into spin and orbital components [42].

1.2.1 Spin angular momentum

In questioning the completeness of quantum mechanics, EPR used the position and momentum of two particles. Their formulation inevitably involved states specified in terms of Dirac-delta functions which are not very amenable to experimental implementations. That the paradoxical situation that EPR proposed has been implemented in the laboratory owes much to the work of Bohm, who reformulated the EPR paradox in terms of spin [43]. Spin is usually imagined as a property of massive particles (e.g. electrons have a spin $\pm 1/2$). Spin however, is a property of wave fields and, as such, can also be attributed to photons even if they are massless [44].

Angular momentum comes from a circulating flow of energy in the electromagnetic field [44]. In particular, spin angular momentum (SAM) stems from the rotation of the electric field of light as the beam propagates. SAM has a value of $\sigma_z \hbar$ per photon, where σ_z is determined by the polarisation.

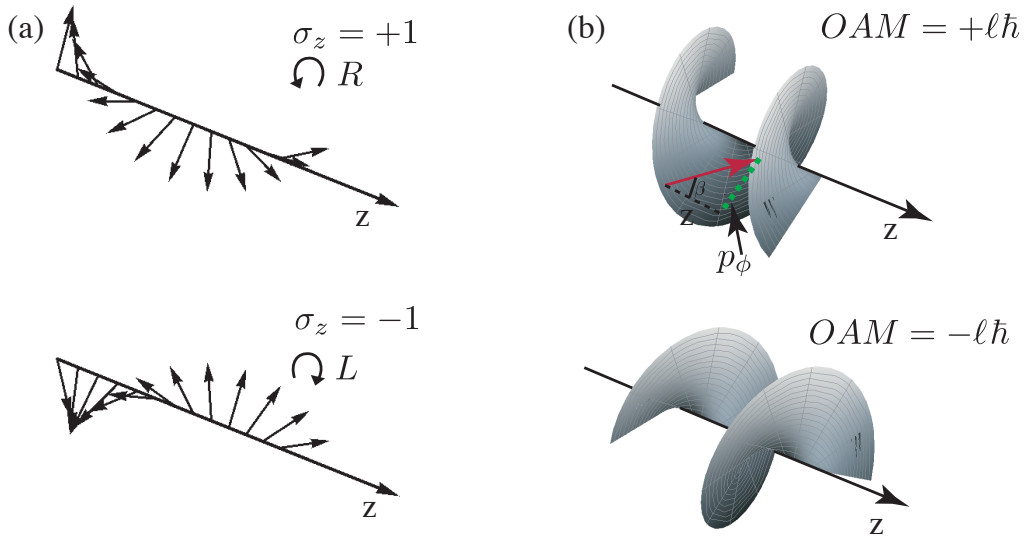

Figure 1.2: Spin angular momentum ($\sigma_z\hbar$) arises from the rotation of the electric field vector (a). By convention, a counterclockwise rotation is called right-circular (R) polarisation with $\sigma_z = 1$, while a clockwise rotation is left-circular (L) polarisation with $\sigma_z = -1$. Orbital angular momentum (OAM) arises from helical wave fronts, which can also be counterclockwise or clockwise leading to OAM of $+\ell\hbar$ or $-\ell\hbar$ respectively. The skew rays (red arrow, normal to the wave front and forming angle β with respect to z) leads to an azimuthal component in the linear momentum (green dotted line) leading to OAM in the $z-$direction. The magnitude of p_ϕ is biggest nearer the optical axis. Looking in the propagation direction, p_ϕ points in the counterclockwise (clockwise) direction for an OAM of $\ell\hbar$ ($-\ell\hbar$). [1]

Right- and left-circularly polarised light has $\sigma_z = +1$ and $\sigma_z = -1$ respectively [42, 40] (fig. 1.2.a). Any state of polarisation can be expressed as a superposition of right- and left-circular polarisations. Equal-amplitude superpositions correspond to linear polarisations, in which case $\sigma_z = 0$. The polarisation of light has played an important historical role in the experimental investigation of quantum entanglement [19]. It is also the degree of freedom which is most exploited for information-related applications such as quantum key distribution [45].

1.2.2 Orbital angular momentum

We can describe a light beam as a field amplitude, $u(x, y, z)$. For light beams propagating along z and having an $\ell-$dependent azimuthal phase, we can write,

$$u(x, y, z, \phi) = u_o(x, y, z)e^{-ikz}e^{i\ell\phi} \tag{1.3}$$

where ϕ is the azimuthal angle, ℓ is an integer, u_0 is a slowly varying amplitude distribution and k is the wave number. These beams are characterised by helical wave fronts, in contrast to the (nearly) planar wave fronts of laser beams (fig. 1.2.b). They appear in the solution to Maxwell's equations written in cylindrical coordinates– the Laguerre-Gaussian (LG_p^ℓ) family of modes.

This family of modes is defined by

$$\begin{aligned} \mathrm{LG}_p^\ell(r,\phi,z) &= \sqrt{\frac{2p!}{w^2(z)\,\pi(|\ell|+p)!}}\left(\frac{r\sqrt{2}}{w(z)}\right)^{|\ell|} L_p^{|\ell|}\left[\frac{2r^2}{w^2(z)}\right]\exp\left[\frac{-r^2}{w^2(z)}\right] \\ &\times \exp\left[i\ell\phi\right]\exp\left[\frac{ikr^2z}{2(z+z_R^2)}\right] \\ &\times \exp\left[-i(2p+|\ell|+1)\tan^{-1}(z/z_R)\right] \end{aligned} \tag{1.4}$$

where ℓ is the azimuthal mode index, p is the radial mode index, k is the wave number, $w(z)$ is the beam waist given by $w(z) = \sqrt{2(z^2+z_R^2)/kz_R}$, $z_R = kw^2(0)/2$ is the Rayleigh range, $L_p^{|\ell|}$ is the associated Laguerre polynomial, z denotes the distance from the beam waist and r, ϕ denote the transverse coordinates. The helical wave front leads to nonzero OAM. The helical wave front is not unique to LG beams. For example, higher-order Bessel beams [46] and Ince-Gaussian beams [47] have helical wave fronts too and hence carry orbital angular momentum. In this thesis we focus on the LG beams, with the understanding that OAM is not limited to this set.

More intuitively, OAM can also be deduced from a simple geometric argument based on the local ray directions. The local ray direction is, by definition, perpendicular to the wave front. It follows that for light of wavelength λ, at a radius r from the beam axis, the skew angle, β, of the ray is given by $\ell/(kr)$. This skew angle gives an azimuthal component of the linear momentum of the photon of $\ell\hbar/r$ which, when multiplied by the radius vector, gives an angular momentum per photon of $\ell\hbar$ (fig. 1.2.b). This is true for both the paraxial approximation and rigorous treatments via Maxwell's equations. There is no need to invoke any quantum theory to arrive at this

result [40].

Generation and measurement of photon OAM

LG beams were first produced using cylindrical lenses as mode converters [48] but can be made more easily with diffractive optical elements such as diffraction gratings. In 1990, Soskin and co-workers showed that diffraction gratings could be made containing an on-axis fork-singularity in the lines [49]. When the grating is illuminated with a Gaussian beam, the first-order diffracted beam contains a phase singularity accurately described by the $e^{i\ell\phi}$ phase dependence corresponding to helical wave fronts. However, at that time their angular momentum went unrecognised. The origin of this angular momentum is attributed to the fact that the resulting grating has more lines in one half of its area than the other half, and so the diffraction angles are different and hence the resulting beam contains skew rays.

Beams with nonzero OAM have also been created using precisely fabricated spiral phase plates which impart a helical phase front to the transmitted beam. Spiral phase plates are characterised by a phase edge dislocation of height s. This height depends on the OAM, such that $s = (\ell\lambda)/(n-1)$ where n is the refractive index of the plate (fig.1.3.a). The phase plate can also be realised holographically. Although the forked-gratings originally implemented by Soskin [49] were amplitude gratings, their diffraction efficiency can be dramatically improved if fabricated as a phase grating, where all the diffracted energy is directed to the first-order beam. The required phase cross-section $\Phi(x, y)$ of these forked gratings can be simply expressed as the modulo 2π addition of the azimuthal phase term with the linear phase term

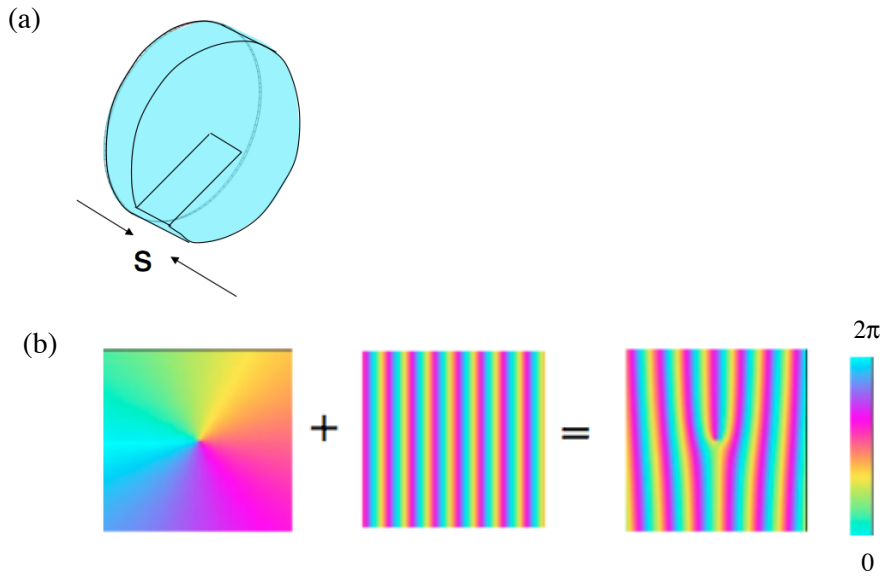

Figure 1.3: A Laguerre-Gaussian beam can be created by a spiral phase plate (a), or holographically by the addition of a spiral phase and a diffraction grating, shown here for the case of $\ell = 1$ (b). [2]

of a standard grating of pitch Λ, $\Phi(x, y) = (2\pi x/\Lambda) + \ell$ arctan2(y, x) (fig. 1.3.b). OAM beams of any desired order can be generated using these ℓ-forked diffraction gratings.

Operated in reverse, these ℓ-forked holograms can serve to detect the OAM of a laser beam. A helically phased beam incident on the hologram is converted back into a fundamental Gaussian beam that can be coupled via a single-mode fibre to a detector. Varying the order of the dislocation on the hologram allows one to determine the ℓ-index of the incident light (fig. 1.4). If the detector is sensitive to single photons then the combination of grating, fibre and detector is a mode-projector which allows the measurement of the ℓ-index of a single photon.

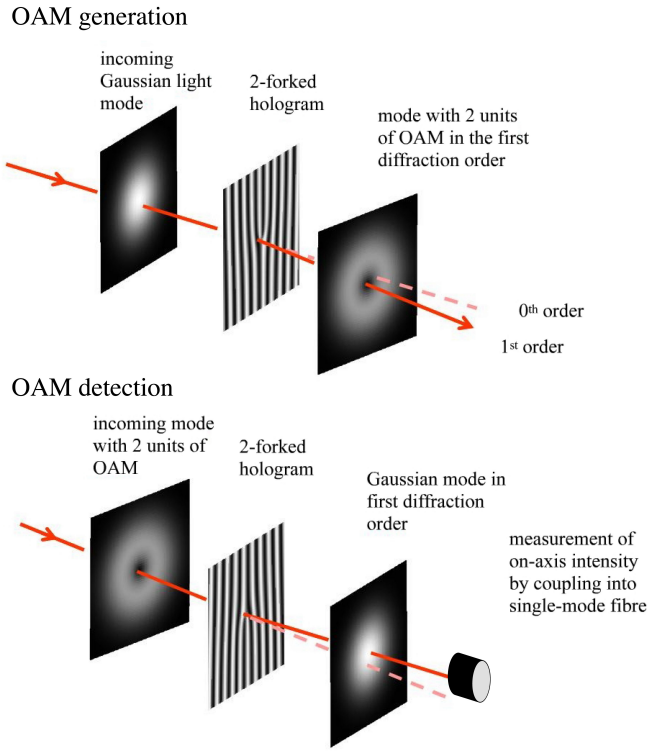

Figure 1.4: A forked diffraction grating can be used to generate a beam with a helical phase front in the first order diffracted beam, with the charge of the dislocation corresponding to the OAM of the generated beam. The reverse is also true, when a helically phased beam is incident on the hologram, the beam is transformed into the fundamental Gaussian mode, which can be coupled to a single mode fibre and a photon detector.

SAM vs OAM

Spin angular momentum (SAM) and OAM have different mechanical consequences. SAM causes a particle to spin about its own axis, whereas OAM causes a particle to rotate around the beam axis [50]. These mechanical effects have inspired optically driven manipulation and continue to be an active field [40, 41, 51].

A more obvious (but no less important) difference is that SAM is confined to a two-dimensional state-space, whereas OAM is not. The OAM quantum number, ℓ, is an integer, $-\infty < \ell < \infty$ and hence in theory the OAM state-space is infinite-dimensional. This has implications for entanglement and quantum information applications. Much attention has been directed to the two-dimensional state space of photon polarisation which provides both a conceptually and experimentally accessible playground. When quantum computation is discussed, it is almost always in terms of quantum bits (qubits) [20, 19, 45, 52, 53]. With OAM as a degree of freedom, D-dimensional entanglement is possible, wherein each photon is a D-level qudit taking on any of D possible values, and may prove to be an even more fertile playground.

High-dimensional entanglement and OAM

There is still much progress to be made in our understanding of high-dimensional entanglement, and on how we can put it to good use. From a fundamental standpoint, higher-dimensional entanglement implies stronger violations of locality [54, 55] and is especially useful in the study of mutually unbiased bases in higher dimensions [56]. More relevant to practical applications,

higher-dimensional entanglement provides increased security and robustness [57, 58, 59] and a higher information capacity [58, 60, 61]. As we shall discuss in more detail in the next chapter, entangled photon pairs typically come from the process of spontaneous parametric down-conversion (SPDC) in a nonlinear crystal. High-dimensional entanglement between these photon pairs can broadly be classified into two groups. The first exploits the spectral [62] and temporal [63] degrees of freedom; an experimental system with at least 11 dimensions has been achieved for the latter [63]. The second exploits the spatial degrees of freedom, such as transverse spatial profile [60], and transverse position and linear momentum [33, 59, 61]; an experimental system with a notable channel capacity of 7 bits/photon corresponding to roughly 128 dimensions has been reported for the latter [61]. We take the route which exploits the angular position and the orbital angular momentum to achieve high-dimensional entanglement.

The entanglement of orbital angular momentum (OAM) in photons generated via SPDC is firmly established theoretically and experimentally [64, 65]. In 2001, using the mode-projector consisting of a forked hologram and a single-mode fibre, Zeilinger and coworkers measured the OAM of single photons generated by SPDC [65] and investigated the entanglement of OAM. They used fixed holograms and were able to explore values up to $\ell = 2$. We have introduced a simple technological improvement: the use of programmable phase arrays in the form of spatial light modulators (instead of the fixed holograms). This has allowed us to do versatile measurements more easily including those that involve higher OAM states and OAM superpositions [5, 9, 11, 8]. The use of spatial light modulators has made the

infinite-dimensional state-space of OAM truly accessible.

1.3 Walkthrough

In all our experiments, we investigated the entanglement between photon pairs generated by SPDC. Chapter 2 is a closer look at the process of SPDC. SPDC is a reliable method of producing entangled photon pairs and has played a major role in making studies of entanglement more feasible in the laboratory. I describe our experimental setup in detail, including how we program the spatial light modulator to measure both intensity and phase modulations. Although there is an infinite range of values for OAM, only a finite subset of this is accessible in experiments. I characterise the OAM entanglement that is accessible to us in this chapter. We also look at measurements made in the conjugate variable to OAM, angular position, and confirm the well-known Fourier relationship between the two.

Chapter 3 is about tests of quantum mechanics done by measuring OAM. We draw analogies between polarisation (which has served as the usual testbed for quantum mechanics) and OAM. We also present the EPR paradox in OAM and angular position. Having established that entanglement exists (in the EPR sense), we test alternative theories which aim to explain the presence of correlations between the two photons of the entangled pair. We first test local hidden variable theories, as described by Bell [66, 67, 68]. We show a violation of a Bell-type inequality, thereby concluding that local hidden variables are not sufficient to explain the correlations that we observe. We also test local hidden variable theory without using inequalities. We

follow Hardy [69] and demonstrate a ladder version of the Hardy paradox, again supporting the incompatibility of locality with quantum mechanics. We then proceed to test nonlocal hidden variable theories, as described by Leggett [70]. We show a violation of Leggett-type inequalities, thereby concluding that nonlocal hidden variables are also not sufficient to explain the correlations that we observe.

Chapter 4 is on the entanglement of a more "exotic" spatial mode, in the form of loops of optical vortices that are linked together, called Hopf links. Hopf links can be generated by suitable superpositions of LG beams. We show that these can also be measured in the light coming from SPDC. Moreover, we show that these states are entangled by violating a Bell-type inequality, implying the entanglement of volumes within the electromagnetic field.

Chapter 5 is a summary of the work presented, and some possible exciting work for the future.

Chapter 2

Spontaneous Parametric Down-Conversion and Orbital Angular Momentum

Entangled photon pairs nowadays, are most conveniently generated by the nonlinear process of spontaneous parametric down-conversion (SPDC). Polarisation correlations between these photon pairs are well-exploited for studies of both the foundations and applications of quantum mechanics. Orbital angular momentum (OAM) has only recently been added to the repertoire of accessible photon properties for observing quantum correlations. We explore SPDC in the context of OAM correlations. Although the OAM state space is theoretically infinite-dimensional, only a range of OAM states can actually be generated and measured in experiments. The first experiment discussed in this chapter shows

how the range of OAM values can be increased by changing the phase-matching conditions. This translates to an increase in the information capacity of the entangled photons. The second experiment is a first step towards using more complex pump beam shapes for SPDC. We implement SPDC with a non-fundamental Gaussian beam, which allows us to redistribute both OAM and angular correlations.

J Romero, D Giovannini, S Franke-Arnold, S M Barnett, and M J Padgett, Phys. Rev. A 86, 012334 (2012)

J Romero, D Giovannini, M G McLaren, E J Galvez, A Forbes and M J Padgett, J. Opt. 14, 085401 (2012)

2.1 Spontaneous parametric down-conversion

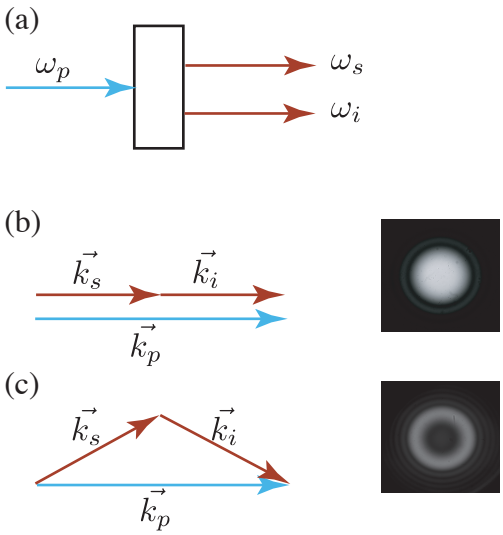

Figure 2.1: In SPDC, a pump photon of frequency ω_p spontaneously decays into two photons, of frequency ω_s and ω_i (a). In perfect collinear SPDC, the two photons are emitted parallel to the direction of the pump, and the down-converted light forms a bright spot surrounded by rings of decreasing intensity (b). In perfect noncollinear SPDC, the two photons are emitted with opposite transverse momentum, and the down-converted light is a bright central ring surrounded by rings of decreasing intensity.

Spontaneous parametric down-conversion (SPDC) is the elementary quantum process of a pump photon decaying into two lower-energy photons which are, by convention, called the signal and idler photons (fig. 2.1.a). This process has been described by Kleinman in 1968, where he describes SPDC as optical parametric noise [71]. Being a parametric process, the angular frequencies of the pump (ω_p) , signal (ω_s) and idler (ω_i) photons follow energy

conservation,

$$\omega_p = \omega_s + \omega_i. \tag{2.1}$$

The emission is greatest when the wave vectors of the pump ($\vec{k_p}$), signal ($\vec{k_s}$) and idler ($\vec{k_i}$) photons follow the conservation of linear momentum,

$$\vec{k_p} = \vec{k_s} + \vec{k_i}. \tag{2.2}$$

Equations (2.1) and (2.2) are collectively called the phase-matching conditions. Perfect phase-matching refers to situations in which these conditions are met. In our experiments, we consider only type-I SPDC. Here the signal and idler photons have the same polarisation, which is orthogonal to the pump polarisation. SPDC can be collinear, wherein the signal and idler photons are emitted in the same direction, parallel to the direction of the pump (fig. 2.1.b). Type-I collinear SPDC appears as a bright on-axis spot as in fig. 2.1.b. SPDC can also be noncollinear, wherein the signal and idler photons are emitted in different directions such that (2.2) is still satisfied. Type-I noncollinear SPDC appears as a bright annulus, such as in fig. 2.1.c and the signal and idler photons appear in diametrically opposite positions.

The entanglement of the signal and idler photons have not been explored in the early days of SPDC. However, the quantum mechanical picture of a pump photon splitting into two photons has been verified as early as 1970. Referring to SPDC as parametric fluorescence, Burnham and Weinberg observed the simultaneous detection (or coincidence, as it is now widely called in literature) of the signal and idler photons emitted by an ammonium dihydrogen phosphate (ADP) crystal [72]. However, a coincidence is recorded

only if the detectors were arranged such that they satisfy the conservation of energy and momentum. Despite this study, the majority of experiments on entangled photons in the 1970s and 80s were performed with photons created in cascade atomic decays [6, 52, 73]. Although these were largely successful in demonstrating entanglement by examining correlations in polarisation, the results are limited (and controversial!). This is because of the divergence in the emitted photons, which further aggravates the low detection efficiencies [74, 75]. As early as 1974, Clauser and Horne had hinted on the importance of correlations in direction in addition to correlations in spin to test local hidden variables conclusively [76]. Because of phase-matching, SPDC provides such directional correlation and the photons emitted by SPDC occur in very narrow cones. An experiment exploiting SPDC for producing polarisation-entangled photons was first implemented in 1988 by Shih and Alley using a deuterated potassium dihydrogen phosphate crystal [77]. Since this seminal experiment, SPDC has been exploited as a source of entangled photons, with measurements of phase, time-energy, linear position and momentum, and spatial modes including those with orbital angular momentum [33, 65, 78, 79, 80, 7]. SPDC is preferred because of the relative ease at which entangled photon pairs are generated by room-temperature crystals. SPDC has become even more ubiquitous with the developments in type-II SPDC (where the signal and idler have orthogonal polarisations) and ultrabright sources which have a high pair generation rate [81, 82, 83].

2.1.1 Two-photon state and conservation of OAM

Aside from a wealth of experiments, SPDC is well-studied theoretically. A rigorous treatment of the physical process can be attributed to Kleinman who derived the interaction Hamiltonian [71]. Zel'dovich and Klyshko studied the statistics of the fields and count rates in SPDC (or parametric luminescence, as it is called in their paper) as early as 1969 [84]. Hong and Mandel published a more detailed study in 1985, where they have derived both single and joint photon detection probabilities and shown that these two probabilities can equal each other [85]. A full theory is outside the scope of this thesis and we will skip the details of the quantisation. Instead we start with the result of [85], where the state generated in SPDC, $|\psi\rangle$ is written in terms of the wave vectors, and then follow the presentation in [86],

$$\begin{aligned} |\psi\rangle &= |\text{vac}\rangle + \text{const} \times \int d\mathbf{k_s} \int d\mathbf{k_i} \quad \text{sinc}\frac{1}{2}\left(\omega_s + \omega_i - \omega_p\right) t \\ &\quad \times \mathbf{F}(\mathbf{k_s}, \mathbf{k_i}) |1, \mathbf{k_s}\rangle |1, \mathbf{k_i}\rangle, \end{aligned} \tag{2.3}$$

where $|1, \mathbf{k_s}\rangle|1, \mathbf{k_i}\rangle$ denote the creation of one signal photon with wave vector $\mathbf{k_s}$ and one idler photon with wave vector $\mathbf{k_i}$, and $\mathbf{F}(\mathbf{k_s}, \mathbf{k_i})$ is,

$$\begin{aligned} \mathbf{F}(\mathbf{k_s}, \mathbf{k_i}) &= \int d\mathbf{q_p} \quad E(\mathbf{q_p}) \left[\frac{\omega_s \omega_i \omega_p}{n^2(\mathbf{k_s}) n^2(\mathbf{k_i}) n^2(\mathbf{k_p})}\right]^{1/2} \\ &\quad \times \quad \prod_{j=1}^{3} \text{sinc}\frac{1}{2}\left(\mathbf{k_s} + \mathbf{k_i} - \mathbf{k_p}\right)_j L_j. \end{aligned} \tag{2.4}$$

The transverse wave vectors of the pump are denoted by $\mathbf{q_p}$ ($\mathbf{q_s}$ and $\mathbf{q_i}$ are defined similarly), $E(\mathbf{q_p})$ is the angular spectrum of the pump, $n(\mathbf{k})$ are the

refractive indices, and L_j denote the length of the crystal in $\{x, y, z\}$. So that the time dependence disappears, we assume that the condition (2.1) holds. Experimentally, this is accomplished by using narrow-band interference filters before the detectors to ensure that we are measuring near degeneracy. We will also assume that the pump has a narrow angular spectrum, and the photon pairs are observed close to the z axis such that $|\mathbf{q}| \ll |\mathbf{k}|$ for the three wave vectors. The transverse momentum is conserved, $\mathbf{q_p} = \mathbf{q_s} + \mathbf{q_i}$, if the transverse size of the crystal is large enough. In addition, the refractive indices are slowly varying with $\mathbf{k}$ such that they can be treated as constants. From these conditions, we can write,

$$\mathbf{F}(\mathbf{k_s}, \mathbf{k_i}) \quad = \quad E(\mathbf{q_s} + \mathbf{q_i}) \quad \text{sinc}\left[\frac{1}{2}\left(k_{p,z} - k_{s,z} - k_{i,z}\right) L_z\right]. \qquad (2.5)$$

Examining the expression for $\mathbf{F}(\mathbf{k_s}, \mathbf{k_i})$, we can see that there are two factors that dictate the two-photon state: the angular spectrum of the pump and the phase-matching condition. Most treatments assume a thin crystal (hence the name "thin crystal approximation"), such that the width of the sinc function is much greater than the width of the pump beam angular spectrum [86, 87, 88], hence the sinc term goes to unity (note that the sinc term also goes to unity for the case of perfect phase-matching).

The conservation of angular momentum is expected because the Hamiltonian for SPDC is rotationally symmetric [85, 89]. However because optical OAM is not a true angular momentum, it is challenging to relate the symmetry to OAM conservation [89, 90]. Instead, it is the transfer of the angular spectrum of the pump and the phase-matching condition embodied in (2.5) which are often invoked to derive conservation of OAM [64, 86]. It is now gen-

erally accepted that OAM is conserved for collinear to near-collinear type-I SPDC. That is the selection rule,

$$m = \ell_s + \ell_i, \tag{2.6}$$

holds, where $m\hbar$ is the OAM per photon of the pump beam and $\ell_s\hbar$ and $\ell_i\hbar$ are the OAM of the signal and idler photons respectively. A complete derivation of this is presented in [91].

Any pure entangled state can be expressed in terms of a Schmidt decomposition [25, 92]. The Schmidt decomposition is not unique, and for our purpose, we will use the LG_p^ℓ basis ($|\ell, p\rangle$) to represent the OAM states. The two-photon state which satisfies (2.6) can be written as,

$$|\psi\rangle = \sum_{p_s=0}^{\infty}\sum_{p_i=0}^{\infty}\sum_{\ell=-\infty}^{\infty} c_{-\ell,p_i}^{\ell,p_s} |m-\ell, p_s\rangle |\ell, p_i\rangle . \tag{2.7}$$

Apart from the effect of our finite apertures, the measurements presented in this chapter are insensitive to the radial structure, and hence the radial index p. For simplicity we ignore $p_{s,i}$ in the meantime and write

$$|\psi\rangle = \sum_{\ell=-\infty}^{+\infty} c_\ell |m-\ell\rangle|\ell\rangle, \tag{2.8}$$

for the generated two-photon state. The probability of measuring photons in the states $|m-\ell\rangle$ and $|\ell\rangle$ is $|c_\ell|^2$.

2.1.2 Phase-matching

In SPDC experiments, the transverse profile of the pump is usually smaller than the cross-section area of the nonlinear crystal, such that we can let L_x and L_y approach infinity. In this way, the process is invariant to transverse translations and conservation of transverse linear momentum holds. However, the crystal has a finite length which makes the process *not invariant* to translations along z. The difference in the $z-$components of the wave vectors, which appears in the argument of the sinc function in (2.5), is called the on-axis phase mismatch Δk_z,

$$\Delta k_z = k_{p,z} - k_{s,z} - k_{i,z}. \tag{2.9}$$

The on-axis phase mismatch (fig. 2.2) determines the efficiency in which a three-wave mixing process will occur. In second harmonic generation, $2\pi/\Delta k$ is regarded as the coherence length over which the driving and the harmonic fields remain in phase, and hence dictates the efficiency. SPDC is also most efficient (brightest) when $\Delta k_z = 0$, but more importantly for us, Δk_z determines the spectral distribution of the down-converted photons [71, 93, 94]. Theoretical treatment of phase-matching is complicated and several approximations have been made [95, 96, 97], but it is easy to do in practice, either by tuning the temperature or angular orientation of the crystal [93]. In the case of our bulk crystal, changing the angular orientation changes the index of refraction for the pump beam, and hence Δk_z. A full characterisation of SPDC for any phase-matching condition is nontrivial, details and a numerical program can be found in [98].

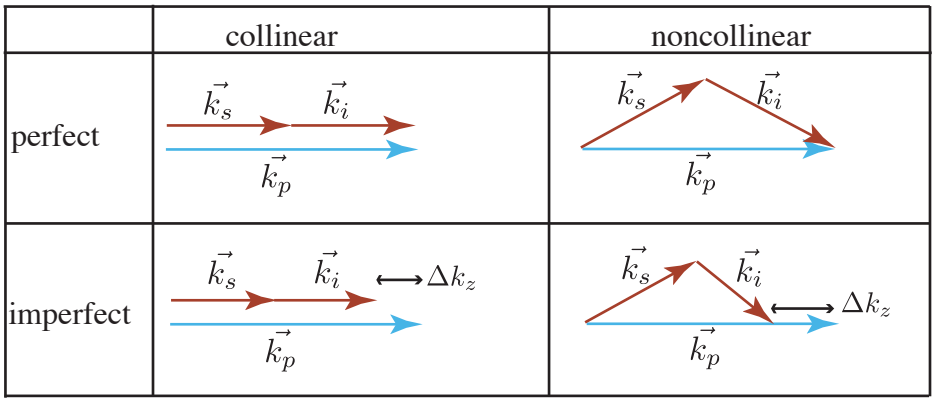

Figure 2.2: The efficiency of SPDC, like any other three-wave mixing process, depends on phase-matching. In addition, in SPDC, the on-axis phase mismatch determines the spectral distribution of the signal and idler photons. Here we show the different phase-matching scenarios. Emission is inhibited when $\Delta k_z L_z$ is a multiple of 2π, and the most significant emission occurs when $\Delta k_z L_z = 0$.

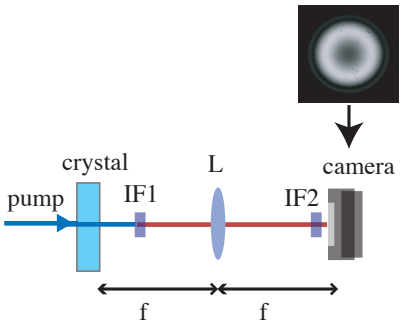

Figure 2.3: The phase-matching in SPDC can be derived by capturing the far-field intensity (inset) of the down-converted light, at the focal plane of a lens, L. The intensity pattern is fitted with (2.10) and we use α as a phase-matching parameter, with $\alpha = 0$ corresponding to collinear SPDC. (IF1- interference filter to filter out the pump, IF2-interference filter to select photon pairs)

The effect of phase-matching is readily observable in the structure of the down-converted light in the far-field, where only phase-matching and pump divergence matters [99]. The intensity profile I in the far-field of the crystal (fig. 2.3) mirrors the sinc phase-matching term in (2.5) and can be fitted with the function,

$$I(r) = \text{sinc}^2\left(\frac{ar^2}{f^2} + \alpha\right) \tag{2.10}$$

where r is radial coordinate in the focal plane of a lens with focal length f, $\alpha = (|\mathbf{k}_p| - |\mathbf{k}_s| - |\mathbf{k}_i|)L/2$ is a phase-matching parameter which determines the opening angle of SPDC, and $a = (|\mathbf{k}_s| + |\mathbf{k}_i|)L/4n^2$, where n is the refractive index for the signal and idler wavelengths and L is the crystal length [100]. Because the transverse momentum of the photons is conserved, α is dominated by Δk_z, and α can be taken as a measure of the on-axis phase

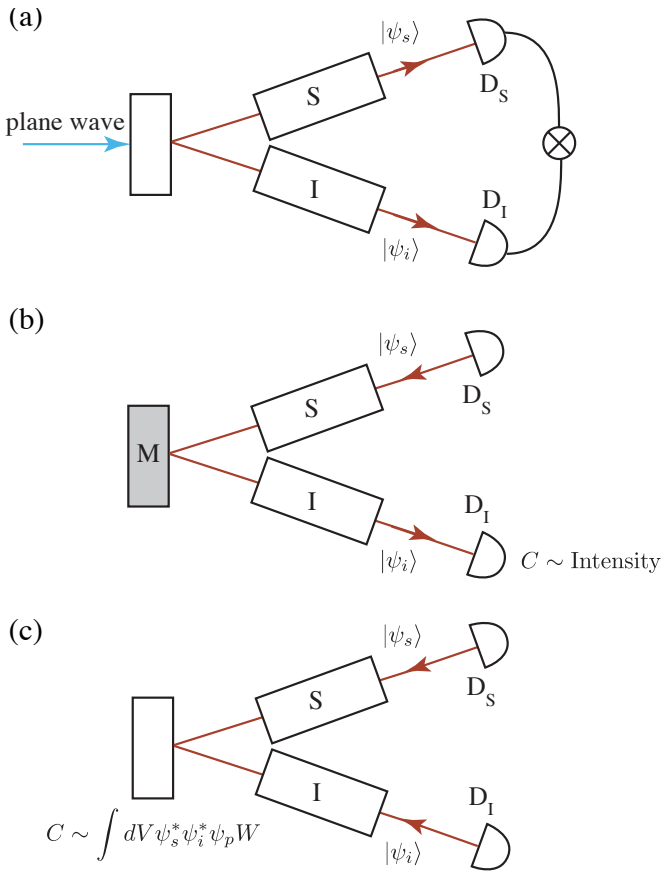

Figure 2.4: A generic experiment scheme where states ψ_s and ψ_i are measured from the photons generated in SPDC is shown in (a). S and I represent the optical train from the crystal to the detectors. If the pump is a plane wave and phase-matching is perfect (nearly perfect), the coincidences can be predicted by using the Klyshko picture (b). D_S is taken to be a source of $|\psi_s\rangle$, this state is propagated through S and reflected off the crystal which is now treated as a mirror (M). It is then propagated through I, and the coincidence probability is taken to be proportional to the intensity at D_I. A more general treatment which can take into consideration both crystal length and phase-matching is the "double Klyshko" picture (c). Both detectors D_S and D_I are taken to be sources of ψ_s and ψ_i, respectively. These modes are propagated through S and I onto the facet of the crystal. At the crystal, these resulting modes are propagated together with the pump mode, ψ_p and any phase-matching function W. The coincidence probability is taken to be proportional to a volume integral.

mismatch with $\alpha = 0$ corresponding to the collinear case. In the next section, we will exploit phase-matching to increase the number of OAM states that can be measured in our SPDC experiment.

2.1.3 Klyshko picture

Given a two-photon state $|\psi\rangle$, the joint probability $P(\psi_s, \psi_i)$ of detecting the signal and idler photons in the states $|\psi_s\rangle$ and $|\psi_i\rangle$ respectively can be calculated as,

$$P(\psi_s, \psi_i) = |\langle\psi_i|\langle\psi_s|\psi\rangle|^2. \tag{2.11}$$

The joint probability is proportional to the coincidences and is the quantum mechanical prediction of the measurement outcomes [26].

Klyshko formulated a different approach to predicting measurement outcomes, in what is referred to as the Klyshko picture [101]. The Klyshko picture is formalised in retrodictive quantum theory, in which the state of the quantum system at any time between preparation and measurement is the measured state evolved backward in time [102, 103]. We will avoid that formalism here, it will suffice to say that the simplicity of the Klyshko picture also arises from a rigorous (albeit uncommon) formulation of quantum mechanics [104].

Experimentally, a measurement of $\psi_s(\psi_i)$ would entail various components (polarisers, lenses, holograms etc. - denoted as boxes S and I in fig. 2.4) downstream from the nonlinear crystal terminating on detectors $D_s(D_i)$. To predict the coincidence, Klyshko proposed "back-propagating" from one detector to the other, treating the crystal as a mirror (provided that the pump

is plane wave and phase-matching is satisfied). The system can be modelled as follows: the detector D_s is replaced by a source of photons in state $|\psi_s\rangle$, this mode is propagated through the components in the signal arm, gets reflected at the nonlinear crystal, and continues to propagate through the components in the idler arm and finally to D_i. The intensity of this "propagated" mode at D_i is proportional to the expected coincidences. This is a simple picture which has been verified by various experiments, most notably by ghost imaging experiments wherein a two-photon analogue to geometric optics has been derived [105, 106].

Taking phase-matching (and even the finite thickness of the crystal) into consideration in the context of the Klyshko picture is largely unexplored since for most cases, the simple picture of the crystal taken as a mirror is sufficient. A naive possibility is to take the crystal as a thick diffraction grating, but this is yet to be done and verified experimentally. Instead, there is a "double-Klyshko" picture to account for phase-matching and crystal length [107]. Here, the detectors (which are in transverse positions r_s and r_i) are replaced by sources of states $|\psi_s\rangle$ and $|\psi_i\rangle$. These modes are propagated through their respective arms, as in the Klyshko picture to the facet of the crystal. The joint probability of measuring $|\psi_s\rangle$ and $|\psi_i\rangle$ is then calculated from a volume integral in the crystal, through which the three fields (including the pump mode ψ_p) are propagated and multiplied by the phase-matching function W, as in

$$P(r_s, r_i) \sim \int_{-L/2}^{L/2} dz' \int_{-\infty}^{+\infty} dr' \psi^*_{s,prop}(r', z') \psi^*_{i,prop}(r', z') \psi_p(r', z') W(z') \tag{2.12}$$

where we refer to the "back-propagated" signal(idler) modes as $\psi_{s,prop}(\psi_{i,prop})$. An exact expression which incorporates the on-axis phase-mismatch for the case where the detection modes are Gaussian ($\ell = 0$) have been derived using this [107, 108]. However, it has not been done for the Laguerre-Gaussian detection family of modes, which is most relevant to us. For most of the results we present in this thesis, the quantum mechanical prescription of (2.11) is enough to describe our results. We use the Klyshko picture to optimise our detection system instead, as we will discuss later.

2.2 Experimental apparatus

Before I embark on describing experiments, I will first present our general experiment schematic. The experiments discussed in this thesis were done over a period of four years. Over those four years, some details of the setup have been modified, but the general schematic remains the same. We have a source of entangled photons and a way of measuring the spatial mode of the photons (fig. 2.5.a.). Our photons come from SPDC in a β-barium borate (BBO) crystal pumped by a 355 nm quasi-CW source. The photons are separated and goes through two identical arms. The output facet of the crystal is imaged onto spatial light modulators (SLM, from Hamamatsu). The SLM specifies the state that we aim to measure. The SLM is imaged onto one end of a single mode-fibre (SMF). The SMF is connected to a silicon avalanche photodiode (APD, Perkin Elmer), the output of which is fed to a coincidence circuit (fig. 2.5.b). The experiment setup will be sketched for each of the experiments presented in this thesis, but it is useful to keep this

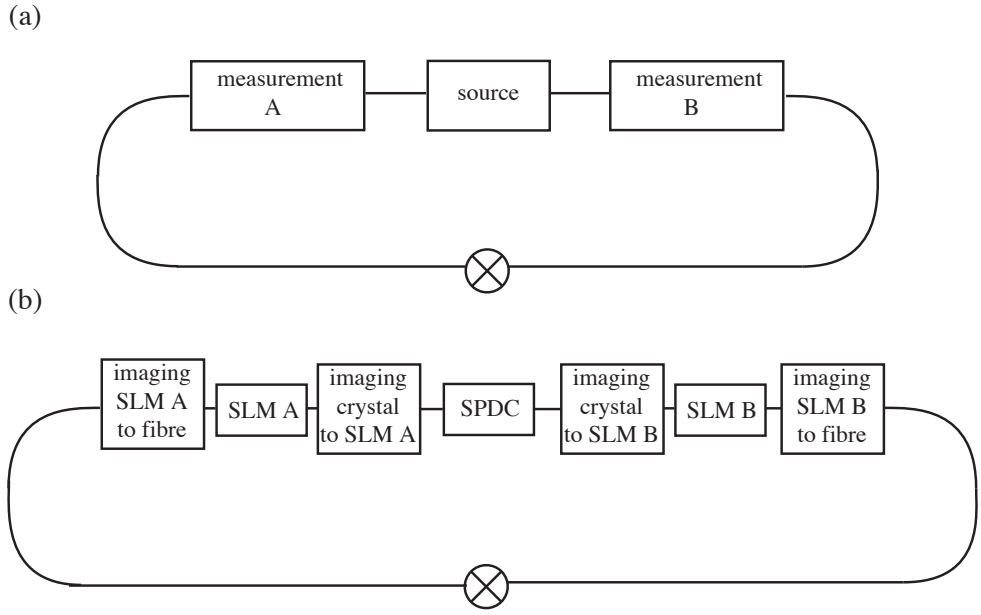

Figure 2.5: A general picture of an experiment with two photons consist of a two-photon source and a measurement arm for each of the photons (a). In our experiments, the photons come from SPDC in a nonlinear crystal. The measurement consists of imaging the crystal onto the SLMs, and the SLMs onto the single mode fibres, which are then coupled to the single photon detectors. The output of the detectors are fed to a coincidence counting circuit (b).

general scheme in mind.

One important technological improvement that our group has introduced is the use of SLMs. The first experiments on OAM entanglement employed fixed holograms [65, 109], which although effective, are not very flexible. Introducing an SLM to measure the spatial mode has made our experiment very versatile, we can measure not only OAM, but any OAM superposition or in fact, any spatial mode. Being a reconfigurable element in the image

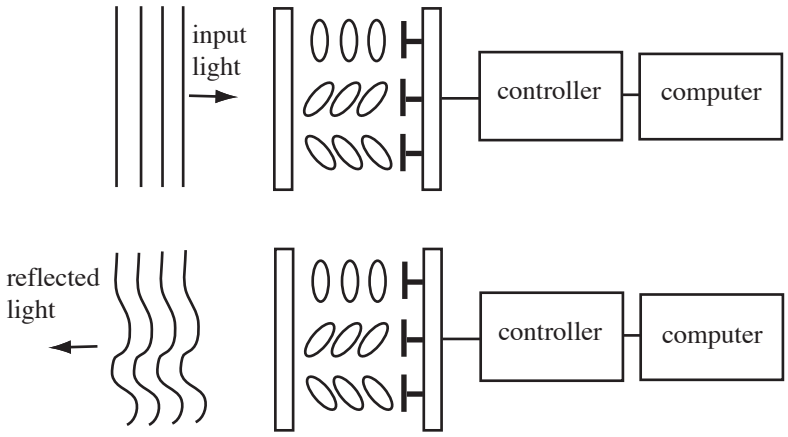

Figure 2.6: A spatial light modulator is an array of liquid crystals on top of a chip which controls the voltage. The change in orientation of the liquid crystals brings about varying optical path difference across the input beam. This results to a tailored phase profile in the reflected light.

plane (in which the angle and transverse positions are decoupled) of both the crystal and SMF, the SLM also makes alignment of our setup more convenient. The angle of the diffraction grating and the position of the fork in grating can be modified just by software, in contrast to physically aligning a fixed hologram.

Our SLM consists of an array of liquid crystals on top of a silicon chip. Depending on the voltage across the liquid crystal, the liquid crystal changes orientation, hence introducing a spatially varying phase delay on the reflected light (fig. 2.6). The SLM allows us to specify any phase from 0 to 2π as grayscale values 0 to 255. Any arbitrary phase structure can be measured. Forked gratings such as those in fig. 1.3.b, can be easily implemented to

measure OAM.

The power that goes to the first order can be varied by changing the grayscale contrast of the blazed diffraction grating. At the outset, we have made a calibration curve which consists of the single channel counts as a function of grayscale contrast. In this way, by changing the grayscale contrast, we can measure not just spatial modes with a phase modulation, but also those that have an amplitude modulation (if one is willing to incur additional loss). In general if we want to measure a spatial mode with phase $\Phi(x, y)$ and amplitude $A(x, y)$, we can calculate the phase that we will encode in the SLM, $\Phi_{\text{holo}}(x, y)$,

$$\Phi_{\text{holo}}(x, y) = [\Phi(x, y) + \Phi_{\text{grating}}(x, y)]_{\text{mod}2\pi} \times \text{D}(A(x, y)). \tag{2.13}$$

The phase $\Phi_{\text{grating}}(x, y)$ refers to the diffraction grating used to direct the light to the first order. The distortion function, $\text{D}(A(x, y))$, which depends on the amplitude can be derived from the lookup table, but ideally can also be calculated from the relationship,

$$\text{sinc}\left[\pi(1 - \text{D}(A(x, y)))\right] = A(x, y). \tag{2.14}$$

which could be numerically evaluated [110, 111].

Although SLMs introduce a significant degree of flexibility, they also introduces a significant loss. This is not ideal if one is trying to beat the fair sampling loophole (the assumption that the photons that we can measure with our limited detection efficiency is a representative sample of all the photons). Our SLMs have a ballpark diffraction efficiency of 60% and our

APDs have a quantum efficiency of 60% at 710 nm (with a dark count of 200 s^{-}1). We are nowhere near the limit to close the fair sampling loophole (66.7% overall efficiency with a reasonable background [112]).

2.3 Fourier relationship between OAM and angular position

The relationship between OAM and angular position is a recurring theme in this thesis so we will clarify their relationship in this section. Physical properties of a cylindrical system are periodic functions of an angular position, results of measurements on angles differing by 2π are the same. An angular position corresponds to an azimuthal angle, ϕ. The difference between angular positions ϕ_1 and ϕ_2, is denoted by $\Delta\phi = \phi_2 - \phi_1$, and corresponds to a physical difference in orientations (relative orientation, or a rotation). This angle should not be confused with the phase difference. The phase difference arising from a rotation is $\ell-$ dependent, because of the symmetry introduced by ℓ, and is equal to $\ell\Delta\phi$. A phase difference, however, is not exclusively brought about by rotation, for example, it can also arise from propagation or reflection off a material.

More formally, if we take $|\Phi_1\rangle$ as the state at orientation ϕ_1 and $|\Phi_2\rangle$ as the state after being rotated by $\Delta\phi$ about the z-axis (denoted by the OAM operator $\hat{L}_z$), then we can write

$$|\Phi_2\rangle = \exp(i\hat{L}_z\Delta\phi)|\Phi_1\rangle. \tag{2.15}$$

We can rewrite this as,

$$\exp(i\hat{L}_z\Delta\phi)\Phi(\phi_1) = \Phi(\phi_1 + \Delta\phi), \tag{2.16}$$

and if we compare with a Taylor expansion,

$$\exp\left(\Delta\phi\frac{\partial}{\partial\phi}\right)\Phi(\phi_1) = \Phi(\phi_1 + \Delta\phi), \tag{2.17}$$

we see that $\hat{L}_z$ has the form,

$$\hat{L}_z = -i\frac{\partial}{\partial\phi}. \tag{2.18}$$

That is to say, $\hat{L}_z$ is a generator of rotations and hence OAM and angular position are conjugate variables [113, 114].

Angular position is periodic, but one can choose any 2π interval from ϕ_0 to $\phi_0 + 2\pi$, where ϕ_0 is the reference angular position. In our experiments, we are mostly concerned with relative orientations, which is independent of ϕ_0 (ϕ_0 becomes important for angle operators [115], but this is outside our scope). It is also possible to measure the azimuthal position of a single photon. As a simple example, a narrow angular aperture (a 'cake slice') can be used to determine azimuthal position, in the same way that a slit can measure linear position. The central angle of the angular aperture can be rotated, and the number of photons that pass through the aperture as a function of the aperture's orientation is taken as a measure of the probability distribution of the angular position [116].

Intuitively, if the angular probability distribution is uniform, one has

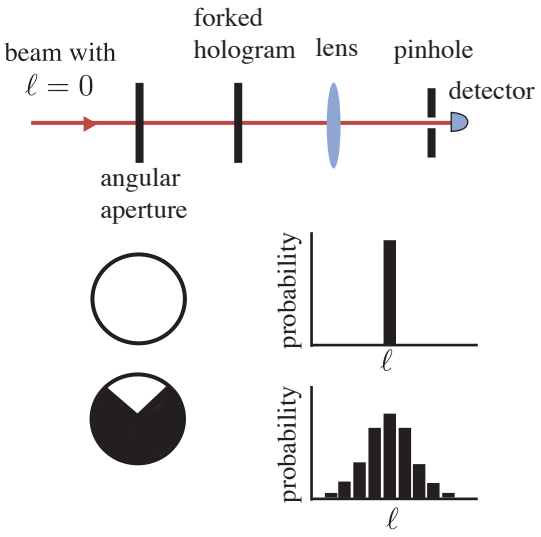

Figure 2.7: The conjugacy between OAM and angular position can be demonstrated by passing a beam of specific OAM ($\ell = 0$ in this case) through an angular aperture and analysing the OAM content of the transmitted beam. This is done by varying the ℓ-value of the forked hologram and measuring the amount of light that goes through the pinhole. If there is no angular aperture, the measured OAM of the beam is the same as the OAM of the input beam. If there is an angular aperture, the measured OAM is spread over multiple OAM states.

access to the whole angular aperture (i.e. unobstructed field of view) and therefore the OAM can be determined with certainty. As the angular probability distribution narrows (corresponding to a 'cake slice', hence some part of the beam is obstructed), the OAM can not be determined with certainty, and this results to a spread in the possible OAM values (fig. 2.7). The complementarity results to an uncertainty relation between OAM and angle, analogous to that of linear position and linear momentum, and this will be alluded to in the next chapter when we discuss the Einstein-Podolsky-Rosen paradox.

From complementarity, we can also write the probability amplitudes of the angular states in terms of the OAM probability amplitudes [116, 117],

$$\psi(\phi) = \frac{1}{\sqrt{2\pi}} \sum_{\ell=-\infty}^{+\infty} \psi_\ell \exp(i\ell\phi), \tag{2.19}$$

and the OAM probability amplitudes in terms of the angular probability amplitudes,

$$\psi(\ell) = \frac{1}{\sqrt{2\pi}} \int_{-\pi}^{\pi} \psi(\phi) \exp(-i\ell\phi). \tag{2.20}$$

We will exploit this Fourier relationship in the two succeeding experiments.

Note: I will now begin describing our experiments. I discuss the experiments in this thesis, not in the order that they were done, but rather in the order which makes most sense (to me, at least). The next two sections are the most relevant to SPDC, hence I discuss them first, but they were the last two experiments that I have done.

2.4 Increasing the dimensionality in OAM entanglement

The OAM quantum number ℓ is theoretically unbounded, $-\infty < \ell < \infty$. However, owing to our finite pump, crystal and aperture sizes, we can only access a subset of this high-dimensional state space. Higher dimensions in entangled systems are desirable for stronger violations of locality [54, 55], for increasing security and robustness in quantum communications [57, 58, 59], and for increasing the information capacity of a photon [58, 60, 61]. In this section, we will discuss how we can expand the range of OAM modes available for experiments.

2.4.1 Spiral bandwidth and dimensionality

The term "spiral bandwidth" is often used within the OAM community in different contexts and so it is imperative to discuss what it means to avoid confusion. The number OAM modes (in our case, we take it as those within the full width at half-maximum) is generally referred to as the spiral bandwidth [118], and the range of OAM modes and their respective weightings is referred to as the spiral spectrum. The *generation* spiral bandwidth is the number of OAM modes that is produced by SPDC. The generation spiral spectrum of SPDC has previously been calculated analytically from the coincidence fringe obtained from a clever angular equivalent of the Hong-Ou-Mandel interferometer using bucket detectors [119]. Measuring the generation spiral spectrum is essentially recovering the Schmidt decomposition in (2.8). As such, the term "Schmidt number", K, is often used in conjunction with the genera-

tion spiral spectrum. Because we are only interested in the OAM modes and ignoring the radial part, we focus on the azimuthal Schmidt number, K_{az}. Mathematically, K_{az} can be derived from (2.8), $K_{az} = 1/\sum_\ell |c_\ell|^4$ [95, 119]. The total Schmidt number, K and K_{az} are related as, $K_{az} = 2\sqrt{K}$ [120].

On the other hand, the *measurement* spiral bandwidth is the number of OAM modes that can be measured. It depends on the generation spiral bandwidth and detection capability of the system. The measurement spiral spectrum has been derived for the collinear case in [88, 91]. We focus on the measurement spiral bandwidth, since it dictates the number of usable OAM modes. Any projective measurement of OAM, wherein the OAM of the signal and idler photons are directly measured using a mode-transformer (with a hologram or phase plate) and a single-mode fibre coupled to a photon-detector, is inherently sensitive to the radial field distribution [11, 119, 121]. Measuring the OAM spectrum in this manner will inevitably result in a spiral bandwidth that is different from the generation bandwidth [119]. Pors et al. have calculated the dimension D from coincidence fringes as angular phase plate analysers are rotated: D is the inverse of the area under the peak-normalised coincidence fringe [122]. Using this technique, a dimensionality of $D = 6$ has been measured for an SPDC system with a Schmidt number of 31. Another technique is to measure the OAM states of the signal and idler photons directly by forked diffraction holograms and build up a measurement spiral spectrum, as was done by Dada et al. in [55], where they have shown 11-dimensional OAM entanglement via generalised Bell inequalities. Using angular slits and forked diffraction holograms, Leach et al. successfully demonstrated the Einstein-Podolsky-Rosen (EPR) paradox by

measuring angular position and 15 different OAM states, although they did not obtain the dimensionality of the measured OAM entanglement [5].

In this section, we quantify the dimensionality of OAM entanglement in two ways. First, we fit our measured spiral spectrum with a Lorentzian function and simply obtain the half-width. Second, we compute the quantum mutual information capacity - the information that is shared by the entangled photons. This is an especially meaningful quantity for quantum key distribution (QKD) [61, 123, 124], and has not been measured for OAM previously.

2.4.2 Experiment and results

To increase the number of measurable OAM modes, one can either optimise the detection system or widen the OAM spectrum of the generated two-photon state. These two are equally important, but optimising detection is fruitless if the OAM states are not being generated in the first place. The detection geometry is more often fixed but can be designed optimally, as we will describe later. The generation bandwidth can be modified by changing the characteristics of the pump beam [96, 125], or by tuning the phase-matching conditions as shown previously by temperature tuning a periodically poled potassium titanyl phosphate (PPKTP) crystal [119]. We adopt the latter, and demonstrate the effect of phase-matching in our bulk crystal to both the OAM and angular position correlations.

Our entangled photons are generated from a 5-mm long beta-barium borate (BBO) crystal cut for type-I collinear SPDC pumped by a collimated 355 nm pump beam (fig. 2.8). The pump beam is blocked by a longpass filter

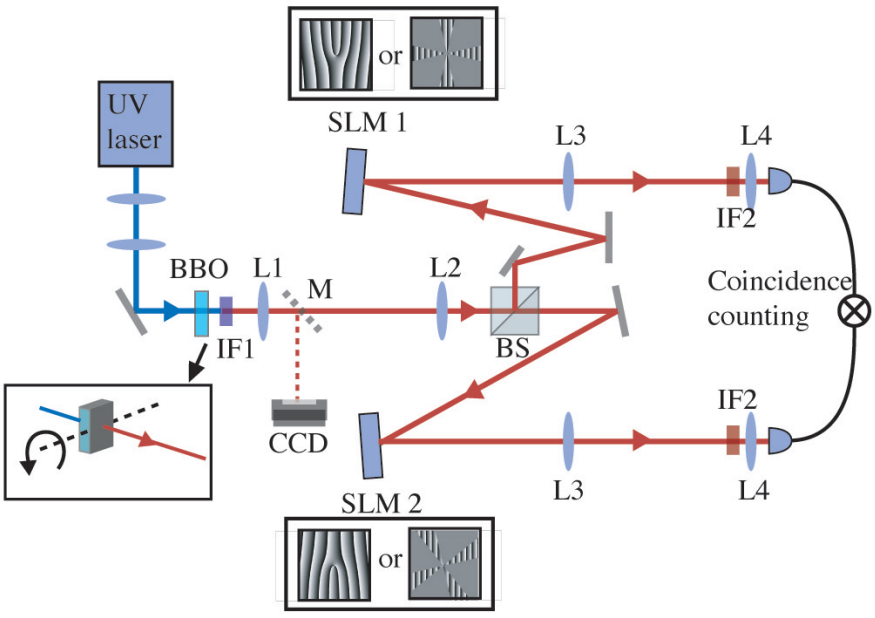

Figure 2.8: We measure in the OAM or angular position basis by programming either a forked diffraction hologram or an angular four-slit pattern on the SLMs (top and bottom insets). The SPDC phase-matching is changed by tilting the BBO crystal about the axis shown (left inset). The CCD camera accessible via the flip-up mirror M allows us to derive a phase-matching parameter according to (2.10). [3]

(IF1) after passing through the crystal. The crystal is mounted on a rotation stage which allows us to change the orientation of the crystal, consequently changing the phase matching from collinear to near-collinear. The signal and idler fields are incident on the same beam splitter and imaged by lenses L1 (f=200 mm) and L2 (f=400 mm) to separate spatial light modulators (SLMs). A flip-up mirror (M) is used to direct the light to a CCD camera positioned at the focal plane of L1 to allow us to capture the far-field intensity of the down-converted fields (fig. 2.3), we fit these intensity patterns with (2.10). The SLMs are imaged by lenses L3 (f=600 mm) and L4 (f=3.2 mm) onto the facets of single-mode fibres coupled to avalanche photodiodes (APD) for single photon detection. Bandpass filters (IF2) of width 2 nm and centred at 710 nm placed in front of the fibres ensure that we measure signal and idler photons near degeneracy. The outputs of the APDs are connected to a coincidence circuit (with a timing window of 10 ns) and the coincidence rate is recorded as a function of the measurement states specified in the SLM.

We measure both OAM and angle correlations for two different phase-matching conditions. To measure OAM we use the mode-projectors we have discussed in section 1.2.2. We encode forked diffraction gratings of topological charge ℓ_s on one SLM and ℓ_i on the other. These holograms transform any incoming field. However, only the the modes satisfying the selection rule (2.6) are transformed to the fundamental mode, which is the only mode that can be coupled to the fibres [65]. Since we are working in the collinear to near-collinear regime, OAM is conserved in our SPDC and we expect the OAM of the signal and idler photon to be anti-correlated. Since our pump carries no OAM, $m = 0$ in (2.6) and the coincidence count is high only when

$\ell_s = -\ell_i$ [126]. Ideally, to measure correlations in angular position, we encode angular slits of width $\delta\phi$ centred at angle ϕ in both SLMs and rotate one with respect to the other, expecting high coincidence counts when the two slits are aligned [5]. Because angle and OAM are Fourier-related [117], a wide spiral bandwidth means a correspondingly narrow angular correlation which should be measured with a narrow angular slit. This presents a limitation in practice because a narrow angular slit means less counts which are difficult to discern against the background. We solve this problem by using not one, but four narrow slits (7° wide, almost twice as narrow as what was used previously [5]) thereby enabling us to still measure tight angular correlations without sacrificing counts. With one four-slit pattern oriented at ϕ_s and another oriented at ϕ_i, we measure the coincidences as a function of $\Delta\phi = \phi_s - \phi_i$. As a result of having four slits, our angular position coincidence curves has more than one maximum (figs. 2.9 c , f insets) from which the width of the angular correlation can be derived.

OAM and angular position measurements for two different phase-matching conditions are shown in fig. 2.9. We have judiciously subtracted the accidental counts, $A = S \times I \times \Delta t$, where S and I are the single channel counts of the signal and idler arms respectively and $\Delta t = 10$ ns is our coincidence timing window. We define the measurement spiral bandwidth, $\Delta\ell$, as the full width at half-maximum of the measured spiral spectrum. We use a Lorentzian function to fit our measured spiral spectrum, with C and $\Delta\ell$ as fitting parameters,

$$P(\ell) = \frac{C\left(\frac{1}{2}\Delta\ell\right)}{\ell^2 + \left(\frac{1}{2}\Delta\ell\right)^2}. \tag{2.21}$$

For collinear phase-matching (fig. 2.9.a), $\alpha = 0$ in (2.10), we find $\Delta\ell \approx$

10 (fig. 2.9.b) and the corresponding half-width of the central peak in the angular position coincidence curve is 12° (fig. 2.9.c). With the addition of an on-axis phase mismatch, $\alpha = -2.2$ in (2.10), the opening angle of the spot is slightly increased (to $\approx 1.1°$, from propagation axis to the first minimum, compared to 0.9° for $\alpha = 0$). There is a central dip in the intensity distribution (fig. 2.13.d), we find $\Delta\ell \approx 20$ (fig. 2.13.e). The half-width of the corresponding angular position correlation is narrower, as expected from the Fourier relationship [117, 127], and is 8°. The solid black lines in fig. 2.9.b and e are in accordance to (2.21). Using these fits, we were able to calculate the expected angular correlation from the Fourier relation, with the added consideration that our angular masks have a finite slit width (solid line in fig. 2.9.c and f, derivation is presented in the appendix). Angular position measurements are very sensitive to alignment, and we attribute the imperfect fits in fig. 2.9.c and f to this.

The entanglement between the signal and idler photons can be characterised by the information that they"mutually share." The shared information indicates how much quantum correlation is present [123]. We focus on our OAM measurements and derive the mutual information, H. This can be calculated from the probabilities,

$$H = -\sum_{\ell_s} p(\ell_s)\log_2[p(\ell_s)] - \sum_{\ell_i} p(\ell_i)\log_2[p(\ell_i)] + \sum_{\ell_s,\ell_i} p(\ell_s,\ell_i)\log_2[p(\ell_s,\ell_i)], \tag{2.22}$$

where $p(\ell_s,\ell_i)$ is the joint probability of measuring ℓ_s and ℓ_i, $p(\ell_s) = \sum_{\ell_i} p(\ell_s,\ell_i)$ is the probability of measuring ℓ_s and $p(\ell_i) = \sum_{\ell_s} p(\ell_s,\ell_i)$ is the probability of measuring ℓ_i. For $\alpha = 0$ the mutual information is 3.17±0.60 bits/photon

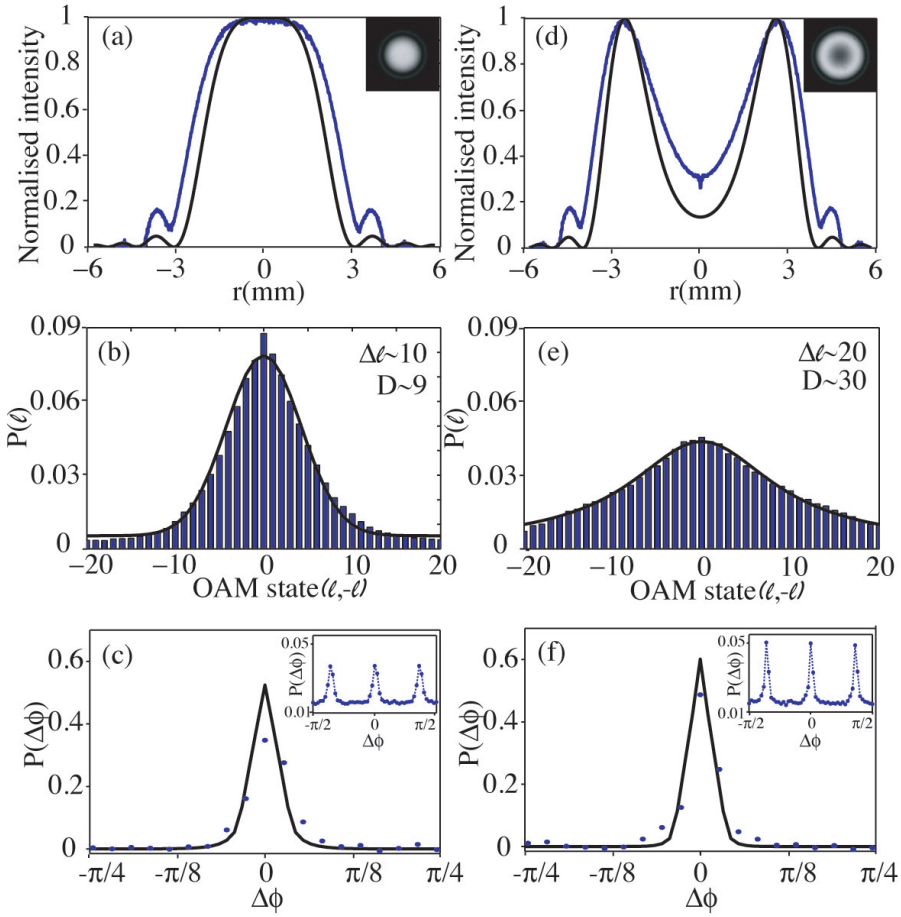

Figure 2.9: (left column) For collinear phase-matching, the far-field intensity profile (blue line) follows (2.10) (solid black line) with $\alpha = 0$ (a). The measured spiral spectrum has a half-width $\Delta\ell \approx 10$, with $D \approx 9$ (b). The central maximum (renormalised and background-subtracted) of our angular position correlation measurement when the signal and idler slits have a relative orientation of $\Delta\phi$, has a half-width of $\approx 12°$ (c). The inset shows the other maxima from the four-slit pattern. (right column) For noncollinear phase-matching (d), $\alpha = -2.2$ in (2.10), the measurement spiral bandwidth is wider, with $\Delta\ell \approx 20$, $D \approx 30$ (e) and the angular position correlation is narrower, with a half-width of $\approx 8°$ (f). Blue dots and bars are experiment results, solid black lines are fits that demonstrate consistency with a Fourier relation between OAM and angle. [3]

corresponding to a dimensionality $D = 2^H \sim 9$. Adjusting the phase matching to $\alpha = -2.2$ results in a mutual information of 4.94 ± 1.03 bits/photon corresponding to $D \sim 30$, twice the measurement range of our previous results in [5]. We remark that apart from being detection-limited, we have also defined our dimensionality stringently by calculating it from the mutual information. In this way we are sensitive to the level of noise and cross-talk even for measurements where $\ell_s \neq \ell_i$, which becomes more apparent with higher-valued OAM states. As such, we expect our dimensionality to be less than the Schmidt number for our system (recall K in section 2.4.1). We have independently measured K for our system via sector phase-plates and find these greater than our measured D. For $\alpha = 0$ we obtain $K = 35 \pm 2$, and for $\alpha = -2.2$ we obtain $K = 49 \pm 2$ [128]. The values of K can also be estimated from [95], which gives 35 for $\alpha = 0$ and 43 for $\alpha = -2.2$ with our experiment parameters. We also remark that K, being defined in terms of just probabilities, does not give any hint on the shape of the spiral spectrum. A full decomposition in terms of OAM modes has been treated elsewhere, albeit not for the noncollinear case [88, 91]. The OAM spectrum, although not strictly Lorentzian, is Lorentzian-like in shape, and this has motivated us to use the Lorentzian fit in (2.21)[88, 55]. Theoretical fits for our results, and hence estimates for $\Delta\ell$ can only be obtained from a full model of our experiment, such as one based on the Klyshko back-propagation picture [129].

2.4.3 Optical étendue and dimensionality

A simple geometrical argument can explain why the spiral spectrum widens as we tune the phase-matching. This involves the concept of the optical

étendue, $E = A\Omega$, where A is the near-field beam area and Ω is the solid angle subtended by the beam in the far-field [121, 130]. In the treatment of noise in laser amplifiers, the étendue normalised with respect to the wavelength λ, E/λ^2, is the number of transverse modes that can be supported, hence E acts as a measure of the quantum states in a beam [130, 131]. E is more often invoked in the discussion of light collection, but is equally applicable in the case of SPDC where light is instead being emitted. Regardless of the phase-matching, A is the same in our experiment: the SLMs are in the near-field of a particular plane in the crystal (fig. 2.8) and minute changes to crystal orientation (typically 1/20 of a degree) do not change the image on the SLMs. However, changes to the crystal orientation do modify the far-field opening angle. The far-field opening angle Ω, increases for $\alpha = -2.2$, hence the number of transverse (both azimuthal and radial) modes emitted increases. In setting up an SPDC experiment, this has important practical implications: one should ensure that the detection étendue is greater than the generation étendue to maximise the overlap between the pump and detection modes. Using the Klyshko picture as a guide (fig. 2.4.b), the overlap is maximised by keeping all corresponding far-field solid angles and near-field beam diameters in the signal and idler arms the same. The reason we use two lenses to image the crystal onto the SLMs, instead of one, is to match the far-field angles in both arms, thus providing an effective detection system.

2.4.4 Entanglement measures

Measuring the entanglement of D dimensions is not as straightforward as measuring the entanglement of 2-dimensional systems. We can violate a Bell

inequality for higher dimensions as implemented in [55], but this is difficult for D $\sim$ 30 because the intensity modulation necessary to do this reduces the count rates considerably. Instead, we employ the entanglement measure,

$$E = \sum_{\ell_s, \ell_i} |p(\ell_s, \ell_i) - p(\ell_s)p(\ell_i)| \tag{2.23}$$

proposed in [132] which applies for pure states. E is zero for separable (non-entangled) states. For our results, we calculate values of 0.81 ± 0.01 and 0.81 ± 0.02 for $\alpha = 0$ and $\alpha = -2.2$ respectively, indicating that our two-photon OAM states are non-factorable and therefore entangled. It is reasonable to expect that E increases for the $\alpha = -2.2$, more entangled modes should lead to a higher entanglement measure. However, we do not get a higher E in this case because of the presence of crosstalk which becomes more apparent for higher OAM modes.

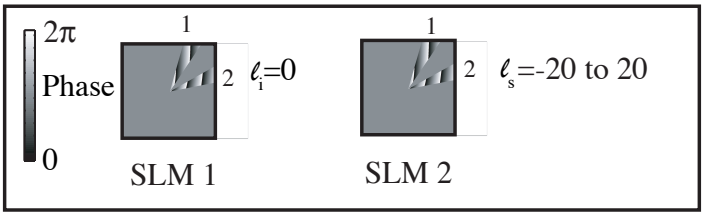

Figure 2.10: We encode two-slit patterns (width 18°, separated by 45°) in SLM1 and SLM2 with the corresponding OAM values (ℓ_s and ℓ_i) shown.

Furthermore, we exploit the Fourier relationship, or complementarity between OAM and angle [117, 133] to characterise the entanglement in the angular position basis. When a photon passes through an angular aperture, angular diffraction results in interference in the OAM distribution of the sig-

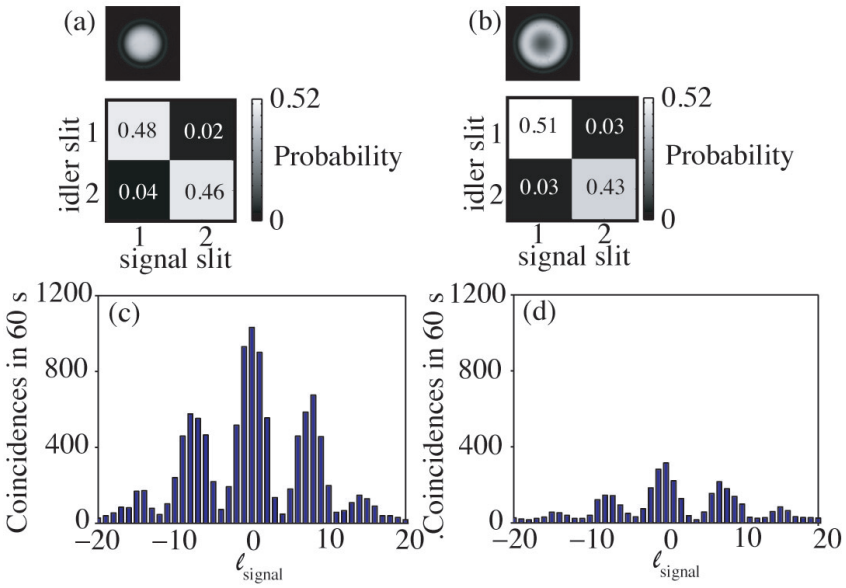

Figure 2.11: We encode two-slit patterns (width 18°, separated by 45°) in SLM1 and SLM2 with the corresponding OAM values shown (a). With only one slit in each SLM (1 or 2), we verified the strong angular position correlation. For $\alpha = 0$, we only get high coincidences when both SLMs have slits with the same angular position (b). The measured concurrence is 0.96 (c). We show similar angular position correlation for $\alpha = -2.2$, (d) and measure a concurrence of 0.90 (e). [3]

nal (or idler) field. Effectively, restricting the angle of one photon changes the OAM spectrum of the other photon. The modulation observed depends on the spiral spectrum [134]. We use the same setup in fig. 2.8, where we now encode angular two-slit patterns on the SLMs (slits 1 and 2. fig. 2.10). We measure the resulting OAM interference when SLM 1 (idler) is set to measure $\ell_i = 0$ and the value of ℓ_s on SLM 2 is scanned from $-\ell_{max}$ to ℓ_{max} ($\ell_{max} = 20$ in our case). We do this so that we can measure the concurrence, which is another entanglement measure ranging from 0 to 1, with 1 corresponding to the maximally entangled case. It has been shown that the visibility of the resulting interference pattern when we do the measurements in fig. 2.10 is the same as the concurrence of the two-qubit density matrix written in the angular position basis [134, 135].

We first verify strong angular position correlation in fig. 2.11.a and b, where we have measured the coincidences when only one slit has been encoded on each SLM for both phase-matching conditions. As expected, because the SLMs are in an image plane of the crystal, we only get appreciable coincidences when the same slit positions are encoded for both SLMs. Ideally the diagonals should be 0.5, but due to imperfect alignment we get small probabilities off the diagonal. Having established strong angular position correlation, we encode the holograms in fig. 2.10. The interference of these two-slit patterns leads to a modulation in the coincidences which can be measured in the OAM basis. Fig. 2.11.c and d show the coincidences for $\alpha = 0$ (a inset) and $\alpha = -2.2$ (b inset). The measured concurrence is 0.96 ± 0.07 for $\alpha = 0$ and 0.90 ± 0.12 for $\alpha = -2.2$, demonstrating that we indeed have entangled angular qubit states for both phase-matching conditions. We remark

that the decrease in the concurrence value is not expected considering that the latter case corresponds to a greater number of OAM modes. This may be due to imperfect alignment, as measurements in the angular position basis are more sensitive to this. We also emphasise that the measurements made in fig. 2.11.a and 2.11.b (strong angular position correlation) and fig. 2.11.c and 2.11.d (interference in the OAM basis) can be produced simultaneously only by OAM-angular position entangled sources. The good entanglement measures in both OAM and angular position bases for both phase-matching conditions, $\alpha = 0$ and $\alpha = -2.2$ where $D \sim 9$ and $D \sim 30$ respectively, indicate genuine two-photon D-dimensional entanglement, where D is tuneable.

2.5 SPDC with a phase-flipped Gaussian mode as pump

Exploring the higher dimensions afforded by OAM generally means the design of holograms that measure superpositions of different OAM states [11, 109, 136, 137]. But since SPDC is very much dependent on the pump beam [86, 88], one can also explore the high-dimensional OAM state space by engineering the pump. Shaping the pump with more complex modes has been proposed to prepare high-dimensional entangled OAM states, although this has not been implemented experimentally [125, 138]. In this section, we describe a step in that direction. We employ a non-fundamental Gaussian pump beam for SPDC and analyse how the OAM and angle correlations change as a result.

2.5.1 Pump shape and SPDC

In SPDC, a pump beam is usually approximated as a plane wave incident on a nonlinear crystal, which results in the emission of two correlated photons in definite directions. The bulk of the studies on entangled photons produced by SPDC has concentrated on manipulating these two outgoing photons by letting them pass through polarisers, slits, holograms, and other optical components, to observe various desired quantum effects [6, 52, 65, 8, 7, 139].

Manipulating the pump field is also an interesting enterprise, as the fields generated in SPDC are strongly related to the pump field; this has been investigated theoretically and experimentally [65, 86, 88]. Phase matching allows the amplitude and phase structure of the pump to be transferred to the two-photon field, and fourth-order images related to the aperture in front of the pump can be formed by the down-converted beams [86]. Focusing the pump before the crystal leads to two-photon geometric optics effects wherein the crystal acts like a spherical mirror in the formation of the fourth-order images [106].

More relevant to us, the shape of the pump is of consequence to correlations in the OAM and angular position of the signal and idler fields. We have already noted that the transfer of the plane-wave spectrum of the pump to the two-photon field leads to conservation of OAM in SPDC [80, 126, 140]. Experiments where the crystal is pumped with a beam of nonzero OAM follow conservation of OAM [65, 80].

It is possible to generate arbitrary two-photon OAM states. It has been predicted that a maximally entangled state consisting of only four modes (in contrast to the infinite OAM spectrum of (2.8)) can be obtained by pumping

the crystal with a suitable superposition of OAM modes which result in a number of phase singularities [125]. However, this entails the modulation of both the phase and intensity of the pump, and has yet to be achieved experimentally. The first step towards the implementation of such schemes is to have an element which will efficiently convert the fundamental mode of a pump laser to the desired mode for SPDC.

Several experiments [65, 80] have performed this mode conversion with cylindrical lenses, holograms or with a cover slip [141, 142]. Simple pump shapes could be implemented with simple mode converters. For instance, HG modes can be created by placing one to two wires inside a laser cavity [143]. We do not have access to the laser cavity of our pump laser, so instead we use a cover slip that introduces a π-phase shift to half of the area of the usual Gaussian output of a laser beam. This introduces a phase-flip to one half of the beam, hence the name "flipped mode" [144]. Following [144], the flipped mode $u_{f,0}$ is the fundamental Gaussian mode with a phase flip at $x = 0$. This can be expressed as an infinite sum of odd Hermite-Gauss (HG) modes $u_{2n+1}(x)$,

$$u_{f,0} = \sum_{n=0}^{\infty} c_{2n+1} u_{2n+1}(x) \tag{2.24}$$

where

$$c_{2n+1} = \frac{(-1)^n (2n)!}{n! \sqrt{\pi 2^{2n-1} (2n+1)!}}, \tag{2.25}$$

giving $\sqrt{2/\pi} \approx 0.80$ as the contribution of the first-order HG_{10} mode. Since the LG modes form a convenient basis for OAM-carrying beams, it is in-

structive to express $u_{f,0}$ in terms of Laguerre polynomials L_k^j [145, 146],

$$\begin{aligned} u_{f,0} &= \sum_{n=0}^{\infty}\sum_{p=0}^{n} a_{np}\exp\left(-\left(\frac{r}{\omega}\right)^2\right)\left(\frac{\sqrt{2}r}{\omega}\right)^{|2(n-p)+1|} \\ &\times L_p^{2(n-p)+1}\left(2\left(\frac{r}{\omega}\right)\right)\left(\exp\left(i(2(n-p)+1)\right)+\exp\left(-i(2(n-p)+1)\right)\right) \end{aligned} \tag{2.26}$$

where $a_{n,p}$ is

$$a_{n,p} = (-1)^{n+p}\sqrt{\frac{8}{\pi}}\frac{(2n)!}{(2n+1)!}\frac{(n+1/2)!}{2p!}\frac{2p!}{\pi(p+(2(n-p)+1))!}$$

Hence, only the odd LG modes contribute reflecting the parity of the mode. A table of the decomposition in terms of the LG_p^ℓ modes for p=0 is given in Table 2.1.

Table 2.1: Decomposition in LG basis

ℓ	$\langle LG_0^\ell \vert u_{f,0}\rangle$
±5	$\frac{1}{8}\sqrt{\frac{3}{10\pi}} = 0.0386$
±3	$\frac{-1}{2}\sqrt{\frac{1}{6\pi}} = -0.1151$
±1	$\sqrt{\frac{1}{\pi}} = 0.5642$
0	0

The flipped mode(top inset in fig. 2.12) has been used in SPDC to produce singlet states [141], to demonstrate multimode Hong-Ou-Mandel interference, and to generalise genuine non-Gaussian entanglement [142, 147]. Since the combination of OAM states $|1\rangle$ and $|-1\rangle$ make the most significant contributions to the flipped mode, in contrast to the usual Gaussian pump which is in the OAM state $|0\rangle$ [148], we expect different OAM and angle cor-

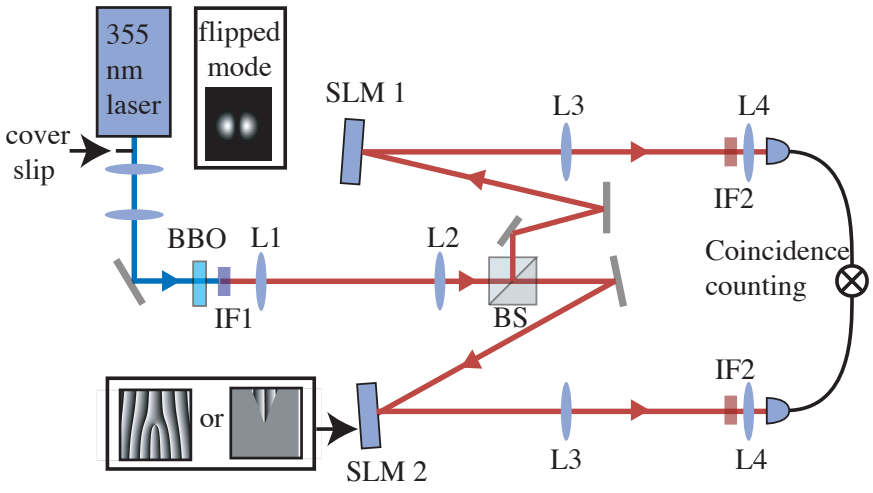

Figure 2.12: The pump is shaped by a cover slip thereby introducing a π-phase shift to half of the output Gaussian beam (top inset). The OAM or angular position of signal and idler photons are measured by programming the SLM with either a forked diffraction grating or an angular slit respectively (bottom inset). [4]

relations from that in [5]. Specifically, we expect coincidences when $\ell_s + \ell_i$ is odd with the strongest correlations occurring when $\ell_s + \ell_i = \pm 1$. For the angular correlations, we can again invoke the Fourier relationship between OAM and angle, given that we have knowledge of the OAM components of the entangled photons [117] .

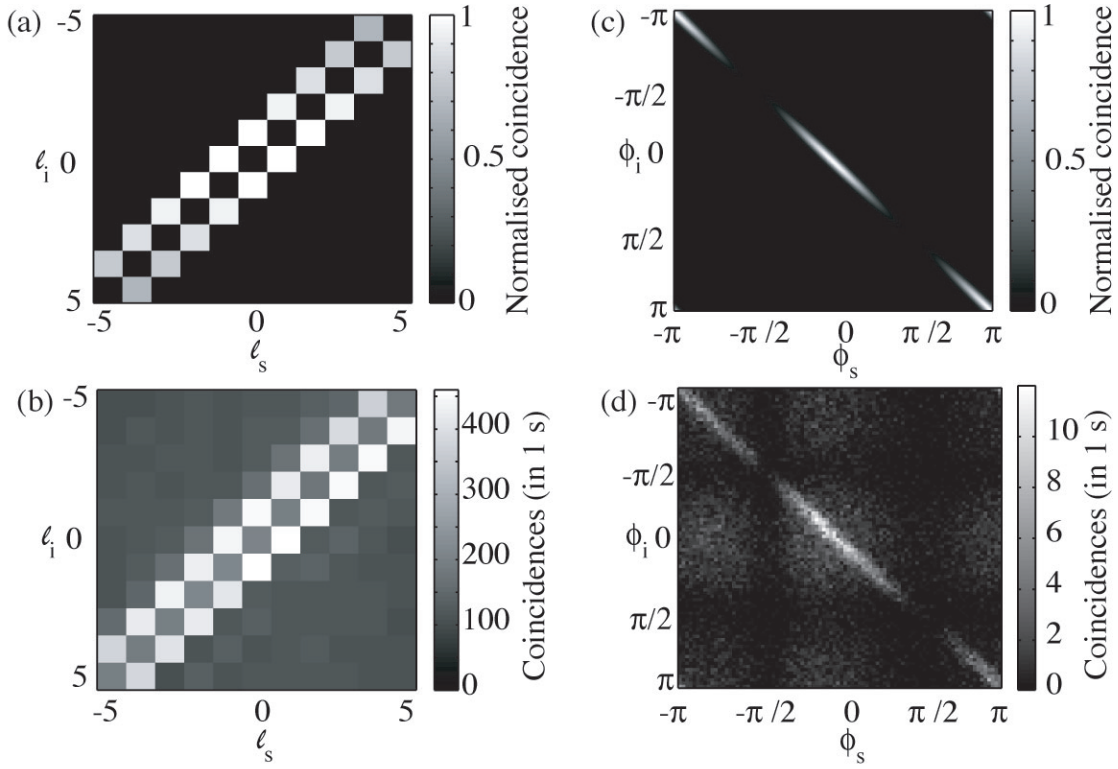

Figure 2.13: With the pump having largest contributions from $|1\rangle$ and $|-1\rangle$ we expect the coincidences to be high when $\ell_s+\ell_i = \pm 1$ (a). This is supported by the OAM correlations we obtain from our experiment (b). The angular position correlations also reflect the shape of the pump, and in theory can be obtained via the Fourier relationship between OAM and angular position. From the OAM correlations in (a), we expect the modulated coincidence in (c). Coincidence is high along the diagonal when $\phi_s = \phi_i$, but with minima corresponding to the position of the phase discontinuity in the pump. Apart from some background counts, our experiment results support this (d). [4]

2.5.2 Experiment and Results

Apart from the pump before the BBO crystal and the change of the focal length of L4 from 3.2 mm to 2.0 mm, the details of our setup for this experiment is the same as that in the previous experiment. We use collinear phase-matching throughout the experiment, the camera to check phase-matching is not shown in fig. 2.12 for simplicity. To create a phase-flipped Gaussian mode, a cover slip is placed on a translation stage positioned such that the cover slip obstructs half of the UV pump beam. The cover slip is also attached to a tip-tilt mount to control the phase introduced to the pump. We measure OAM as before, where each SLM displays a hologram with a fork dislocation of order ℓ_s and ℓ_i, corresponding to the OAM states $|\ell_s\rangle$ and $|\ell_i\rangle$. The pump beam consist of superpositions of odd-valued OAM states, with $|1\rangle$ and $|-1\rangle$ making the largest contribution [148]. Hence following the selection rule (2.6) , we expect high coincidences when the sum of ℓ_s and ℓ_i is ± 1, as shown in fig. 2.13.a. We expect two diagonals symmetric about the main diagonal, in contrast to SPDC with a fundamental Gaussian pump wherein there is only one main diagonal [5]. Fig 2.13.b shows the coincidences, as a function of ℓ_s and ℓ_i, that we obtained from the experiment. Apart from a uniform background (we did not do any background subtraction in our results), and residual on-axis coincidences (due to the imperfect conversion of the pump laser output to a flipped mode) there is good qualitative agreement between fig. 2.13.a and 2.13.b, showing the transfer of the pump OAM spectrum to the entangled photons.

To measure angular position, we employ angular slits of width $\Delta\theta$ which are oriented at positions ϕ_s and ϕ_i in the signal and idler SLMs respectively

(fig. 2.13.b). We can obtain the expected angular position correlations shown in fig. 2.13.b from the Fourier relationship, by performing a Fourier transform on figure 2.13.a. Because the SLMs are in the image plane of the crystal, we expect the coincidences to be high for $\phi_s = \phi_i$. In addition, due to the shape of the pump, we see a modulation wherein there are coincidence minima corresponding to the case when the slit is aligned with the phase discontinuity in the pump. Figure 2.13.d shows the coincidence counts as a function of the angular positions ϕ_s and ϕ_i. There is good qualitative agreement between figure 2.13.c and 2.13.d, apart from an almost uniform background.

We focused on a simple pump shape, but more complicated modes are possible with combinations of cover slips (for HG pump modes), specially fabricated components or programmable spatial light modulators.

2.6 Conclusion

We have examined spontaneous-parametric down-conversion, focusing on the two important factors that determine the two-photon state: phase-matching and the spatial properties of the pump.

In the first experiment, we have exploited phase-matching to increase the dimensionality of our OAM-entangled photons. We have presented a system where we can generate and detect high-dimensional two-photon entanglement. We have characterised the entanglement in terms of the mutual information shared by the entangled photon pairs. Minute changes to the angular orientation of a bulk BBO crystal ($\approx$1/20 of a degree) widens the

OAM measurement spiral spectrum and narrows the angular position correlation, as a consequence of phase-matching in SPDC. We have designed our detection system guided by the concept of the optical étendue, and we have achieved as much as 4.94 bits/photon implying 30-dimensional OAM entanglement. We can obtain a relatively flat spectrum for a few OAM modes which could allow future protocols to forego entanglement concentration.

We note that although the OAM value is in a high-dimensional space, our measurements are still dichotomous. With a forked hologram, we can only ask whether a photon is of a particular OAM or not. This is in contrast to a polarisation beam splitter which sorts the two possible polarisation states. However, a mode-sorter which separates all of the D orthogonal OAM states has been recently developed [149]. Coupled with the generation and detection geometry that we have characterised in this work, this points to the possibility of new experiments such as detection loophole-free Bell test experiments [150], superdense coding [151, 152] beating the linear optics threshold and multi-valued quantum walks [153] where a higher-dimensional space is desirable.

In the second experiment, we have shown the effect of the pump shape on OAM and angle correlations exhibited by photon pairs from SPDC. We focused on a particularly simple OAM superposition state, but more complicated pump shapes such as the vortex pancakes suggested in [125] can be used for tailored entangled states. The correlations that arise result from the transfer of the OAM spectrum of the pump to the down-converted photon pairs, as manifested in the OAM correlation matrix. We have shown a modulation in the angular position correlation which is consistent with

the Fourier relationship between OAM and angle. The spatial structure of down-converted light is a rich playground to observe correlations in a variety of spatial modes, not just OAM. If efficiency is not a priority, spatial light modulators can be introduced not just in the measurement, but also in the generation of entangled photons. With the flexibility afforded by spatial light modulators, different pump modes can be used to prepare the entangled states. In addition to current developments in sorting OAM states[149] and OAM gates[154], this will certainly be a step forward to fully exploring a D-dimensional space for quantum information.

Chapter 3

Quantum Tests

Quantum mechanics is, undeniably, a successful theory. However, many issues at its foundation still baffle us, one of which is the transition from probabilistic quantum mechanics to deterministic classical mechanics. If there is an underlying deterministic theory (e.g. one involving hidden variables) of which quantum mechanics is an approximation, our common-sense notion of the world can be restored. Most tests of this kind measure the polarisation states of light, but here we present a variety of tests measuring spatial light modes. We first demonstrate the Eisntein-Podolsky-Rosen paradox using orbital angular momentum and angular position variables. We then test local hidden variable (LHV) theories as an alternative to quantum mechanics in explaining our observed correlations. We discount LHVs by (1) showing a violation of Bell-type inequalities and (2) showing a logically inconsistent chain of probabilities akin to the Hardy paradox. We also

test nonlocal hidden variable (NHV) theories and show that even these are in conflict with quantum mechanics, via violations of Leggett-type inequalities. All these tests were made possible by the versatility afforded by spatial light modulators in measuring spatial modes.

J Leach, B Jack, J Romero, A K Jha, A M Yao, S Franke-Arnold, D G Ireland, R W Boyd, S M Barnett and M J Padgett, Science 329, 5992, 662 (2010)

J Leach, B Jack, J Romero, M Ritsch-Marte, R W Boyd, A K Jha, S M Barnett, S Franke-Arnold, and M J Padgett, Opt Express 17, 8287 (2009)

B Jack, A M Yao, J Leach, J Romero, S Franke-Arnold, D G Ireland, S M Barnett, and M J Padgett, Phys Rev A 4, 43844 (2010)

L Chen and J Romero,Opt Express 19, 21687-21692 (2012)

J Romero, J Leach, B Jack, S M Barnett, M J Padgett, and S Franke-Arnold, New J Phys 12, 123007 (2010)

3.1 Quantum system and quantum tests

The quantum system that we consider in the experiments described in this chapter consists of the spatial mode of a photon. More specifically, we consider states of a specific orbital angular momentum (OAM), superpositions of OAM and the conjugate variable to OAM, angular position. Needless to say, most physicists believe that quantum mechanics is true. Testing any alternative theory to quantum mechanics is expected to lead to the same conclusion–the alternative theory is wrong and quantum mechanics (still) is the best description of measurement outcomes. This is indeed true, and moreover, all of the tests that will be discussed here have already been shown for polarisation (or some other degree of freedom). However, when we examine the history of optical implementations of quantum information, OAM and angular position (angle) are relative newcomers. For example, polarisation entanglement has been demonstrated in the 1970s-80s [6, 52, 73] and OAM entanglement only in 2001 [65]. Not surprisingly, OAM has yet to achieve the ubiquitousness of other degrees of freedom (e.g. polarisation, time-bin, energy, etc.). But if OAM does become more pervasive in the future, it will be assuring to know that quantum tests done (in two-dimensional subspaces embedded) in the high-dimensional state space of photon OAM lead to the same conclusion as those done with other photonic properties. With that in mind, we can proceed with the "superfluousness".

3.1.1 Classical and Quantum Correlations

We use the word "correlation" in this chapter often and in the broadest sense. Inevitably, our notion of correlation involves the results of measurements that we make on separated subsystems (e.g. the signal and idler photon of our down-converted photon pair). Given the outcome of the measurement on one photon, we know the outcome of the measurement on the other photon. Although "correlated" and "entangled" are sometimes used interchangeably, correlations are not exclusively quantum. Take for instance a box containing two balls, one black and one white. There are two experimenters, Alice and Bob. Alice opens the box, takes one ball (but does not show it to Bob), closes the box and hands the box to Bob. Bob then takes the box, opens it, and sees that the ball remaining is white. Right away, Bob knows that the ball with Alice is black. Bob having a white ball is correlated with Alice having a black ball, but there is nothing quantum in that.

So when are correlations quantum? We can answer this question more mathematically in terms of probability and entropic measures (as we have done in the previous chapter). An alternative, which may be more "physical" is to construct a reasonable theory X (maybe within/outwith a classical framework) and test if this theory accounts for the observed correlations. If X accounts for the correlations, then the correlation is not necessarily quantum. Otherwise, if quantum mechanics gives the best description of the observed correlations, then we say that the correlation is quantum, at least until we find a better description.

Note: The general experiment schematic has been presented in the previous chapter and details of the common parts of the setup (the SLMs, pump laser, detectors, coincidence circuit) will no longer be mentioned here. The experimental setup will be sketched for each of the following sections, with the details being given in the figure captions rather than the main body. The EPR and Bell experiments are not solely my work, and were done nearer the beginning of my PhD together with J. Leach and B. Jack. I have included them here to make a more complete story. The ideas for the Hardy experiment were developed with L. Chen and implemented by me.

3.2 Einstein-Podolsky-Rosen paradox with OAM and angle

In 1935, Einstein, Podolsky and Rosen (EPR) showed an apparent paradox between *local realistic* theories and quantum mechanics. Locality implies that measurements made on a subsystem which is spatially separated from another subsystem can not influence the results of the measurement on the other subsystem. EPR also define "elements of physical reality"– if the value of a physical quantity can be predicted with certainty without disturbing the system, then this physical quantity has a corresponding element of physical reality. They then formulated a thought experiment (fig. 3.1.a) on two particles (labelled 1 and 2) that have "interacted in the past". The state of the composite system in the position basis can be written as $\Psi(x_1, x_2) = \delta(x_1 - x_2 - L)$, where x_1 and x_2 refer to the the position of particle 1 and 2 respectively, and L is some large distance such that there is no interaction

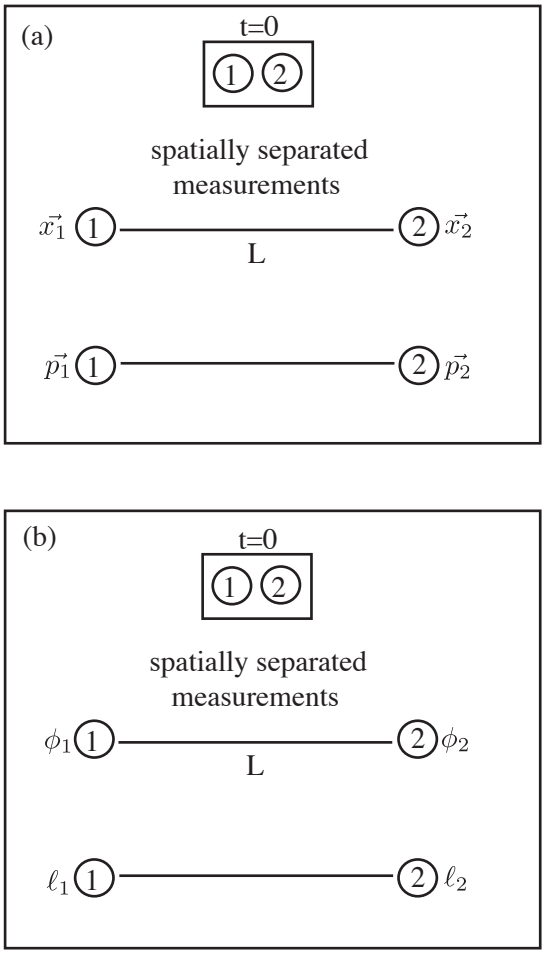

Figure 3.1: The original EPR paradox is expressed in terms of position and momentum (a). The EPR paradox we present here is expressed in terms of angular position and OAM (b).

between the two particles. We can also write the state of the composite system in the momentum basis as $\Psi(p_1, p_2) = \delta(p_1 + p_2)$. Note that in these descriptions we do not know individually the position or the momentum of either particle, but we know their relative position and their total momentum. If we set to measure x_1, we will be able to predict with certainty x_2 (because we know the relative position), without disturbing particle 2. Hence, x_2 corresponds to an element of reality. On the other hand, if we set to measure p_1, we will be able to predict with certainty p_2 (because we know the total momentum), again without disturbing particle 2. Hence, p_2 also corresponds to an element of reality. However, quantum mechanics does not allow the simultaneous knowledge of position (x_2) and momentum (p_2) with absolute certainty. As Einstein notes [155], this paradox forces us to give up either of two statements: (1) quantum mechanics is complete or (2) the real states of spatially separated objects are independent of each other. To Einstein, the second statement (locality) was indisputable, hence he leaves open the question of whether quantum mechanics can be complete.

The first EPR paradox demonstration with continuous variables (quadratures) was done in 1992 by Ou et al. [156]. More recently, the EPR paradox has been demonstrated for position and linear momentum by Howell et al. [33], where they have measured position correlations and momentum correlations on the separated photons. Given a precise measurement of the position of the signal photon, they can predict the position of the idler photon with an uncertainty Δx_i. Given a precise measurement of the momentum of the signal photon, they can predict the momentum of the idler photon with an uncertainty Δp_i. To show the paradox, $(\Delta x_i)^2(\Delta p_i)^2 \leq \hbar^2/4$.

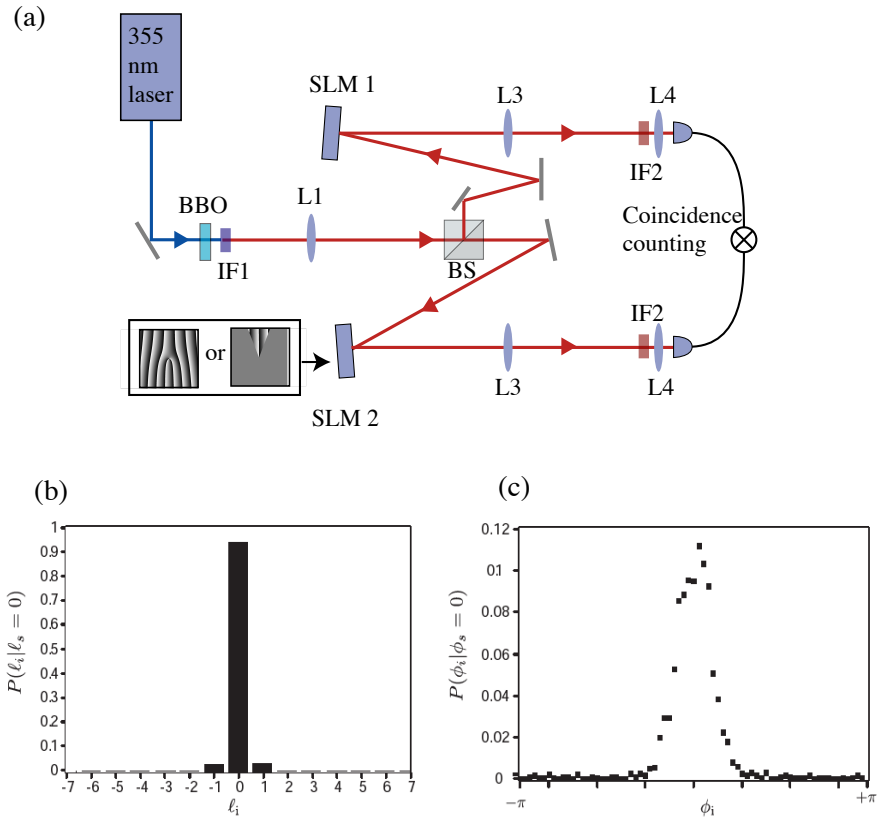

Figure 3.2: We have SPDC from a 3-mm BBO crystal as source of our entangled photons. The crystal is imaged by L1 (f=300 mm) onto separate SLMs, where we encode either a forked diffraction grating or an angular transmission mask (with transmission tailing off towards the edges). The SLMs are again imaged by L3(f=600 mm) and L4(f=1.6 mm) onto the facet of single-mode fibres through 2 nm wide interference filters centred at 710 nm (a). The plots for conditional probability (b-c) show that we can infer the OAM value of the idler photon(ℓ_i), given the OAM value of the signal photon (ℓ_s) and that we can infer the angular position of the idler photon (ϕ_i) given the angular position of the signal photon (ϕ_s). [5]

We have implemented an experiment conceptually similar to the original EPR paradox, apart from the fact that we are measuring angular position and OAM (fig. 3.1.b). As with the experiments of Zeilinger and co-workers, measuring OAM can be achieved with a forked diffraction grating. Measuring the angular position can be achieved with an angular slit (fig. 3.2.a). Both of these optical elements can be implemented using SLMs. Measuring the OAM of the signal photon allows us to predict the OAM of the other (which will have the opposite value) with an uncertainty $\Delta\ell_i$. Similarly, measuring the angular position of the signal photon gives the angular position of the other (which will have the same value) with an uncertainty $\Delta\phi_i$ (fig. 3.2.c-d). The ability to show strong correlation in either of the two Fourier-related basis sets is completely analogous to the original formulation of the paradox and is a demonstration of the EPR paradox for angles and OAM [5]. We used the EPR-Reid criterion which shows the paradox for $(\Delta\ell_i)^2(\Delta\phi_i)^2 \leq 1/4$ [157]. The variance product that we obtain, $(\Delta\ell_i)^2(\Delta\phi_i)^2 = 0.024 \pm 0.004$, is an order of magnitude lower than the EPR criterion. Although OAM is discrete (unlike linear momentum which is continuous) and angle is periodic, the EPR paradox nevertheless applies to these variables. Again, this implies that we either give up the completeness of quantum mechanics or locality.

3.3 Local hidden variable theory

It transpires that EPR states can indeed be demonstrated in the laboratory. Locality is such an obvious and reasonable concept that it is difficult to let it go. This has been a motivation for attempts to "complete" quantum

mechanics, and alternative theories abound. Local hidden variable theory is one such attempt, and this can be tested with the Bell inequality.

3.3.1 Local hidden variables and Bell inequality

Bohm reformulated the EPR paradox in terms of spin systems. We will consider an optical analogue to Bohm's formulation in terms of polarisation [6, 52]. Let us consider a specific entangled state,

$$|\Psi_{s,i}\rangle = \frac{1}{\sqrt{2}}|H\rangle|_A H\rangle_B + |V\rangle_A|V\rangle_B \tag{3.1}$$

where H and V denote horizontal and vertical polarisations respectively, and the subscripts $\{A, B\}$ denote the states of the signal and idler photons (or Alice's and Bob's photon as will be introduced shortly). Each photon is sent to its own measuring station, which consists of a polariser of orientation $\mathbf{a}$ ($\mathbf{b}$). Each polariser is followed by detectors giving dichotomic results, $+$ or $-$ corresponding to polarisation parallel or perpendicular to $\mathbf{a}$ ($\mathbf{b}$). The probabilities of getting $+$ or $-$ ($P_{\pm}(\mathbf{x})$) for individual measurements are: $P_{+}(\mathbf{a}) = P_{-}(\mathbf{a}) = 1/2$ and also $P_{+}(\mathbf{b}) = P_{-}(\mathbf{b}) = 1/2$, that is, individual polarisation measurements are random. Quantum mechanics also predicts the joint probabilities depending on the relative orientation of the polarisers $\Delta\theta = \mathbf{a} - \mathbf{b}$,

$$P_{++}(\Delta\theta) = P_{--}(\Delta\theta) = \frac{1}{2}\cos^2(\Delta\theta) \tag{3.2}$$

$$P_{+-}(\Delta\theta) = P_{-+}(\Delta\theta) = \frac{1}{2}\sin^2(\Delta\theta). \tag{3.3}$$

If $\Delta\theta = 0$, then $P_{++} = P_{--} = 1/2$, while $P_{+-} = P_{-+} = 0$. This means that, although individual measurements are random, if the result in the signal photon is $+$, the result in the idler photon is $+$ with *certainty* (similarly for $-$). It is easy to attribute a classical picture to this; the spin angular momentum at the start has a definite sum (0), and this has to be conserved regardless of how far the photons are from each other. The polarisations should then always be parallel, and half of the results will be $++$ and the other half will be $--$. We can then invoke "supplementary parameters" that will determine whether the pair of measurements will generate $++$ or $--$. These supplementary parameters are not contained in the quantum mechanical description of (3.1), hence the name "hidden variables" (HVs). HVs differ from one pair to another. One can imagine HVs as the photons having a "prior agreement" that determines the outcome of future measurements. Theories involving local hidden variables are not unreasonable. Quantum mechanics could really be incomplete in that it could be just an approximation of an underlying deterministic theory. Local HV theories maintain that spatially separated measurements have no influence on each other, and that measurements can be predicted with certainty (hence real) given the knowledge of the HVs. In 1964, Bell came up with a theorem which involves an inequality that puts a limit to the correlations that can be achieved by any local HV theory. This made local HV theories testable, as proven later on by experiments.

We will now outline Bell's theorem [66, 67, 68] as proposed by Clauser, Horne, Shimony and Holt (CSHS) in 1969 [158]. The HVs are denoted by λ, and consequently the results of measurements, $A(B)$, will be a function of λ

and the orientations of the polarisers **a** and **a'** (**b** and **b'**), note that these orientations are different from horizontal and vertical. We have $A(\lambda, \mathbf{a}) = \pm 1$ and $B(\lambda, \mathbf{b}) = \pm 1$. We then consider,

$$\begin{aligned} s &= A(\lambda,\mathbf{a})B(\lambda,\mathbf{b}) - A(\lambda,\mathbf{a})B(\lambda,\mathbf{b}') + A(\lambda,\mathbf{a}')B(\lambda,\mathbf{b}) + A(\lambda,\mathbf{a}')B(\lambda,\mathbf{b}') \\ &= A(\lambda,\mathbf{a})\left[B(\lambda,\mathbf{b}) - B(\lambda,\mathbf{b}')\right] \quad + \quad A(\lambda,\mathbf{a}')\left[B(\lambda,\mathbf{b}) + B(\lambda,\mathbf{b}')\right]. \quad (3.4) \end{aligned}$$

Because A and B can only be ± 1, from (3.4), $s = \pm 2$. Assuming there is a probability distribution of HVs, $\rho(\lambda)$, the average of s will be between -2 and $+2$, that is

$$-2 \leq \int d\lambda \rho(\lambda) s(\lambda, \mathbf{a}, \mathbf{a}', \mathbf{b}, \mathbf{b}') \leq 2. \quad (3.5)$$

We now define a correlation function E,

$$E(\mathbf{a}, \mathbf{b}) = \int d\lambda \rho(\lambda) A(\lambda, \mathbf{a}) B(\lambda, \mathbf{b}) \quad (3.6)$$

such that we can write (3.4) in terms of (3.6), and (3.5) becomes,

$$-2 \leq E(\mathbf{a}, \mathbf{b}) - E(\mathbf{a}, \mathbf{b}') + E(\mathbf{a}', \mathbf{b}) + E(\mathbf{a}', \mathbf{b}') \leq 2, \quad (3.7)$$

In the literature, the Bell parameter is denoted by S and is defined as $S = E(\mathbf{a}, \mathbf{b}) - E(\mathbf{a}, \mathbf{b}') + E(\mathbf{a}', \mathbf{b}) + E(\mathbf{a}', \mathbf{b}')$, hence the usual form of the Bell inequality $|S| \geq 2$. Quantum mechanics predicts that S could take on values as high as $2\sqrt{2}$.

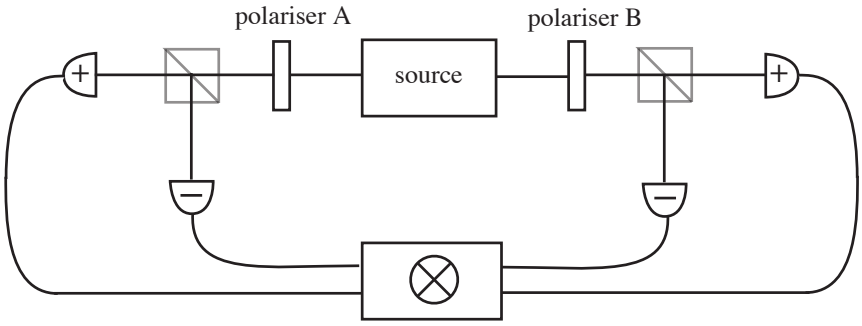

Figure 3.3: The seminal experiment of Aspect et al. measured the polarisation of photons coming from an atomic cascade [6]. The beamsplitters are polarising beamsplitters, hence all of the possible outcomes are measured simultaneously by the four detectors.

3.3.2 Bell experiment with polarisation

With Bell's theorem, one can test whether local HV theories can account for observed correlations, or not. All that is needed is a source of EPR states, and coincidence rates $C_{\pm\pm}$ from measurements on both subsystems. In 1982, this experiment was done on photons coming from a calcium atomic cascade [6], where the correlation function is defined as

$$E(\mathbf{a},\mathbf{b}) = \frac{C_{++}(\mathbf{a},\mathbf{b}) - C_{+-}(\mathbf{a},\mathbf{b}) - C_{-+}(\mathbf{a},\mathbf{b}) + C_{--}(\mathbf{a},\mathbf{b})}{C_{++}(\mathbf{a},\mathbf{b}) + C_{+-}(\mathbf{a},\mathbf{b}) + C_{-+}(\mathbf{a},\mathbf{b}) + C_{--}(\mathbf{a},\mathbf{b})}. \tag{3.8}$$

Fig. 3.3 gives a schematic of the experiment, which consists of a source of the photons, rotatable polarisers and a coincidence counting circuit. The results of this experiment show the coincidence varying sinusoidally as a function of the orientation between the two polarisers ($\Delta\theta$), as predicted by quantum mechanics (3.3). The value of S was 2.697 [6], demonstrating that local HV theories do not suffice to describe the observed correlations.

Note:In tests of this kind, one is always tempted to conclude that quantum mechanics is correct. However, we should note that the objective of Bell's theorem is to prove whether local HV theories are correct or not. No quantum mechanics was invoked in deriving Bell's theorem. The proper conclusion whenever the Bell inequality is violated is that local HV theories are wrong, not that quantum mechanics is correct (although it still is our best description of the observed correlations).

3.3.3 Analogy between polarisation and OAM

The polarisation of light has played an important historical role in the experimental investigation of quantum entanglement. The early experiments on Bell's inequality were performed by measuring polarisation of photons coming from an atomic cascade and later on from spontaneous parametric down-conversion (SPDC) [6, 52, 73, 77, 159]. If we are to perform a Bell experiment by measuring OAM, it is natural to seek an analogy between polarisation and OAM. The polarisation of the two photons from an atomic cascade, when examined individually, is random. However for any given pair, the polarisations are highly correlated (i.e. always opposite). The same is true for OAM. Individually, the photons can have any OAM value, but because OAM is conserved, any given pair will have opposite OAM values [80].

The mathematical analogy between polarisation and OAM states was already recognised in the studies using cylindrical lenses as mode converters in the early 1990s [39, 48]. These mode converters transformed Hermite-Gaussian modes into Laguerre-Gaussian modes and are the equivalent op-

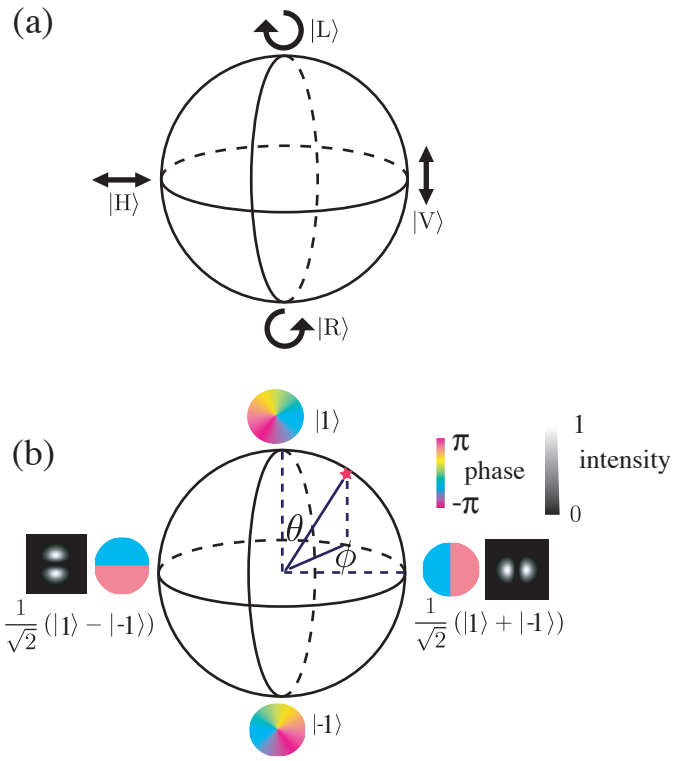

Figure 3.4: Polarisation states can be described in terms of a Poincaré sphere where the North and South poles correspond to the left- and right- circular polarisations. (a) The superpositions of left- and right- circular polarisations are the linear polarisation states which lie on the equator. (b) An analogous sphere can be defined for OAM, with the poles being $|\pm\ell\rangle$. The states on the equator are $2|\ell|$ petal patterns with $2|\ell|$ sectors of alternating 0 and π phase. The angles θ and ϕ define any state (red star) on the OAM Bloch sphere.

tical components to waveplates for polarisation states. This analogy was exploited by Padgett and Courtial [148, 160] in 1999, who proposed a representation of the OAM states on a Bloch sphere equivalent to the Poincaré sphere. The Poincaré sphere represents the complex superposition of two or-

thogonal polarisation states. Right- and left-circular polarisation states are located at the 'North' and 'South' poles of the Poincaré sphere, respectively. Linear polarisation states are situated around the 'equator', where the longitude specifies their orientation, which in turn depends on the relative phase between the right- and left-circular polarisation components. The elliptical polarisations correspond to the intermediate 'latitudes', with the 'longitude' denoting the orientation of the major axis (fig. 3.4).

While polarisation is a two state system, completely described by a Poincaré sphere, OAM is not. However, it is possible to choose any two orthogonal OAM modes and place them in the North and South poles of an OAM Bloch sphere (fig. 3.4). For example, in the case where the North and South poles represent Laguerre-Gaussian modes with $p = 0$ (LG_0^ℓ) and $\ell = 1$ and $\ell = -1$ respectively, we find the Hermite-Gaussian (HG) modes (of order 1). The HG modes represent the coherent equal-amplitude superpositions of $|\ell = 1\rangle$ and $|\ell = -1\rangle$ and they are located at the equator. The orientation of the phase discontinuity of the HG mode depends on the relative phase of $|\ell = 1\rangle$ and $|\ell = -1\rangle$, and is specified by the 'longitude' on the sphere. Analogously, intermediate latitudes correspond to more complicated spatial modes, similar to the elliptical polarisations. In general, for OAM Bloch spheres with OAM states $|\pm\ell\rangle$ at the poles, the equatorial states have intensity cross-sections consisting of a ring of $2|\ell|$ petals of different orientations depending on the relative phase of the $|\pm\ell\rangle$ components. Any vector on the sphere can be described by,

$$|\mathbf{v}\rangle = \cos\left(\frac{\theta}{2}\right)|\ell\rangle + e^{i\varphi}\sin\left(\frac{\theta}{2}\right)|-\ell\rangle \tag{3.9}$$

where the angles θ and φ are the usual inclination and azimuth angles respectively, defined such that $0 \leq \theta < \pi$ and $0 \leq \varphi < 2\pi$. It is possible to construct OAM Bloch spheres for more complicated mode structures, as long as they occupy only two dimensions, as we shall see in the next chapter.

3.3.4 Bell experiment with OAM

Equipped with the analogy between polarisation and OAM, it is straightforward to repeat Bell-type experiments for OAM and OAM superpositions. The first experiments testing a Bell-type inequality using photon polarisation entailed measuring the polarisation of each photon of the pair with polarisers at different relative orientations and measuring the coincidence rates that result [6, 52, 73]. When measuring linear polarisation, changing the relative orientation $\Delta\theta$ is equivalent to traversing the equator of the Poincaré sphere. The coincidence rate is sinusoidally dependent on the difference $\Delta\theta = \theta_A - \theta_B$ (or the sum $\theta_A + \theta_B$ depending on the Bell state used). Therefore, to show a similar violation in an OAM subspace, one needs only to choose an OAM Bloch sphere, and measure states corresponding to its equator. In fig. 3.4.b we have shown the case with $|1\rangle$ and $|-1\rangle$ at the poles, and one could think of the linear polarisations in a similar manner to the orientation of the phase discontinuity.

We measure the OAM of the photon pair along the equator of the equivalent OAM Bloch sphere (fig. 3.4), with holograms (rather than polarisers) of different relative orientations, and analyse the coincidence rates that result (fig. 3.5). We have done this for different two-dimensional OAM subspaces of $|\pm\ell\rangle$. The correlation function $E(\theta_A, \theta_B)$ (3.6) as a function of the ori-

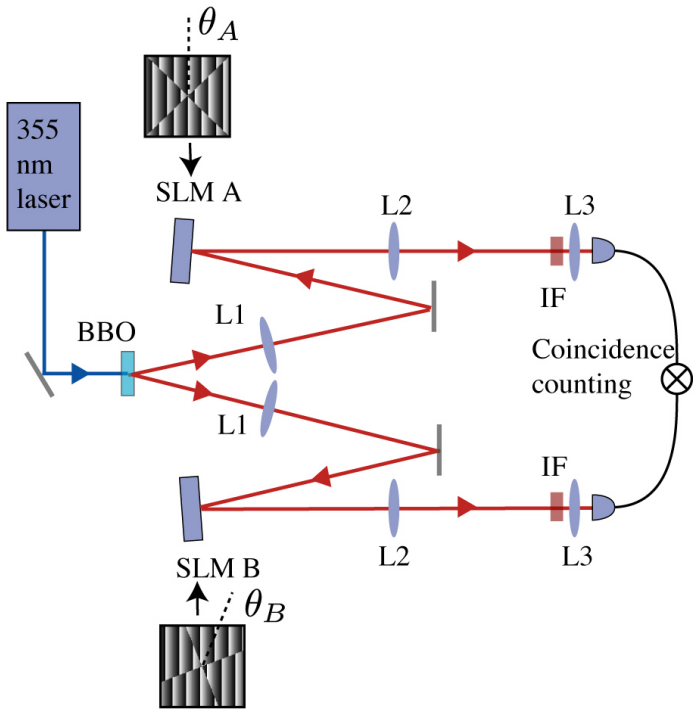

Figure 3.5: The photons come from noncollinear, type 1 SPDC in a 3-mm long BBO crystal. Pinholes are used to select two diametrically opposite sections of the down-converted light, which has an opening cone of 8°. These are each imaged onto separate SLMs (L1=300 mm), where we program the holograms to measure "sector states" (referring to the $2|\ell|$ sectors in the resulting superposition of $|\ell\rangle$ and $|-\ell\rangle$). We show the hologram for $\ell = 2$. The SLMs are imaged through interference filters (IF, centred at 710 nm with a width of 10 nm), onto single-mode fibres (L2=600 mm, L3=1.6 mm) and fed into a coincidence circuit with a coincidence window of 25 ns.

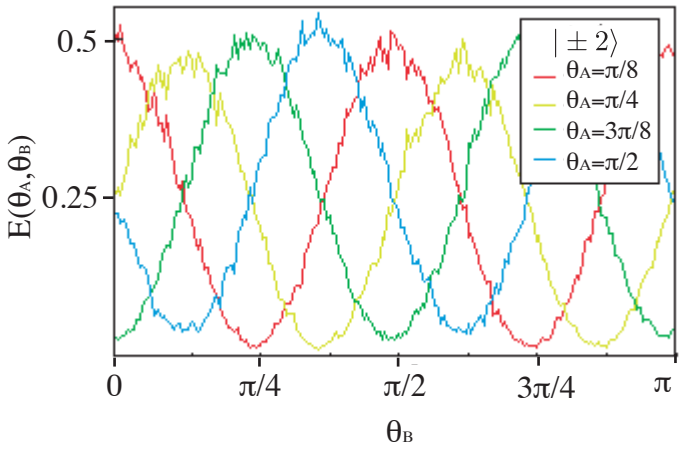

Figure 3.6: As expected, the coincidence as a function of the orientation of hologram B (θ_B) for different fixed orientations of hologram A (θ_A) is sinusoidal. From here we calculate S to be 2.69 ± 0.02. Results shown are for superpositions of $\ell = \pm 2$. [7]

entations of the holograms, for a subspace with the North and South poles corresponding to $|2\rangle$ and $|-2\rangle$ is shown in fig. 3.6. From this set of curves we have calculated S to be 2.69 ± 0.02, a violation of 35 standard deviations. We have also shown a violation of Bell inequalities up to subspaces where $\ell = \pm 24$ [7].

Because SLMs are easily programmable, we need not restrict ourselves to measurements along the equator. It is possible to also measure the analogous states to elliptical polarisation by modulating not just the phase but also the intensity structure of the measured modes (the hologram design with intensity modulation has been discussed in section 2.2). We can access states

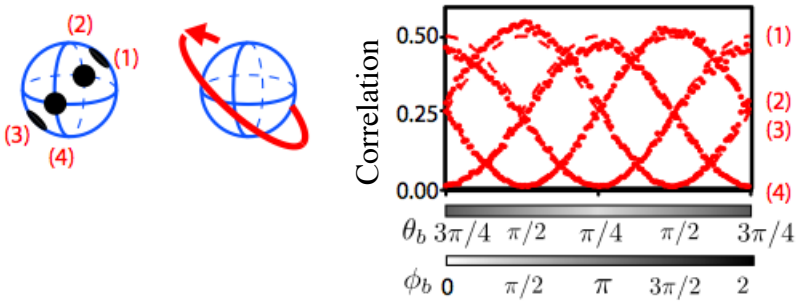

Figure 3.7: Because an SLM can provide both phase and amplitude modulation, measurements on the OAM Bloch sphere need not be restricted to the equatorial plane. We can make measurements on any arbitrary great circle of the sphere. The hologram on SLM1 is fixed so as to measure any of the four states represented by the black dots while the hologram on SLM2 measures states along the skewed plane, the angles θ_b and ϕ_b refer to polar and azimuthal angles respectively. The coincidences are sinusoidal as expected, and we calculate S to be 2.59 ± 0.05. [8]

that lie in an arbitrary great circle of the Bloch sphere, as shown in fig. 3.7. We show results for a subspace of $|\pm 2\rangle$, the coincidence curves are still sinusoidal as expected and we have calculated S from these to be 2.59 ± 0.05 [8].

Note that in our Bell experiments, we did not have the four-channel detection of the original polarisation experiment, [6, 52]. Polarisation is a two-state system, and all possibilities (H and V) can be measured with a polarising beam splitter, the output of which is interpreted as $+, -$. In contrast, OAM is not a two-state system and a device which can conveniently measure all the possible outcomes has only recently been developed [149, 161].

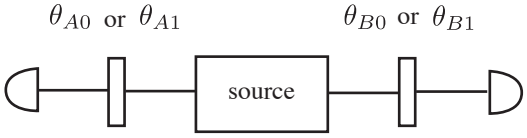

Figure 3.8: A source emits pairs of photons, and each photon is measured by polarisers which are oriented randomly, either along $\theta_{A0}(\theta_{B0})$ or $\theta_{A1}(\theta_{B1})$.

In effect, the holograms that we display on the SLM can only ascertain whether a photon is of a particular spatial mode. Hence, we have to change the correlation function in 3.8 slightly to,

$$E(\theta_a, \theta_b) = \frac{C(\theta_a, \theta_b) - C(\theta_a, \theta_b + \frac{\pi}{2\ell}) - C(\theta_a + \frac{\pi}{2\ell}, \theta_b + C(\theta_a + \frac{\pi}{2\ell}, \theta_b + \frac{\pi}{2\ell})}{C(\theta_a, \theta_b) + C(\theta_a, \theta_b + \frac{\pi}{2\ell}) + C(\theta_a + \frac{\pi}{2\ell}, \theta_b + C(\theta_a + \frac{\pi}{2\ell}, \theta_b + \frac{\pi}{2\ell})}, \tag{3.10}$$

where we note that the orientation of the hologram which is orthogonal (i.e. will give no coincidences) to θ is $\theta + \frac{\pi}{2\ell}$.

3.3.5 Best version of Bell's theorem

Thirty years after Bell put forth his theorem to falsify local hidden variable theories, Hardy formulated a paradox challenging the idea of locality and hidden variables. The Hardy paradox is, in a way, more obvious and does not resort to any inequality [69]. Mermin calls the Hardy paradox the "best version of Bell's theorem [162, 163]. We outline the original Hardy paradox as presented by Carlson using photon polarisation [164] .

We consider two photons, which go in different directions, towards sepa-

rate measurement apparatus (fig. 3.8) consisting of a polariser and detector (assumed with 100% efficiency). In each run of the experiment, the detectors receive a photon from the source (which is not connected to either measuring apparatus). Before the photons arrive at the polarisers, but after they are released from the source so as to discount any more "prior agreement" and any correlation can be attributed to the source, Alice and Bob choose the orientation of their respective polarisers. Alice randomly orients her polarisers to θ_{A0} or θ_{A1} (a click on the detector then denotes that the photon was polarised along θ_{A0} or θ_{A1}, respectively). Bob performs similar measurements and randomly orients his polarisers to θ_{B0} or θ_{B1} (fig. 3.8). They then compare the joint probability, $P(\theta_{Ai}, \theta_{Bj})$, that Alice measures a photon with polarisation θ_{Ai} and Bob measures a photon with polarisation θ_{Bj}, and the conditional probability $P(\theta_{Bj}|\theta_{Ai})$, that Bob measures a photon with polarisation θ_{Bj} given that Alice measured a photon with polarisation θ_{Ai}. For suitable polarisation angles θ_{A0}, θ_{A1}, θ_{B0}, θ_{B1}, they observe that:

(a) $P(\theta_{A1}, \theta_{B1}) = 0.09$, that is if Alice measures with θ_{A1} and Bob with θ_{B1}, they will both detect photons 9% of time (the fraction 9% will become clear later).

(b) $P(\theta_{B0}|\theta_{A1}) = 1$, that is if Alice detects a photon with polarisation θ_{A1}, Bob will detect a photon with polarisation θ_{B0}.

(c) $P(\theta_{A0}|\theta_{B1}) = 1$, that is if Bob detects a photon with polarisation θ_{B1}, Alice will detect a photon with polarisation θ_{A0}.

We will now use (a) to (c) to infer what will happen if Alice and Bob choose to orient their polariser to θ_{A0} and θ_{B0}, respectively. Suppose that

Alice sets to measure a photon polarised along θ_{A1} and Bob sets to measure a photon polarised along θ_{B1} (a). At the last moment, Bob decides he will measure along θ_{B0} instead, what can we expect? Since Alice's polariser is oriented along θ_{A1} and (b) is true, we expect Bob to measure a photon with polarisation θ_{B0}. If instead, Alice is the one that changes her mind and decides to measure along θ_{A0} instead, what can we expect? Since Bob's polariser is oriented along θ_{B1} and (c) is true, we expect Alice to measure a photon with polarisation θ_{A0}. If both Alice and Bob change their mind, and measure along θ_{A0} and θ_{B0}, what can we expect? This is just a combination of the two previous situations, and it is natural to conclude that Alice measures a photon with polarisation θ_{A0} and Bob measures a photon with polarisation θ_{B0}. Hence, with the reasonable assumption that the polarisations of the photons are independent of the detector settings and that the photons have a defined polarisation, $P(\theta_{A0}, \theta_{B0}) > 0$. The paradox is that, when this experiment is done on the photon pairs, they find that,

(d) $P(\theta_{A0}, \theta_{B0}) = 0$, that is Alice and Bob never find photons which have polarisations θ_{A0} and θ_{B0}.

This result clearly contradicts our theoretical expectation which came from a logical reasoning based on (a) to (c). It is imperative to question the assumptions that led us to our prediction. We assumed that Alice's and Bob's measurements are independent and have no influence on each other–the locality assumption. We also assumed that it is sensible to talk of photon polarisation"while the photon is in flight", essentially, that the polarisation of the photons were determined at the source. These assumptions are rea-

sonable in a classical world, but the fact that (d) is true hints that at least one of these assumptions is false.

The strength of the Hardy paradox is that it is so simple and concise [162, 163]. It does not involve any inequality and we just need to show the apparently paradoxical observations in (a) to (d). Note that in the Hardy paradox, we can not predict with certainty every outcome of a remote measurement (for example, if Alice and Bob set their polarisers along θ_{A1} and θ_{B1}, and Alice detects a photon on her side, she can only predict that Bob detects a photon polarised along θ_{B1} correctly 9% of the time). In this sense, not all photon pairs require a "prior agreement" (only pairs that are correlated), and so the Hardy paradox does not invoke EPR's "elements of reality". The states that satisfy the Hardy paradox are less correlated than those that demonstrate the EPR paradox. However despite the absence of some "prior agreements" on some of the photons (not very many, [163]), the correlations that continue to be perfect are sufficient to guarantee the absence of photons with polarisations θ_{A0} and θ_{B0}.

This demonstration is not limited to polarisation, so we can generalise to any two dichotomic observables, A and B. Alice measures in either of two bases A_0 or A_1, Bob measures in either B_0 or B_1. $P(A_i, B_j)$ is defined as the joint probability of obtaining $A_i = 1$ and $B_j = 1$, while $P(\bar{A}_i, B_j)$ is that of $A_i = -1$ and $B_j = 1$. Assuming local hidden-variable theory is true, if the three conditions: (I) $P(A_0, B_0) = 0$, (II) $P(\bar{A}_0, B_1) = 0$ and (III) $P(A_1, \bar{B}_0) = 0$ hold, we can conclude that (IV) $P(A_1, B_1) = 0$. However, for specific measurements, quantum mechanics allows for the case where $P(A_1, B_1) > 0$.

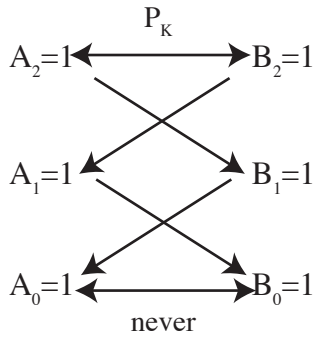

Figure 3.9: If there is a nonzero probability of obtaining the result $A_2 = 1$ and $B_2 = 1$, local realism together with the relations (3.12) and (3.13) implies that there is also a nonzero probability of obtaining the result $A_0 = 1$ and $B_0 = 1$, however experiments contradict this.

3.3.6 Ladder version of the Hardy paradox

The fraction of photons which can demonstrate a conflict with local realism in the original Hardy paradox (the Hardy fraction) is just 0.09. Hardy and co-workers [165] suggested that this can be increased by employing a 'ladder' of probabilities. They demonstrated this using polarisation entangled photons. Alice and Bob measure $K + 1$ dichotomic observables, $\{A_k\}$ and $\{B_k\}$ respectively, where $k = 0, 1, \cdots K$. The original Hardy paradox is when K=1. In order to demonstrate the ladder version of the Hardy paradox, we need to choose $\{A_k\}$ and $\{B_k\}$ such that the following chain of probabilities is true.

$$P(A_0, B_0) = 0 \tag{3.11}$$

$$P(\bar{A}_{k-1}, B_k) = 0, \tag{3.12}$$

$$P(A_k, \bar{B}_{k-1}) = 0, \tag{3.13}$$

$$P(A_K, B_K) > 0 \tag{3.14}$$

With this, the Hardy fraction, $P_K = P(A_K, B_K)$ can be increased up to 0.5.

We will take the case for K=2 (fig. 3.9). Let us assume Alice and Bob set their polarisers to A_2 and B_2 respectively, and both detectors clicked (thus $A_2 = 1$ and $B_2 = 1$). Assuming local realism, it follows from the result $A_2 = 1$ and (3.13) that if Bob measured B_1 instead, his detector will click and thus the result $B_1 = 1$. Similarly, from the result that $B_2 = 1$ and (3.12), it follows that if Alice measured A_1 instead, her detector will click and thus the result $A_1 = 1$. This is now one step down the ladder. We can then consider the results $A_1 = 1$ and $B_1 = 1$ together with (3.13) and (3.12) respectively (i.e. suppose Alice and Bob change their minds again!) to arrive at the results $A_0 = 1$ and $B_0 = 1$. Hence, with local realism as an assumption and statements (3.12) and (3.13), we are led to conclude that if we observe the result $A_2 = 1$ and $B_2 = 1$, we should observe the result $A_0 = 1$ and $B_0 = 1$ at least some of the time. However, the case where $P(A_0, B_0) > 0$ is not observed in experiments.

Before the Hardy experiment with OAM is described, it is important to mention another major difference between the Hardy paradox and Bell-type tests. The maximum violation of the Bell inequality occurs when the state in consideration is maximally entangled. This is not true for demonstrations of the Hardy paradox. The Hardy paradox can not be shown for maximally entangled states because the proof relies on a certain lack of symmetry which is absent in maximally entangled states [69]. This makes a source of non-maximally entangled photons necessary. To show the Hardy paradox using photon polarisation, clever arrangements of wave plates and Fresnel rhomb rotators have been implemented to vary the degree of entanglement,

while the correlations were inferred from Hong-Ou-Mandel peaks (dips) [165]. Measuring OAM (instead of polarisation) presents an advantage in this case because, as we have seen in the previous chapter, SPDC naturally results to non-maximally entangled OAM states.

3.3.7 Ladder version of the Hardy paradox with OAM

Since the pump has zero OAM, the two-photon state in terms of the OAM basis can be written as,

$$|\Psi\rangle_{\text{SPDC}} = \sum_{\ell} \sum_{p_s,p_i} C^{\ell,-\ell}_{p_s,p_i} |\ell, p_s\rangle |-\ell, p_i\rangle, \tag{3.15}$$

where $|C^{\ell,-\ell}_{p_s,p_i}|^2$ is the probability of finding a signal photon in $|\ell, p_s\rangle$ and an idler photon in $|-\ell, p_i\rangle$. We restrict our measurements to the case where $p = 0$ and subsequently denote $|\ell, p_{s,i} = 0\rangle$ as $|\ell\rangle$. To implement the Hardy paradox in OAM, we first need knowledge of the available OAM states. The different OAM states have different weightings, and these weightings make up the spiral spectrum [118]. We first build up the spiral spectrum, measuring $|\ell\rangle$ and $|-\ell\rangle$ by encoding forked diffraction holograms in the SLMs of the setup shown in fig. 3.10. We model the spiral spectrum as $C^{\ell,-\ell}_{0,0} = C_\ell = \zeta^{|\ell|}$, where we find $\zeta = 0.66 \pm 0.02$ from an empirical fit (fig.3.12.a). In reality, ζ is a function of the pump and detection waists, and the phase-matching conditions [88, 3]. The important thing to note is that given an SPDC setup, the spiral spectrum can be obtained experimentally and this can be parametrized in terms of $|\ell|$ (fig.3.12.a). This gives us a naturally non-maximally entangled two-photon state, and given the knowledge of the

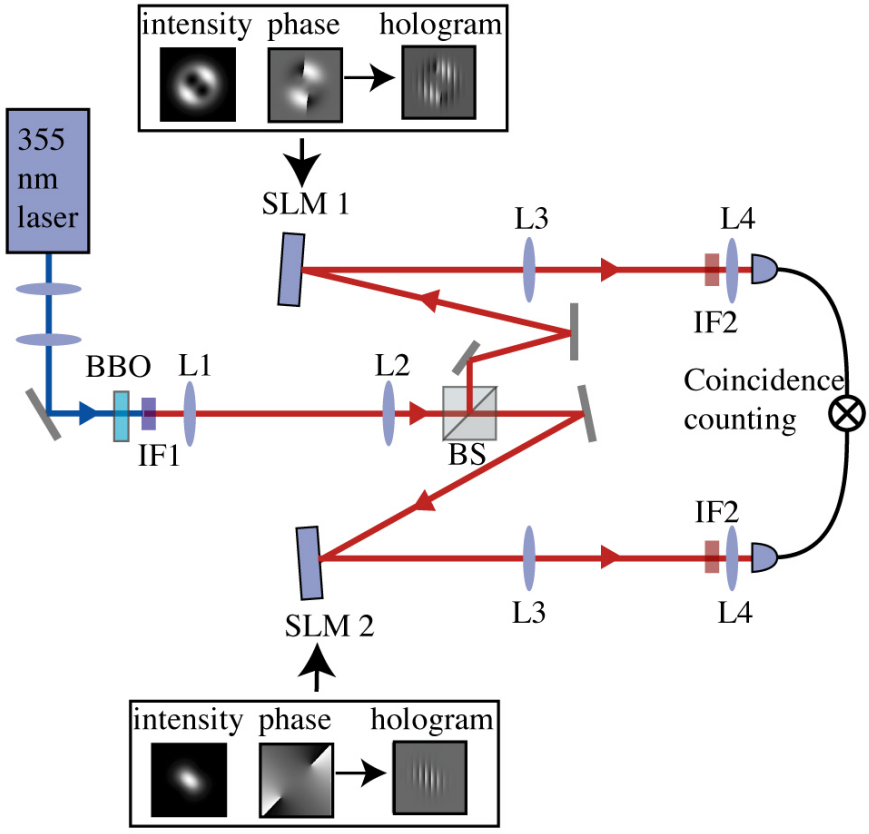

Figure 3.10: We have collinear SPDC from a 5-mm BBO crystal as source of our entangled photons. The crystal is imaged by a telescope (L1=200 mm, L2=400 mm) onto separate SLMs, where we encode the Hardy measurement states (sample intensity, phase and holograms are shown on insets). The SLMs are again imaged by L3(f=600 mm) and L4(f=2.0 mm) onto the facet of single-mode fibres through 2 nm wide interference filters centred at 710 nm.

spiral spectrum we can choose different OAM subspaces with varying degrees of entanglement.

With the knowledge of the spiral spectrum, we choose two OAM states $|m\rangle_A$ and $|n\rangle_A$ to span the possible states of the signal photon. As a consequence of the conservation of OAM [80], the states of the idler photon will be spanned by $|-m\rangle_B$ and $|-n\rangle_B$. The non-maximally entangled state is naturally post-selected,

$$|\Psi\rangle_{\mathrm{m,n}} = \frac{1}{\sqrt{1+\varepsilon^2}} \left(\varepsilon|m\rangle_A|-m\rangle_B + |n\rangle_A|-n\rangle_B\right), \tag{3.16}$$

where $\varepsilon = C_m/C_n \approx \zeta^{|m|-|n|}$ denotes the degree of entanglement ($\varepsilon = 1$ for maximally entangled), depending on the chosen OAM bases. For the ladder version of Hardy's paradox, we define the following $K+1$ OAM measurement bases, $\{A_k, A_k^{\perp}\}$ and $\{B_k, B_k^{\perp}\}$, for signal and idler photons, respectively:

$$\begin{bmatrix} |A_k\rangle \\ |A_k^{\perp}\rangle \end{bmatrix} = \begin{bmatrix} \cos\theta_k & i\sin\theta_k \\ i\sin\theta_k & \cos\theta_k \end{bmatrix} \begin{bmatrix} |+m\rangle_A \\ |+n\rangle_A \end{bmatrix}, \tag{3.17}$$

$$\begin{bmatrix} |B_k\rangle \\ |B_k^{\perp}\rangle \end{bmatrix} = \begin{bmatrix} \cos\theta_k & i\sin\theta_k \\ i\sin\theta_k & \cos\theta_k \end{bmatrix} \begin{bmatrix} |-m\rangle_B \\ |-n\rangle_B \end{bmatrix}. \tag{3.18}$$

By substituting (3.17) to (3.18) into (3.11) to (3.14), we have

$$\tan\theta_k \;=\; (-1)^k \times \zeta^{(2k+1)(|m|-|n|)/2}. \tag{3.19}$$

Subsequently, the Hardy fraction in terms of the degree of entanglement is

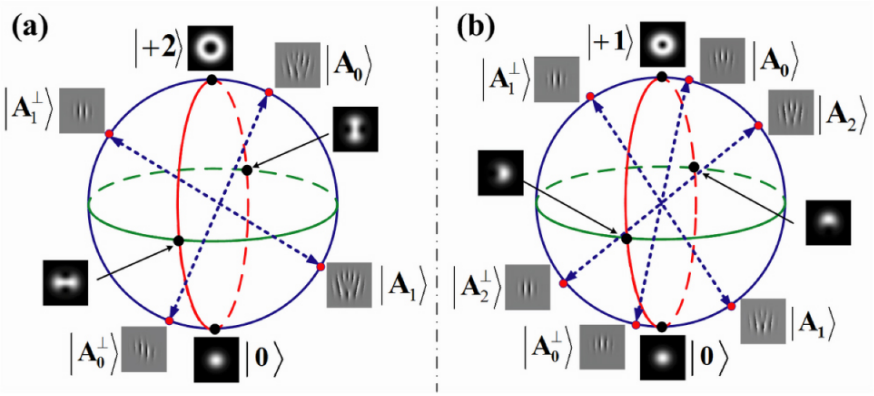

Figure 3.11: The Bloch spheres for our Hardy test: (a) $|+2\rangle$ and $|0\rangle$; (b) $|+1\rangle$ and $|0\rangle$. We show the intensity of the modes on the poles and some representatives on the equator. We also show the holograms required for Alice's measurements (Bob's not shown).

given by

$$P_K = |\langle A_K|\langle B_K|\Psi\rangle_{\mathrm{m,n}}|^2 = \frac{\varepsilon^2}{1+\varepsilon^2}\left(\frac{1-\varepsilon^{2K}}{1+\varepsilon^{2K+1}}\right)^2. \tag{3.20}$$

This is maximal at 0.09 for K=1 and $\varepsilon = 0.66$, as in the original formulation of the Hardy paradox. The maximally entangled state corresponds to the case where $\varepsilon = 1$, giving $P_K = 0$, implying that the Hardy paradox can not be shown for maximally entangled states.

In contrast to [165, 166], the degree of entanglement in our experiment is $\varepsilon = 0.66^{|m|-|n|}$ and can be easily varied simply by choosing different OAM bases, $|m\rangle$ and $|n\rangle$. The required measurements prescribed in (3.17) and (3.18) consisting of a nontrivial superposition of OAM states can be conveniently implemented using SLMs [167].

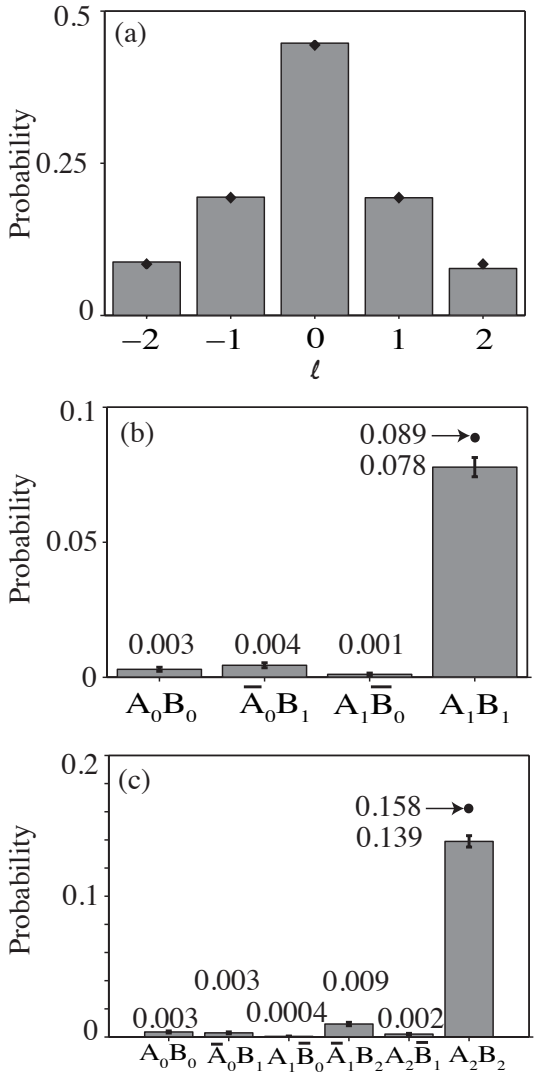

Figure 3.12: The weights of the various $|\ell, p = 0\rangle$ states we obtain from our experiment is shown in (a), the dots correspond to an empirical fit. OAM entanglement from SPDC is naturally non-maximally entangled. Results for the cases where K=1 and K=2 are shown in (b) and (c) respectively. Apart from the probabilities for A_1B_1 and A_2B_2, all the rest are low, as expected. The black dots represent theoretical prediction for P_K.

Without loss of generality, we take two states, $|\Psi\rangle_{2,0}$ and $|\Psi\rangle_{1,0}$, to demonstrate the Hardy paradox with $K = 1$ and $K = 2$, respectively (fig. 3.11). The corresponding degrees of entanglement, $\varepsilon(2,0) = 0.43$ and $\varepsilon(1,0) = 0.66$, are known from the measured spiral bandwidth (fig. 3.12.a). Based on (3.17) and (3.18), we can calculate the states to be measured, and represent them on the asymmetric Bloch spheres, we show the holograms to measure the states $|A_k\rangle$ and $|A_k^{\perp}\rangle$ (fig. 3.11). We illustrate the case of K=1 more closely for which we choose $m = 2$ and $n = 0$. In fig. 3.10, we show the intensity and phase of the states we want to measure ($|A_0\rangle$ in SLM_A and $|B_0\rangle$ in SLM_B,) and the holograms we use to detect these which follow from the recipe in section 2.2.

Our results are shown in fig. 3.12.b and 3.12.c. We obtain $P_1 = 0.078 \pm 0.004$ for $|\Psi\rangle_{2,0}$ and $P_2 = 0.139 \pm 0.005$ for $|\Psi\rangle_{1,0}$, both in close agreement with theory. These values are slightly less than the theoretical predictions of 0.089 and 0.158 from (3. 10), respectively. The difference can be attributed to slight misalignment (the nonzero probabilities for the other measurements show that there is some crosstalk between the modes) and non-uniformity in the diffraction efficiency of the different holograms used (we have been stringent in calculating the probabilities and we did not correct for these differences). All other probabilities are low as anticipated, thereby demonstrating the Hardy paradox.

3.4 Nonlocal hidden variable theory

Local hidden variable theory has satisfactorily been discounted by Bell-type experiments. In addition, the demonstration of the Hardy paradox in the laboratory has highlighted the nonlocality of quantum mechanics even more. The next question is whether the apparently nonlocal correlations can be explained by nonlocal hidden variables.

3.4.1 Leggett inequality and nonlocal hidden variables

In 2003, Leggett developed a theorem analogous to Bell's theorem, he formulated an inequality which serves as a test for a class of nonlocal HV theories [70]. Leggett introduced a nonlocal HV theory, trying to explain nonlocal correlations while maintaining sharply defined individual properties of the subsystems. The Leggett inequality is relatively new and has not been tested as extensively as the Bell inequality. However, conclusive experimental violations have recently been demonstrated using polarisation states of photons, thereby ruling out this class of nonlocal HV theories [168, 169, 170, 171, 172].

Mathematically, a correlation can be defined by a conditional probability distribution $P(\alpha, \beta|\mathbf{a}, \mathbf{b})$, where α and β are the outcomes of measurements $\mathbf{a}$ and $\mathbf{b}$ made on systems A and B respectively (e.g. $\mathbf{a}$ and $\mathbf{b}$ could be the orientation of polarisers). If the outcomes are predetermined by HVs λ (thus imposing realism), and if in addition these HVs are local (*i.e.* spatially separated measurements are independent of each other), the conditional

probability becomes

$$P_\lambda(\alpha, \beta|\mathbf{a}, \mathbf{b}) = P_\lambda(\alpha|\mathbf{a})P_\lambda(\beta|\mathbf{b}). \tag{3.21}$$

Imposing locality in the HVs sets a limit to the correlations that can be achieved in experiments, expressed in Bell's ubiquitous inequality [66, 67, 68]. To date, results of various experiments have been shown to violate the Bell inequality and its derivatives, such as the CHSH inequality, leaving one to conclude that realism and locality cannot hold simultaneously [6, 19, 52]. Whether to abandon the notion of realism or locality is a question which has attracted much speculation [173, 174].

Leggett considered a different HV model in which the condition of locality is relaxed. He analysed a family of nonlocal HV theories and derived an inequality which would be satisfied by systems which abide by his model. In accordance to Leggett's model, the detection of photons emitted from SPDC has the following properties: (i) each pair of photons has a characteristic set of HVs λ; (ii) the ensemble of photon pairs is determined by a statistical distribution of values of λ, $\rho(\lambda)$, which depends only on the source, hence allowing one to write

$$P(\alpha, \beta|\mathbf{a}, \mathbf{b}) = \int d\lambda \rho(\lambda) P_\lambda(\alpha, \beta|\mathbf{a}, \mathbf{b}). \tag{3.22}$$

(iii) the outcome of a measurement on each photon, α, may depend on $\mathbf{a}$, $\mathbf{b}$, λ and β (i.e. (3.21) is not necessarily satisfied, doing away with locality); (iv) each photon of the pair, associated with the parameter λ, individually behaves as if it has well-defined properties (or OAM, in our case), and a

measurement on it (conditioned on λ) will show sinusoidal intensity variations (known as Malus' law for polarisation) [70]. This model is attractive because the properties of the individual photons are sharply defined, allowing one to make deterministic predictions locally on the measurement results of each photon. Moreover, the HVs are nonlocal and may depend on parameters outwith the neighbourhood of the measurement apparatus. These properties lead to an incompatibility theorem, called the Leggett inequality. This inequality has been refined in recent work to be experimentally testable with a finite number of measurements and obviating the need for rotational invariance [169, 170]. Following these recent refinements, for N possible measurement settings in system A, the correlations of a photon pair that obeys Leggett's nonlocal hidden variable model are restricted by the inequality [171]

$$\frac{1}{N}\sum_{i=1}^{N}|E(\mathbf{a}_i,\mathbf{b}_i)+E(\mathbf{a}_i,\mathbf{b'}_i)| \equiv L_N(\chi) \leq 2-2\eta_N\left|\sin\frac{\chi}{2}\right| \tag{3.23}$$

if

$$\frac{1}{N}\sum_{i=1}^{N}|\vec{v}\cdot\vec{e}_i| \geq \eta_N \tag{3.24}$$

holds for any vector $\vec{v}$. Here, $E(\mathbf{a},\mathbf{b})$ and $E(\mathbf{a},\mathbf{b'})$ are the correlation coefficients for measurement settings **a**,**b** and **a**,**b'** respectively, similar to (2.11).

3.4.2 Measurement settings

Quantum mechanics allows for vectors that violate the inequality (3.23). Again we use the idea of Bloch spheres, which apply to both polarisation

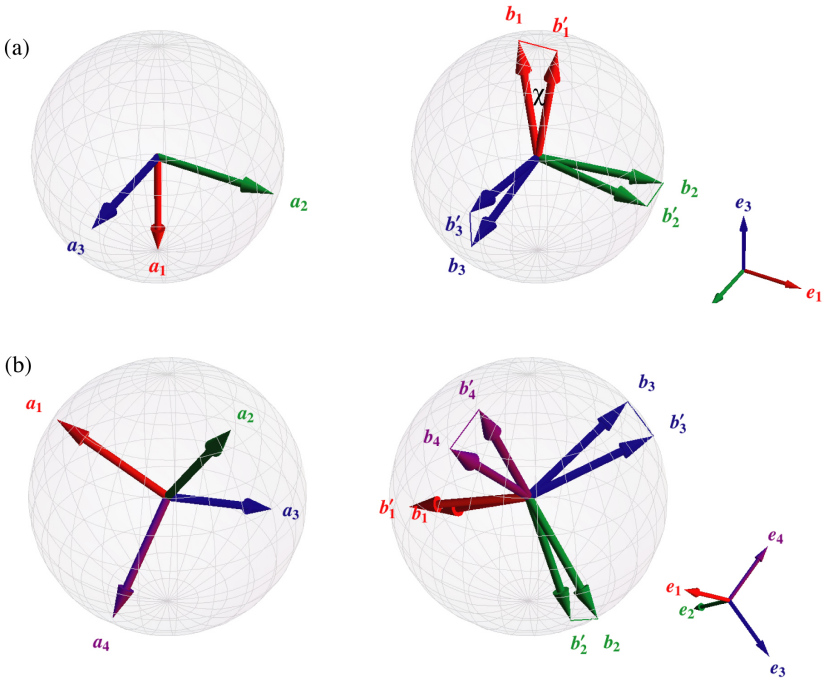

Figure 3.13: (a)For $N = 3$, SLM A is set to measure the three mutually orthogonal states $\mathbf{a}_1$, $\mathbf{a}_2$ and $\mathbf{a}_3$. SLM B is then set to measure coplanar states $\mathbf{b}_i$, $\mathbf{b'}_i$ separated by an angle χ where $\mathbf{b}_i - \mathbf{b'}_i$ is parallel to $\mathbf{e}_i$ which are mutually orthogonal. (b) For $N = 4$, $\mathbf{a}_1$, $\mathbf{a}_2$, $\mathbf{a}_3$ and $\mathbf{a}_4$ are the vertices of a tetrahedron. The vectors $\mathbf{e}_1$, $\mathbf{e}_2$, $\mathbf{e}_3$ and $\mathbf{e}_4$ are then vertices of a regular tetrahedron. Violating the inequality requires measurements in four different non-orthogonal planes. In our case, we chose the planes defined by $\mathbf{e}_1$ and $\mathbf{e}_2$, $\mathbf{e}_2$ and $\mathbf{e}_3$, $\mathbf{e}_3$ and $\mathbf{e}_4$ and $\mathbf{e}_4$ and $\mathbf{e}_1$. [9]

and OAM (or in general, any space spanned by two orthogonal states). We choose $\mathbf{b}_i$ and $\mathbf{b'}_i$ that are separated by angle χ and we define $\mathbf{e}_i = \mathbf{b}_i - \mathbf{b'}_i$. We choose $\mathbf{a}_i$, $\mathbf{b}_i$ and $\mathbf{b'}_i$ such that we get maximum coincidence between $\mathbf{a}_i$ and $\mathbf{b}_i + \mathbf{b'}_i$. This means that $\mathbf{b}_i + \mathbf{b'}_i$ has the same azimuth angle as $\mathbf{a}_i$ but reflected about the equator. The constant η_N depends on the

geometry of the $\mathbf{e}_i$'s, defined as in fig. 3.13. Measurements with $N = 3$ have been done previously in the polarisation state space [170, 171, 172], with $\eta_3 = \frac{1}{3}$ (calculated by minimising the left hand side of inequality (3.24)), and $\mathbf{a}_1$, $\mathbf{a}_2$ and $\mathbf{a}_3$ pointing to the coordinate axes (fig. 3.13.a). Increasing N leads to more robust inequalities, albeit with more sophisticated alignment requirements if working with polarisation [172]. Increasing N becomes more feasible with the flexibility introduced by SLMs because of the ability to specify any arbitrary state. We demonstrate this by showing a violation for $N = 4$ where the largest violation is found for $\mathbf{e}_i$'s being the vertices of a regular tetrahedron (fig. 3.13.b). In this case $\eta_4 = \frac{1}{\sqrt{6}}$, and we choose $\mathbf{a}_1$, $\mathbf{a}_2$, $\mathbf{a}_3$ and $\mathbf{a}_4$ to be vertices of a tetrahedron, as shown in fig.3.13.b, for maximal violation of the inequality. For both cases, quantum mechanics predicts that $L_N(\chi) = 2\cos\left|\frac{\chi}{2}\right|$, violating the inequality (3.23) over a large range of angles, χ.

3.4.3 Testing Leggett inequalities with OAM

Our measurements are defined in an OAM Bloch sphere where the North and South poles are $|+2\rangle$ and $|-2\rangle$ respectively. Hence our vectors $\mathbf{v}$ are described by

$$|\mathbf{v}\rangle = \cos\left(\frac{\theta}{2}\right)|2\rangle + e^{i\varphi}\sin\left(\frac{\theta}{2}\right)|-2\rangle. \tag{3.25}$$

As in the previous experiments, we measure OAM states holographically by programming the SLMs. Measuring the violation of a Bell inequality [7] required measurement of states on orthogonal great circles of the OAM Bloch sphere (e.g. along the equator, 0th and 180th meridians). In the case

of the Leggett inequality, the use of SLMs is even more beneficial because it requires measurements of states along non-orthogonal great circles (*i.e.* the measurement planes are not orthogonal). The SLMs enable us to measure quantum correlations between arbitrary states, positioned at any point of the Bloch sphere, conveniently and with high accuracy.

Our experimental setup is shown in fig. 3.14. This is the same setup we used for the EPR experiment with OAM, apart from the holograms being displayed. The measurements require modulation of both intensity and phase as in the case of the Hardy paradox. The results for $N = 3$ and $N = 4$ are shown in fig. 3.15. Each datapoint in these plots corresponds to three settings, $\mathbf{a_i}$, for measurements on system A and $\mathbf{b_i}$ and $\mathbf{b'_i}$ separated by an angle χ in system B, as indicated in. fig. 3.13 thus requiring $2N^2$ measurements per angle.

We measure the coincidence as we vary the angle χ and compare it to the maximal value of L_N allowed by Leggett's mode as defined in (3.23). Our results, depicted in fig. 3.15, show that the experimental data follows the prediction of quantum mechanics closely, as expected and that the inequality is violated over a large range of angles. For N=3, we observe the maximum violation at $\chi = -42^o$ where $L_3 = 1.88 \pm 0.02$. For N=4, the maximum violation occurs at $\chi = -30^o$ where $L_4 = 1.93 \pm 0.02$. These results imply that it is not possible to keep definite, individual OAM states of the photons while maintaining the observed OAM correlations.

This is the first experimental violation of the Leggett inequality outside a polarisation state space. Our measurements in the OAM state space violate the Leggett inequality by 5 and 6 standard deviations respectively for

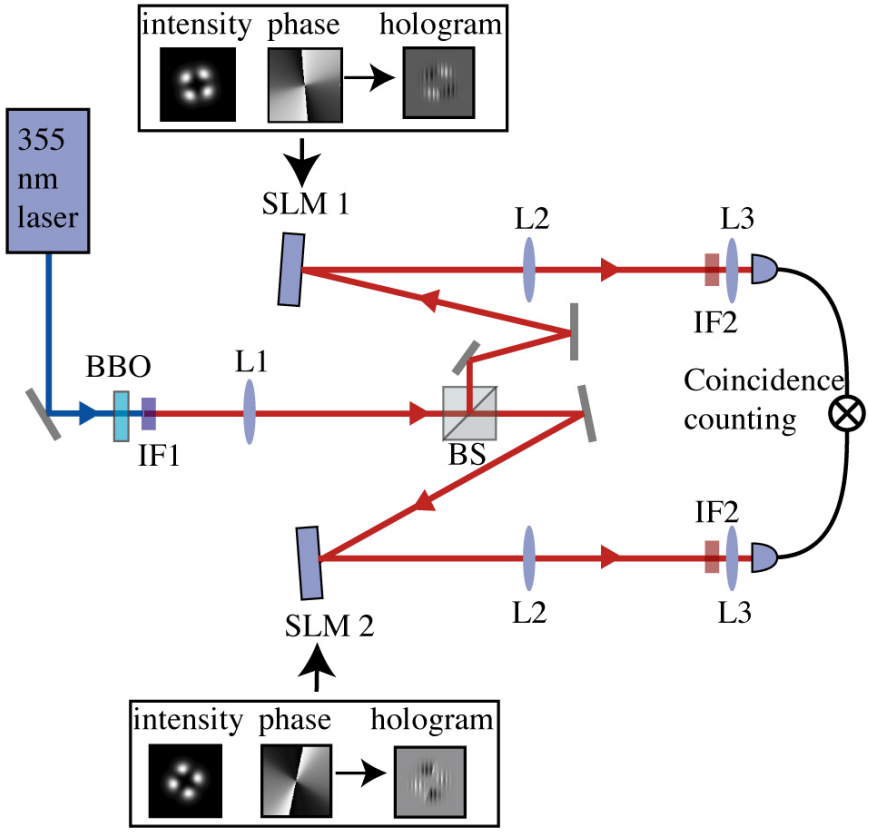

Figure 3.14: We have SPDC from a 3-mm BBO crystal as source of our entangled photons. The crystal is imaged by L1 (f=300 mm) onto separate SLMs, where we encode the holograms shown(sample intensity, phase and holograms are shown on insets). The SLMs are imaged by L2(f=600 mm) and L3(f=1.6 mm) onto the facet of single-mode fibres through 2 nm wide interference filters centred at 710 nm.

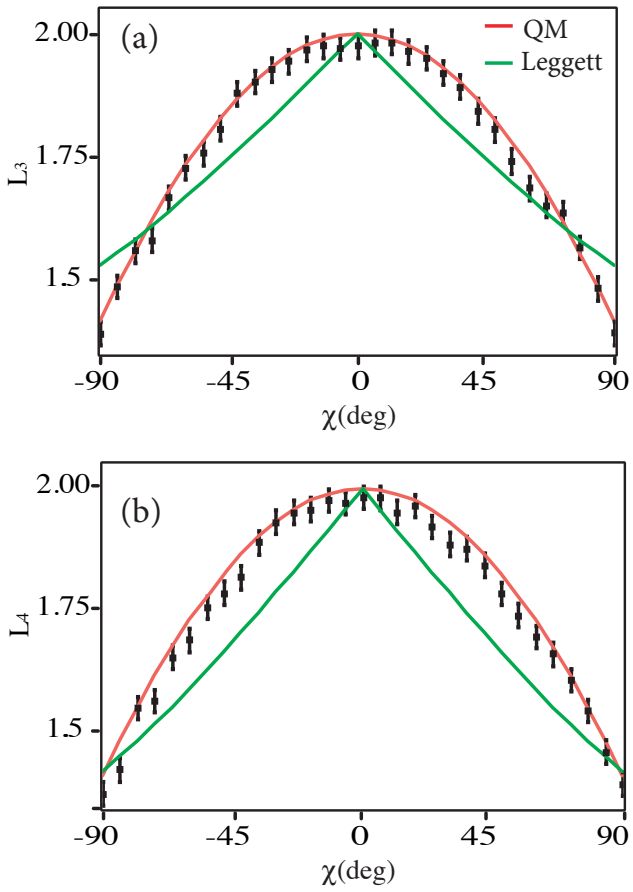

Figure 3.15: Experimentally measured correlations (black dots) for $N = 3$ (a) and $N = 4$ (b) violate the bound arising from Leggett's model (green line), and follow closely the predictions of quantum mechanics (red line). Maximum violation (boxed data points) occurs at -42^o and -30^o respectively for N=3 and N=4 respectively. [9]

$N = 3$ and $N = 4$. The conclusions reached by performing a test of the Leggett inequality, whether in an OAM subspace or in polarisation space, are the same, supporting quantum theory against a specific class of nonlocal hidden variable theory. However, the OAM space offers a much more accessible state space owing to the programmability of SLMs, and less stringent alignment requirements. This is exemplified by our measurements for N=4. Experiments with higher N are practically possible and may prove to be more robust as is speculated [171].

3.5 Conclusion

The peculiarities of quantum mechanics can be demonstrated with OAM and its conjugate variable, angular position. We have started with the question that EPR stirred– is quantum mechanics a complete theory? OAM and angle are also Fourier related like the original EPR variables, position and linear momentum. OAM and angle are different from other degrees of freedom, in that the former is discrete and infinite-dimensional, the latter is continuous and periodic. Nonetheless, our EPR results confirm the result of previous EPR demonstrations, which leads us to challenge either the completeness of quantum mechanics, or the notion of locality.

To answer the question of completeness, we have tested both local and nonlocal hidden variable theories. We have violated the CHSH Bell inequality in two-dimensional OAM subspaces, again discounting local hidden variables as an explanation for observed correlations. We have also demonstrated a ladder version of the Hardy paradox with OAM. An apparently logically

consistent set of statements (from the point of view of local hidden variable theory at least) is shown to be in conflict with our observed correlations. Here the limited range of OAM modes produced by SPDC helps us to easily choose different degrees of entanglement to vary the fraction of photons that demonstrate the Hardy paradox. We have also discounted a general class of nonlocal hidden variable theories by violating a Leggett-type inequality. Hence we can conclude that even if we give up on locality, observed correlations still can not be explained by a hidden variable theory.

From a technological standpoint, the introduction of SLMs has allowed us to access any point on the OAM Bloch sphere–it is just a matter of programming the mode displayed on the SLM. This is one useful advantage over polarisation. In the case of polarisation, in fact, any arbitrary point on the Poincaré corresponds to an elliptical polarisation which is not straightforwardly measurable with just one optical component.

As we have highlighted at the beginning of the chapter, the results that we present here are rather "superfluous". Mainstream physicists believe quantum mechanics to be true, so what is the point of doing all these quantum tests? For one, it is assuring that our results are consistent with experiments done previously for other variables. By restricting measurements to a two-dimensional subspace, such that an analogy with the Poincaré sphere for polarisation is maintained, many of the experiments originally performed with polarisation can be repeated using holograms or phase plates rather than polarisers. Rather than focus on the "superfluousness", we view these results as a challenge: we have established that OAM is an accessible degree of freedom with which to explore quantum mechanics, what do we do next?

There are many possibilities (from blue sky to practically useful!), and we hope that future research directions will exploit the (much discussed, but seldom exploited) inherent high-dimensionality of OAM.

Chapter 4

Entanglement of Optical Vortices

Laguerre-Gaussian (LG) beams naturally contain a phase singularity at their centres. For LG beams, the phase singularities trace a line upon propagation. The Poynting vector rotates around this line, hence the term optical vortex. In certain superpositions of LG beams, the optical vortices can trace more complex structures, such as Hopf links consisting of a pair of optical vortex loops that are linked. We can measure photons in these spatial states from the light coming from spontaneous parametric down-conversion. We also show that the Hopf links we measure are entangled, by demonstrating violations of the Bell inequality. We show that the entanglement between these isolated, spatial, topological vortex features extends over macroscopic and finite volumes.

J Romero, J Leach, B Jack, M R Dennis, S Franke-Arnold, S M Barnett, and M J Padgett, Phys Rev Lett 106, 10, 100407 (2011)

4.1 Phase singularities in the electromagnetic field

Phase singularities are generic features of complex scalar waves. In the case of electromagnetic fields, these are points where the light intensity is zero, the phase is undefined, and around which the phase changes by an integer multiple of 2π [175]. This is exactly what we find at the centre of Laguerre-Gaussian (LG) beams, around which the phase changes from 0 to 2π, ℓ times, depending on the orbital angular momentum (OAM) of the beam. The associated Poynting vector has an azimuthal component making it rotate around the centre, implying that there is a net flow of energy and momentum around the singularity, thus the term optical vortex. LG beams have an optical vortex line running through the optical axis and carry OAM at the same time (the OAM can be imagined as a flow of momentum around the optic axis). However, it is wrong to conclude that all OAM-carrying beams have optical vortex lines. OAM, as a property, relates only to the fact that the Poynting vector has an azimuthal component. Light can have azimuthal phase gradients without having optical vortex structures. The converse statement, that light beams associated with optical vortices have nonzero OAM however, is always true.

Optical vortices are not exclusively found in LG beams. Vortex lines occur whenever three or more plane waves interfere destructively, such as in optical speckle [176]. Light from a coherent laser scattered by a rough surface or propagating through inhomogeneous medium can form optical speckle patterns (fig. 4.1). The vortices occur as the dark points in between the bright

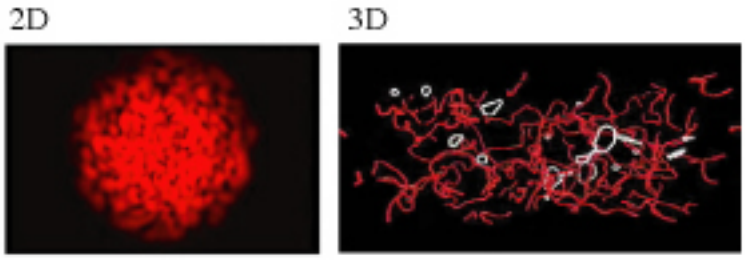

Figure 4.1: In two dimensions, an optical speckle pattern has vortices which are seen as dark points embedded between the bright speckles. In three dimensions, the vortices trace lines (red). Some of the vortices form loops (white), and some of the loops are linked. (speckle pattern from http://spie.org, 3D picture from O'Holleran [10])

speckles. They are the points of intersection of the vortex lines with the viewing plane. In three dimensions (3D), these vortex lines form a fractal tangle, percolating through space [177], exhibiting interesting topological structures such as closed loops which are occasionally linked together (fig. 4.1) [10]. Light produced by spontaneous parametric down-conversion (SPDC) is spatially incoherent and can also be considered as an example of optical speckle [178], making it a good candidate in which to observe topological vortex features.

4.2 Topological vortex structures and superpositions of OAM

Vortices forming interesting topologies, such as knots and links, can be deliberately created from a suitable combination of spatial modes. As Berry

and Dennis have shown, solutions to the Helmholtz equation can contain optical vortices which are knotted or linked [175, 179]. The LG beams, already having an optical vortex line along the optic axis, are naturally an attractive candidate for constructing such modes. Superpositions of LG beams with suitable amplitudes and relative phases result in optical vortices which form knots or links. For example, a mode consisting of a pair of linked optical vortex loops (fig. 4.2), a Hopf link, can be created by the superposition,

$$\Psi_{\text{Hopf link}} = 0.264LG_0^0 - 0.628LG_1^0 + 0.426LG_2^0 - 0.596e^{i2\theta}LG_0^2. \qquad (4.1)$$

where LG_p^ℓ are LG beams of azimuthal index ℓ and radial index p defined in (1.4), and θ defines the orientation of the Hopf link in the $x-y$ plane. The generation of these modes rely on being able to design optical elements which impart the desired vortex structure.

Experimentally, these modes are generated by bouncing a fundamental Gaussian mode off a diffractive optical element (hologram) suitably designed to introduce the vortex structures. To create the Hopf link described in (4.1), one must modulate both intensity and phase and so we employ the method we have discussed in section 2.2. Using this technique, different topological structures, including the Hopf link have been generated [167].

4.3 Measurement of Hopf links

In our entanglement experiment, we are not generating Hopf links of optical vortices. We are, instead, measuring Hopf links from the light that comes off a nonlinear crystal. Just as in our previous experiments, we use SPDC as the

source of correlated photon pairs. As we have seen in the previous chapters, correlations are present in the OAM of the signal and idler photons. We shall show that correlations are also manifested even by special superpositions of OAM modes whose phase singularity lines form a Hopf link.

4.3.1 Hologram design

Macroscopic vortex features like Hopf links can be synthesised by combining LG modes, including those possessing no OAM. We require a hologram encoded with the state described in 4.1), which entails modulation of both amplitude and phase. Although specified only in two dimensions, holograms determine the propagation of the whole optical field behind them. Previously, holograms have transformed the Gaussian output of a laser or single mode fibre into a field with phase singularities that form Hopf links [167]. In modal superpositions of this kind, the linked vortex loops intertwine within regions of very low optical intensity. The practical generation and observation of these topological features relies on the numerical optimisation of the complex mode coefficients to separate the vortex loops by regions of higher intensity [167]. Once the optimum coefficients of the modal components in the superposition are determined, it is a simple matter to implement them in spatial light modulators (SLMs) wherein we have control of both intensity and phase. Fig. 4.2.a shows how the hologram is calculated from knowledge of the phase and intensity structure of the Hopf link. Following section 2.2, the phase of the hologram,Φ_{holo}, is given by,

$$\Phi_{\text{holo}}(x,y) = \left[\Phi_{\text{link}}(x,y) + \Phi_{\text{grating}}(x,y)\right]_{\text{mod}2\pi} \times \text{D}(A_{\text{link}}(x,y)). \qquad (4.2)$$

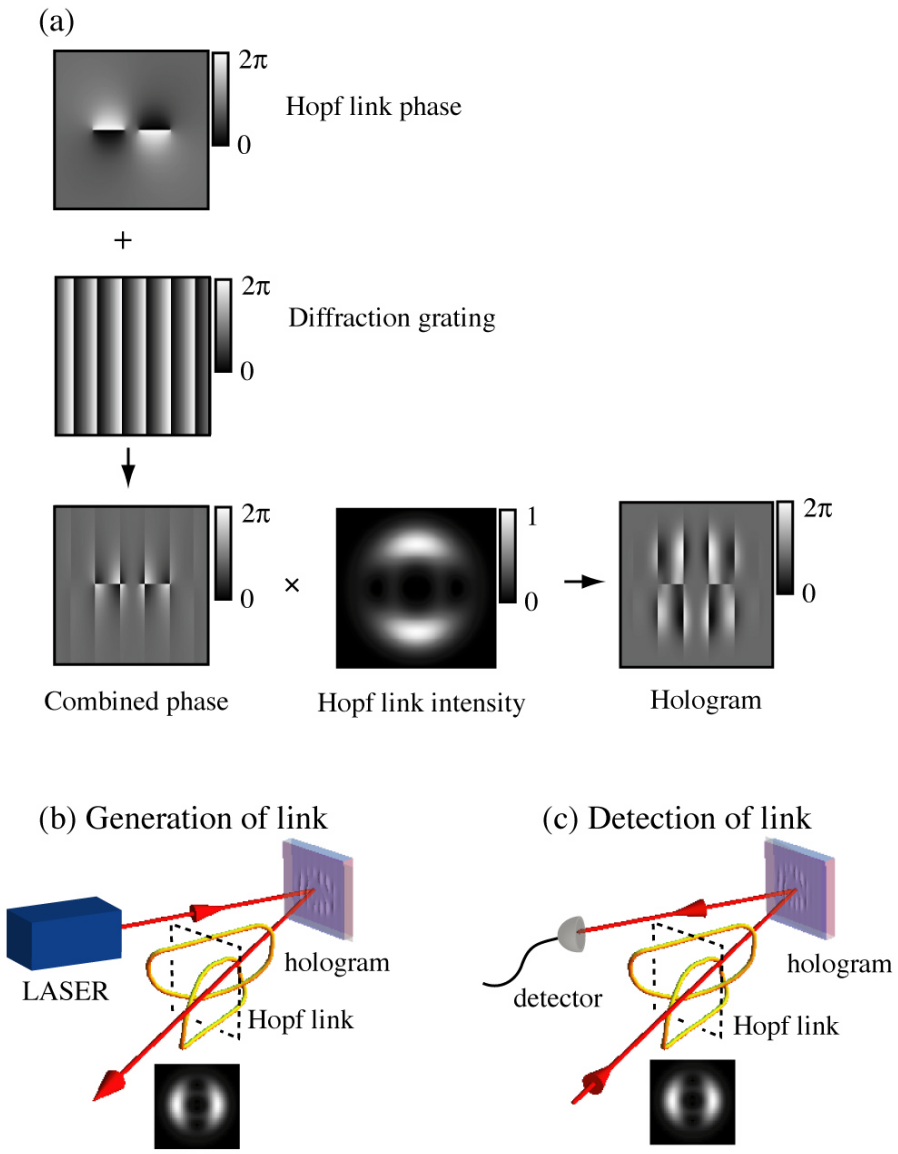

Figure 4.2: The hologram consists of the product of the Hopf link phase and the diffraction grating, modulated by the intensity of the link. The intensity translates to a correction in the depth of the phase blazing to change the diffraction efficiency (a). A hologram can define the structure of the field upon propagation. A hologram can be used to generate a Hopf link (b). A hologram can also be used in reverse to measure a Hopf link. The insets are intensity cross sections and show the vortex positions of the field on the plane represented by the dotted line (c).

where $\Phi_{\text{link}}(x, y)$ and $A_{\text{link}}(x, y)$ refer to the phase and amplitude cross sections of the link. $\Phi_{\text{grating}}(x, y)$ is the phase of the diffraction grating used to direct the light to the first order, and D is the distortion function mapping the grayscale to amplitude (sec. 2.2).

The same hologram that transforms a Gaussian mode into the Hopf link (fig. 4.2.b) can be used in reverse as a measurement hologram to detect the 3D feature (fig.4.2.c). In our case, this transforms a Hopf link back to the fundamental Gaussian mode which can then, and only then, be coupled into a single mode fibre and photon detector. A single photon detection after the hologram constitutes the single photon measurement of the 3D topological state, i.e. we can infer that the photon is in the topological state before the hologram.

4.3.2 Experiment setup and back-projection

We employ the experimental configuration shown in fig. 4.3.a. Our down-converted photons are produced by a 3 mm long type-I $\beta-$barium borate (BBO) crystal pumped by a quasi-cw, mode-locked UV pump beam at 355 nm. The crystal is oriented in a collinear geometry with the down-converted 710 nm signal and idler photons, both incident on the same beamsplitter. The exit face of the crystal is imaged to separate spatial light modulators (SLM). The SLMs are used to display the measurement holograms (fig. 4.2.a) which specify the links we aim to detect. These SLMs are reimaged to the input facets of single-mode fibres which are coupled to avalanche photodiodes (APD) for single photon detection. The output of the detectors are connected to a coincidence counting circuit with a timing window of 10

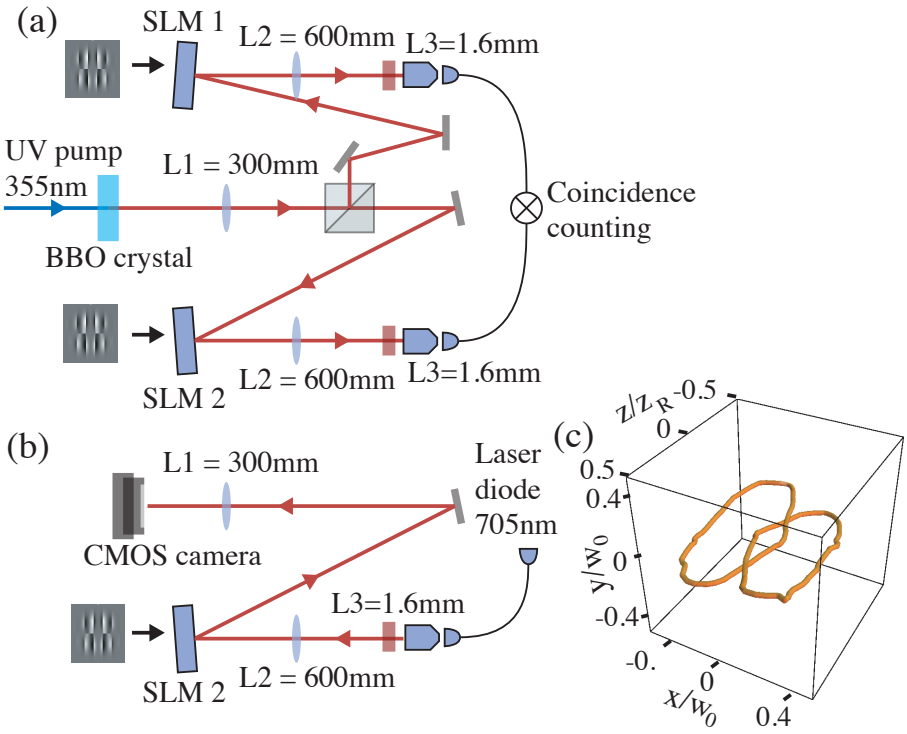

Figure 4.3: The topological states are measured by encoding holograms displayed on separate spatial light modulators (SLMs) (a). Using one of the arms in the same setup, we back-project through the measurement hologram, letting the first-order interfere with the zero-order beam in order to recover the phase information and verify the topology of the field (b) . The recovered topology is a Hopf link, x, y, z refer to shifts in the x−, y−and z− directions respectively. Dimensions have been normalised by the beam waist w_0 and Rayleigh range z_R (c). [11]

ns. The coincidence count rate from the two detectors is recorded as the holograms displayed on the SLMs are updated.

How do we guarantee that we are measuring fields with this special topology in single photons? As with any single-photon detection made via single-mode fibres and APDs, we are essentially destroying the photon by detecting it. This is the case even when we are measuring polarisation. We can only infer what the state of the photon was before it encountered the measuring device. For example, we know that only photons of a horizontal polarisation can pass through a horizontal polariser, hence when a detector after this polariser clicks, it was because there was a horizontal photon which passed through the polariser. We can confidently infer that this is the case because if we replace the detector with a laser, the light that comes after the horizontal polariser is a horizontally polarised photon. This "back-propagation" picture (consistent with retrodictive quantum mechanics [104]) shown in fig. 4.2.b is often unsaid, but this is what guarantees that we are inferring the correct spatial mode in the photons that we measure. It is conceptually no more complicated than measurements of OAM done with forked diffraction gratings, although we have a richer spatial mode with a topology that exists in 3D. We therefore confirmed that our hologram indeed generates a Hopf link by replacing one of the detectors with a laser diode, sending light back to the SLM and then recovering the phase and intensity of the diffracted light field in the plane of the crystal (fig. 4.3.b)[167]. We programmed the SLM to introduce axial displacements with respect to the plane of the crystal allowing us to tomographically reconstruct the phase in each plane and find the vortices to form the link structure as shown in fig. 4.3.c. Having recov-

ered a Hopf link in this "back-projection" experiment, we can confidently say that we are indeed measuring Hopf links. We remark that because this is a 3D structure, we need multiple-plane measurements which can not be performed in one shot on a single photon. Simply put, each measurement plane is a projection of one photon and we just make the assumption that all these photons are identical.

4.4 Entanglement of optical vortex links

Having described the key elements in our experiment, we now quantify quantum correlations that exist between these spatially separated Hopf links. We show that these links of vortex loops, embedded within optical fields produced by SPDC, are entangled.

4.4.1 Bloch sphere analogy

The modal superposition to produce the vortex Hopf link is given by

$$\begin{aligned} |\Psi_{\text{Hopf link}}\rangle &= 0.264\,|0,0\rangle - 0.628\,|0,1\rangle \\ &+ 0.426\,|0,2\rangle - 0.596e^{i2\theta}\,|2,0\rangle\,. \end{aligned} \tag{4.3}$$

where $|\ell, p\rangle$ denote the LG mode with p radial nodes and azimuthal index ℓ, and θ defines the orientation of the Hopf link in the x-y plane. Note that apart from a notation change (LG_p^ℓ is now written as $|\ell, p\rangle$), this equation is the same as (4.1). We use a pump beam of zero OAM in the state $|0,0\rangle$. OAM is generally conserved in collinear SPDC [126], and so we can write the

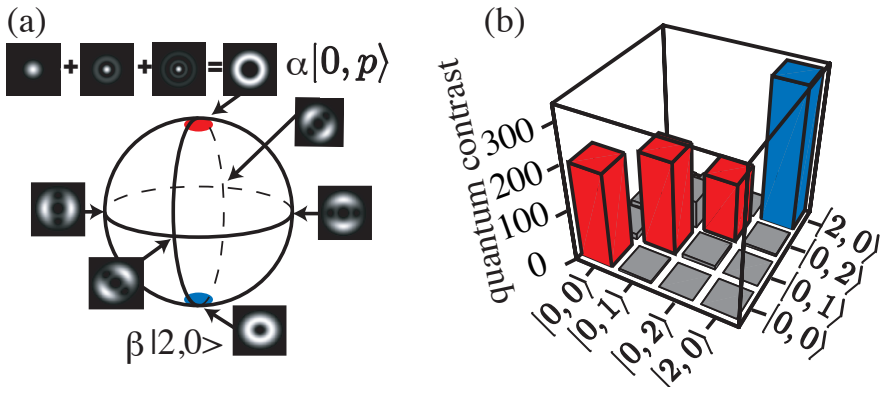

Figure 4.4: A Bloch sphere for the Hopf links has the state $\alpha\,|0,p\rangle$ (with constant phase and a small nonzero on-axis intensity) and $\beta\,|2,0\rangle$ (or $\beta\,|-2,0\rangle$) at the poles. The equatorial states correspond to the Hopf links (a). We examine the constituent modes of the link (b). Red bars show the correlation between the $\ell = 0$ states that make up $|0,p\rangle$ (North pole) and the blue bar correspond to the correlation between the $\ell = 2$ and $\ell = -2$ states (South pole). [11]

entangled SPDC state LG basis as,

$$|\Psi_{\text{SPDC}}\rangle = \sum_{p_s=0}^{\infty}\sum_{p_i=0}^{\infty}\sum_{\ell=-\infty}^{\infty} c_{-\ell,p_i}^{\ell,p_s}\,|\ell,p_s\rangle\,|-\ell,p_i\rangle \tag{4.4}$$

where $\left|c_{-\ell,p_i}^{\ell,p_s}\right|^2$ is dependent on the down-conversion process and is the probability of generating a photon pair in the $|\ell,p_s\rangle$ and $|-\ell,p_i\rangle$ states [88, 95, 118]. The state (4.4) has a range of different modes including the modes which comprise the superposition that could form the link (4.3).

We can separate the superposition (4.3) into two components consisting of modes with zero and nonzero OAM ($\ell = 0$ and $\ell = 2$ respectively), if we define the state $|0,p\rangle = 0.329\,|0,0\rangle - 0.782\,|0,1\rangle + 0.530\,|0,2\rangle$, which we get

by normalizing the first three terms of (4.3). We can then write the Hopf link state as

$$|\Psi_{\text{Hopf link}}\rangle = \alpha\,|0,p\rangle - \beta e^{i2\theta}\,|2,0\rangle\,, \tag{4.5}$$

where $\alpha = 0.803$ and $\beta = 0.596$. This allows us to define our measurement states in a two-dimensional (2D) subspace. The advantage of a 2D subspace is that it lends itself to traditional tests of entanglement such as the Bell inequality [68].

At the heart of entanglement are the correlations exhibited in the bases corresponding to incompatible observables. In a 2D state space, the concept of incompatible observables is best illustrated by a reference to a Bloch sphere where for example a rotation of linear polarisation is equivalent to a change in phase between the constituent circular polarisations. We have already used this reference to a Bloch sphere in the previous chapter (section 3.3.3) for our Bell and Leggett inequality violations by measuring OAM superpositions. We can cast the measurement of Hopf links similarly, in that we can have an unconventional Bloch sphere based on the superposition (4.3). The North pole of this Bloch sphere correspond to the weighted superposition $\alpha\,|0,p\rangle$ and the South pole corresponds to $\beta\,|2,0\rangle$. The equatorial states of this Bloch sphere are then the Hopf links oriented at different angles, θ (fig. 4.4.a).

To show entanglement between the Hopf links requires demonstrating that the strength of nonlocal correlations depend not only on the magnitude of the modes (the poles of the sphere) but also on their relative phases. We test this phase dependence by changing the relative angular orientations of the topological features measured in the signal and idler beams. If the observed correlations were simply and solely due to classical conservation,

then the strength of the correlations would show no phase dependence.

We also show the confinement of the Hopf link to a finite volume and the dependence of the entanglement on relative spatial position. To one of the holograms, we introduced lateral and axial shifts, the latter giving a Gouy phase between the modes [180]. Rather than moving any of the optical components we apply these shifts directly by setting the phase of the modal superpositions for the hologram design.

4.4.2 Bell inequality for optical vortex links and entanglement of volumes

In the image plane of the crystal, the signal and idler fields are complex conjugates of each other. If the holograms are encoded with states that are themselves complex conjugates of each other, the correlation between signal and idler beams should be high. The LG basis that we use to describe our topological features is an orthonormal, complete set and consequently the correlation between any two modes of differing indices should, ideally, be zero.

Before examining the correlation between the Hopf links themselves we examine the measured correlations between the four LG modes that form the Hopf link (fig.4.4.b). We calculate the ratio of the measured coincident rate, C, to that anticipated from accidental coincidences. We call this ratio the quantum contrast, QC, given by $QC = C/(S \times I \times \Delta t)$, where S and I are signal and idler count rates respectively, and Δt is the timing resolution of our coincidence counting electronics [72]. As anticipated, the correlation between any mode and its complex conjugate is high, while its correlation

with all other modes is low (fig. 4.4.b). We note, however, that some nominally orthogonal modes have residual correlations, which arise from the finite apertures of our system. This imperfection potentially reduces the degree of the entanglement, but as we show below, the entanglement we observe is still sufficient to violate a Bell inequality.

With the SLMs displaying holograms to measure the Hopf link and its complex conjugate, we measure the coincident count rate as a function of their angular orientations θ_s and θ_i. The sinusoidal nature of the coincidence count rates are reminiscent of the coincidence curves used to show a violation of the Bell inequality in the case of polarisation-entangled photons. The fact that our state can be written in terms of two orthogonal sets of modes means we can perform a similar analysis for our Hopf links [68]. We use the Clauser-Horne-Shimony-Holt(CHSH) inequality [181], which gives the Bell parameter S, and is violated when $|S| > 2$ (sections 3.3.2, 3.3.4). The extent to which this inequality can be violated is an indication of the degree of entanglement of a quantum system, with S taking on a value of $2\sqrt{2}$ for maximally entangled states.

Because the Hopf link contains a component with $\ell = 0$, the Hopf link and its complex conjugate are not completely orthogonal, and hence the coincidence rate should not fall to exactly zero [92]. For a theoretical prediction, we can use (2.11). We obtain lower minima in our coincidence curves, and this is a consequence of the interference arising from modes that are ideally orthogonal (i.e. the off-diagonal modes in fig.4.4.b), but experimentally gives residual coincidence counts. Fig.4.5.a shows a sample set of coincidence curves used to calculate S from four different orientations of the signal

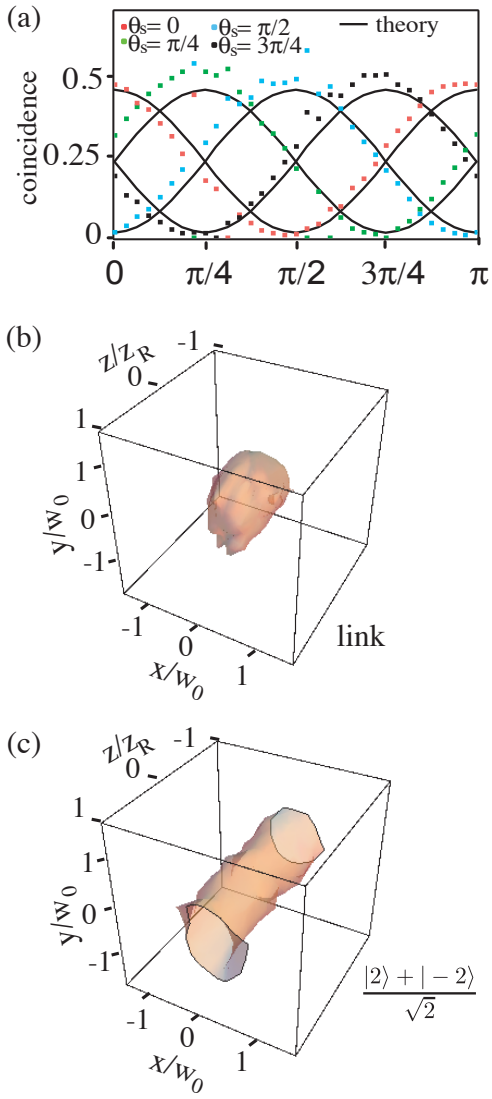

Figure 4.5: Coincidence curves show a phase dependence on angular orientations θ_s and θ_i from which we obtain $S = 2.72$ when signal and idler holograms are both on the $z = 0$ plane. (a) The surface for which $S = 2$ surface for a Hopf link (b) and for a simple superposition of OAM states (c). x, y, z refer to shifts in the x−, y−and z− directions respectively. Dimensions have been normalised by the beam waist w_0 and Rayleigh range z_R.

hologram as the orientation of the idler hologram is varied from 0 to π (corresponding to a phase change between the $\alpha\,|0,p\rangle$ and $\beta\,|2,0\rangle$ of 0 to $2\theta_i = 2\pi$). The near sinusoidal shape is an indication that we largely remain in a 2D state space. Following [122], wherein the dimensionality is taken as the inverse of the area under the peak-normalised coincidence curve, we obtain a Shannon dimensionality of 1.92. We measure S to be 2.72 ± 0.01 when the signal and idler holograms are laterally and axially aligned, greater than the classical limit of 2, thereby demonstrating that the Hopf links we measure in the down-converted fields are indeed entangled.

The unique aspect of these entangled states is that the topological feature is spatially localised in 3D. We show this by measuring S as a function of both lateral and axial displacements of the measured links and compare this volumetric scan to that obtained for the simple superposition of $|\pm\ell\rangle$ OAM states used to show the entanglement of OAM (fig. 4.5.b-c). In this latter case we use a superposition of $\ell = \pm 2$, measuring the count rate and obtaining S as a function of lateral and axial displacement. As might be expected, for pure OAM entanglement we see that the value of S falls for lateral displacement, yet the structural stability of the mode means that S does not fall with axial displacement. By contrast we see that the volume over which the Hopf link violates the CHSH inequality ($S > 2$) is bounded in both the lateral and axial directions to a size similar to that of the experimentally recovered Hopf link, fig. 4.3.c.

The SLMs that we use have a diffraction efficiency of about 60%, we are not free of the detection loophole. We are using off-axis holograms, meaning that any phase noise in the SLM will affect only the diffraction efficiency,

not the phase of the measured state, which is instead set by the spatial form of the hologram. We emphasise that the topology of the Hopf link is recreated in the "back-projection" experiment, inferring that these are the states we measure. In any event, the fact that we violate the Bell inequality is an unambiguous demonstration of quantum entanglement and demonstrates that we are not significantly constrained by the limitations of our SLMs.

4.5 Conclusion and Outlook

From a fundamemental standpoint, our results are interesting because by measuring a specific topology of vortices on one photon, we are essentially "steering" the position of the vortices in the other photon. Whereas earlier work in quantum entanglement has concentrated on two separated point properties of the field (e.g. polarisation) or two field cross-sections (e.g. OAM), our present work shows a signature of entanglement between two separated and finite volumes. Specifically, our measurements relate to topological features of the scalar electromagnetic field. Similar wave descriptions are equally applicable to various physical situations involving cold atoms, superfluids and other condensed matter systems. The existence of vortex lines and related topological features in these systems is an area of intense theoretical and experimental investigation [182, 183, 184]. We conjecture that the quantum entanglement of topological features of vortex lines may extend to cover these other system types. The transfer of the topological vortex states from light to BEC [183, 185] may be a route to the preparation of macroscopically entangled topological states.

As a further point, since topological states are usually robust to perturbation [186], they may offer a route to increasing the stability of the entangled state. Indeed stability of topology has, in two-dimensional physics, led to the field of topological quantum computation [187]. The degree to which three-dimensional vortex topological features are stable or not depends upon the details of the physical system in which they occur. For example, if vortex lines are subject to a repulsive force between them, as can be the case in a nonlinear media [188], this acts to stabilise their topology. Unfortunately for light beams in free-space this is not the case and therefore topology is unlikely to mitigate, for example, the effect of atmospheric turbulence. However, other physical systems may not be limited in this way.

Chapter 5

Conclusion

Entanglement is manifested in a variety of quantum systems. For photons, entanglement is most commonly studied in relation to photon polarisation, wherein the photon is a qubit which can take on any of two possible, orthogonal values. Outside this two-state system, entanglement can be explored in higher dimensions by exploiting various other degrees of freedom, such as time-bin, energy, position and linear momentum, among others. In this thesis, I have focused on the entanglement of the orbital angular momentum (OAM) of photons and its conjugate variable, angular position. OAM is discrete and theoretically unbounded, while angular position is continuous and periodic. These variables are Fourier-related and together they make up basis sets suitable for investigating higher-dimensional entanglement.

We first discussed the process which generates the entangled photon pairs- spontaneous parametric down-conversion (SPDC). We investigated the two important factors that determine OAM and angular position correlations, namely, phase-matching and the shape of the pump. We have shown that

minute adjustments to the phase-matching conditions in SPDC can result to an increase in the range of entangled OAM modes generated. We have shown an experimental system capable of generating and detecting 30-dimensional OAM entanglement. We have also demonstrated the influence of the pump shape, by employing a phase-flipped mode (akin to a first-order Hermite-Gaussian beam) to pump the crystal for SPDC. We have shown OAM correlations consistent with OAM conservation, and angular position correlation consistent with the Fourier relationship between OAM and angle.

The Fourier relationship between OAM and angular position is reminiscent of a similar relationship between position and linear momentum- the original variables in which Einstein, Podolsky and Rosen (EPR) formulated their famous paradox. We have demonstrated that the same EPR paradox holds for OAM and angle. Similarly, we are led to ask: is quantum mechanics a complete theory? Is our notion of locality mistaken? In response to the first question, local hidden variable theories (LHVT) have been proposed as an alternative to explain the correlations that we measure. We have exploited the analogy between a Poincaré sphere and an OAM Bloch sphere to implement various tests of quantum mechanics. Similar to the results obtained for polarisation, our experiments with OAM point to the inadequacy of LHVTs to account for OAM correlations. We have shown violations of Bell-type inequalities for various two-dimensional subspaces of OAM. On a more intuitive level, we have also shown the conflict between quantum mechanics and local realism via the paradoxical situation envisaged by Hardy. We have utilised the naturally non-maximally OAM-entangled state generated by SPDC to achieve the varying degrees of entanglement necessary for demonstrating the

Hardy paradox. Having discounted LHVTs, we also examined a general class of nonlocal hidden variable theories (NHVTs) as proposed by Leggett. We have recreated the experiments originally done on photon polarisation and obtained the same conclusion, that even NHVTs are not enough to account for correlations. This leaves us with quantum mechanics as the best description for our experiments.

In the last chapter, we have also considered a rather special spatial mode consisting of isolated, linked loops of optical vortices called Hopf links. The Hopf links can be expressed in terms of a specific superposition of OAM modes. We have shown that these modes can be measured from the light coming from SPDC, and moreover, these modes are entangled. With the aid of an analogy with the Poincaré sphere, we have demonstrated violations of a Bell-type inequality as a function of spatial position. We have shown that when measuring Hopf links, the violations are confined within a three-dimensional volume corresponding to the extent of the Hopf link. In contrast to polarisation, which can be considered as a property of a point, or to OAM, which can be considered as a property of a cross-section, our Hopf links are features in a finite, isolated volume. This points to interesting possibilities for other systems which are amenable to a scalar wave description such as cold atoms, superfluids and other condensed matter systems.

When stripped of all details, there are two messages I hope this thesis has conveyed:

(1) Quantum mechanics explored with OAM is just as peculiar as quantum mechanics explored with anything else.

Spatial light modulators, which have played an important role in all our

demonstrations here, makes the OAM state space a truly accessible test bed for quantum mechanics.

(2) Having established (1), We see that OAM is a degree of freedom waiting to fulfil its potential.

Many of the results we have presented here are not really surprising, most physicists will agree that quantum mechanics is true anyway. I would rather consider our results as groundwork for exciting work in the future. Optical implementations of quantum information abound, and OAM is but one research area. Given that OAM-entangled states are naturally generated in down-conversion, and the measurement states can be implemented conveniently, I believe that OAM is one of the best candidates for exploring high-dimensional entanglement. Why we want to do that is a good question, and there are a range of answers. It is my hope that OAM can reveal deeper features of quantum mechanics. From a practical standpoint, I think that there has been much development in terms of generating and sorting OAM states, possible quantum gates, and interaction of materials with OAM states. The concept of secure, high-dimensional quantum communication is an attractive catalyst for all these, but I hope research will progress further. I am sure there is much more to be had from OAM, if only we can imagine more!

Appendix:

Coincidence probability for measuring angular position with finite angular slits

The probability density for having entangled photons at angles ϕ_i and ϕ_s is a function only of the difference,

$$P(\phi_s, \phi_i) = \frac{1}{2\pi} P(\phi_s - \phi_i). \tag{5.1}$$

If angle correlations are measured with masks M_s and M_i, the probability of getting a coincidence, P_{coin}, as function of the orientations ϕ_i and ϕ_s is

$$P_{coin}(\phi_s, \phi_i) = \frac{1}{2\pi} \int M_s(\phi_s) M_i(\phi_i) P(\phi_s - \phi_i) d\phi_s d\phi_i. \tag{5.2}$$

The angular masks are characterised by a width Δ and the two masks have a relative orientation of $\Delta\theta$. This means we have

$$M_s = \begin{cases} 1 & -\Delta/2 < \phi_s < \Delta/2 \\ 0 & \text{otherwise} \end{cases}$$

$$M_i = \begin{cases} 1 & -\Delta/2 + \Delta\theta < \phi_i < \Delta/2 + \Delta\theta \\ 0 & \text{otherwise} \end{cases}$$

We substitute these to (5.2) and get

$$P_{coin}(\phi_s, \phi_i) = \frac{1}{2\pi} \int_{-\Delta/2}^{\Delta/2} d\phi_s \int_{-\Delta/2+\Delta\theta}^{\Delta/2+\Delta\theta} d\phi_i P(\phi_s - \phi_i). \tag{5.3}$$

which is an integration over the area of a square defined by the vertices $(\phi_i, \phi_s) = (-\Delta/2 + \Delta\theta, -\Delta/2), (-\Delta/2 + \Delta\theta, \Delta/2), (\Delta/2 + \Delta\theta, \Delta/2), (\Delta/2 + \Delta\theta, -\Delta/2)$

We change variables: $\bar{\phi} = \frac{1}{2}(\phi_s + \phi_i)$ and $x = \phi_s - \phi_i$ so $d\phi_i d\phi_s = d\bar{\phi}dx$. This changes the area of integration into a parallelipiped of vertices $(x, \bar{\phi}) = (-\Delta\theta, -\Delta/2 + \Delta\theta/2), (-\Delta - \Delta\theta, \Delta\theta/2), (-\Delta\theta, \Delta/2 + \Delta\theta/2), (\Delta - \Delta\theta, \Delta\theta/2)$

We break up the integral along x, and use the equations for the boundaries of the parallelipiped,

$$\begin{aligned} P_{coin}(\phi_s, \phi_i) &= \frac{1}{2\pi} \int_{-\Delta-\Delta\theta}^{-\Delta\theta} dx \int_{-x/2-\Delta/2}^{x/2+\Delta/2+\Delta\theta} d\bar{\phi} P(x) \\ &+ \frac{1}{2\pi} \int_{-\Delta\theta}^{\Delta-\Delta\theta} dx \int_{x/2-\Delta/2+\Delta\theta}^{-x/2+\Delta/2} d\bar{\phi} P(x) \\ &= \frac{1}{2\pi} \int_{-\Delta-\Delta\theta}^{-\Delta\theta} dx (x + \Delta + \Delta\theta) P(x) \\ &+ \frac{1}{2\pi} \int_{-\Delta\theta}^{\Delta-\Delta\theta} dx (-x + \Delta - \Delta\theta) P(x) \end{aligned} \tag{5.4}$$

In the first integral, $P(x)$ is effectively multiplied by a ramp which goes from 0 to Δ and in the second integral, $P(x)$ is effectively multiplied by a ramp which goes from Δ to 0. If we define a function $T(x)$ such that,

$$T(x) = \begin{cases} 0 & x < -\Delta - \Delta\theta \\ x + \Delta + \Delta\theta & -\Delta - \Delta\theta < x < -\Delta\theta \\ -x + \Delta - \Delta\theta & -\Delta\theta < x < \Delta - \Delta\theta \\ 0 & \Delta - \Delta\theta < x \end{cases}$$

we can write P_{coin} as the integral of a product,

$$P_{coin}(x;\Delta\theta) = \frac{1}{2\pi}\int dx T(x)P(x) \tag{5.5}$$

We can take $P(x)$ from the contribution of the OAM components weighted by c_ℓ.

$$P(x) = \frac{1}{2\pi}\left|\sum_\ell c_\ell e^{i\ell x}\right|^2 \tag{5.6}$$

so we have in the end the coincidence as a function of the relative orientation $\Delta\theta$

$$J(\Delta\theta) = \frac{1}{2\pi}\int dx \quad T(x)\left|\sum_\ell c_\ell e^{i\ell x}\right|^2 \tag{5.7}$$

Bibliography

[1] J. Leach, S. Keen, M. J. Padgett, C. Saunter, and G. D. Love. Direct measurement of the skew angle of the poynting vector in a helically phased beam. *Opt. Express*, 14(25):11919–11924, 2006.

[2] D. Andrews and M. Babiker. *The angular momentum of light*. Cambridge University Press, 2012.

[3] J. Romero, D. Giovannini, F. M. Miatto, S. M. Barnett, and M. J. Padgett. Increasing the dimension in high-dimensional two-photon orbital angular momentum entanglement. *Phys. Rev. A*, 86:012334, 2012.

[4] J. Romero, D. Giovannini, M. G McLaren, E. J Galvez, A. Forbes, and M. J Padgett. Orbital angular momentum correlations with a phase-flipped gaussian mode pump beam. *J. of Opt.*, 14(8):085401, 2012.

[5] J. Leach, B. Jack, J. Romero, A. Jha, A. Yao, S. Franke-Arnold, D. Ireland, R. Boyd, S. Barnett, and M. Padgett. Quantum correlations in optical angle-orbital angular momentum variables. *Science*, 329:662, 2010.

[6] A. Aspect, J. Dalibard, and G. Roger. Experimental test of Bell's inequalities using time-varying analyzers. *Phys. Rev. Lett.*, 49:1804–1807, 1982.

[7] J. Leach, B. Jack, J. Romero, M. Ritsch-Marte, R. W. Boyd, A. K. Jha, S. M. Barnett, S. Franke-Arnold, and M. J. Padgett. Violation of a Bell inequality in two-dimensional orbital angular momentum state-spaces. *Opt. Express*, 10:8287–8293, 2009.

[8] B. Jack, A. M. Yao, J. Leach, J. Romero, S. Franke-Arnold, D. G. Ireland, S. M. Barnett, and M. J. Padgett. Entanglement of arbitrary superpositions of modes within two-dimensional orbital angular momentum state spaces. *Phys. Rev. A*, 81(4):43844, 2010.

[9] J. Romero, J. Leach, B. Jack, S. M. Barnett, M. J. Padgett, and S. Franke-Arnold. Violation of Leggett inequalities in orbital angular momentum subspaces. *New J. Phys.*, 12:123007, 2010.

[10] K. O'Holleran, M. R. Dennis, and M. J. Padgett. Topology of light's darkness. *Phys. Rev. Lett.*, 102:143902, 2009.

[11] J. Romero, J. Leach, B. Jack, M. R. Dennis, S. Franke-Arnold, S. M. Barnett, and M. J. Padgett. Entangled optical vortex links. *Phys. Rev. Lett.*, 106(10):100407, 2011.

[12] M. Planck. *The theory of heat radiation.* Amer. Inst. of Physics, 1906.

[13] A. Einstein. On a heuristic viewpoint concerning the production and transformation of light. *Annalen der Physik*, 17:132–148, 1905.

[14] L. de Broglie. A tentative theory of light quanta. *Phil. Mag*, 47:446–458, 1924.

[15] E. Schrödinger. An undulatory theory of the mechanics of atoms and molecules. *Phys. Rev.*, 28(6):1049–1070, 1926.

[16] M. Born and P. Jordan. Zur Quantenmechanik. *Z. Phys A-Hadron Nucl*, 34(1):858–888, 1925.

[17] P. A. M. Dirac. The quantum theory of the electron. *Proc. R. Soc. Lond. A*, 117(778):610–624, 1928.

[18] A. Einstein, B. Podolsky, and N. Rosen. Can quantum-mechanical description of reality ever be considered complete? *Phys. Rev.*, 47:777–780, 1935.

[19] M. Genovese. Research on hidden variable theories: A review of recent progresses. *Phys. Rep.*, 413(6):319–396, 2005.

[20] R. Horodecki, P. Horodecki, M. Horodecki, and K. Horodecki. Quantum entanglement. *Rev. Mod. Phys*, 81(2):865–942, 2009.

[21] E. Schrödinger. Discussion of probability relations between separated systems. In *Mathematical Proceedings of the Cambridge Philosophical Society*, volume 31, pages 555–563. Cambridge University Press, 1935.

[22] E. Schrödinger and Trimmer J. D(translator). The present situation in quantum mechanics. *P. Am. Philos. Soc.*, 124:323–38, 1980.

[23] S. Barnett. *Quantum information*, volume 16. Oxford University Press, 2009.

[24] N. Brunner, N. Gisin, and V. Scarani. Entanglement and non-locality are different resources. *New J. of Phys.*, 7:88, 2005.

[25] A. Peres. *Quantum theory: concepts and methods*. Springer, 1993.

[26] M. Born. On the quantum mechanics of collisions. In *Quantum theory and measurement*. Princeton University Press, 1983.

[27] L. Mandel and E. Wolf. *Optical coherence and quantum optics*. Cambridge University Press, 1995.

[28] R. Loudon. *The quantum theory of light*. Oxford University Press, 2000.

[29] W. E. Lamb. Anti-photon. *Appl. Phys. B*, 60(2):77–84, 1995.

[30] G. N. Lewis. The conservation of photons. *Nature*, 118:874–875, 1926.

[31] E. Hecht and A. Zajac. *Optics*. Addison Wesley, 2002.

[32] R. Ursin, F. Tiefenbacher, T. Schmitt-Manderbach, H. Weier, T. Scheidl, M. Lindenthal, B. Blauensteiner, T. Jennewein, J. Perdigues, P. Trojek, B. Ömer, M. Fürst, M. Meyenburg, J. Rarity, Z. Sodnik, C. Barbieri, H. Weinfurter, and A. Zeilinger. Entanglement-based quantum communication over 144 km. *Nat. Phys.*, 3(7):481–486, 2007.

[33] J. C. Howell, R. S. Bennink, S. J. Bentley, and R. W. Boyd. Realization of the Einstein-Podolsky-Rosen paradox using momentum-and position-entangled photons from spontaneous parametric down conversion. *Phys. Rev. Lett.*, 92(21):210403, 2004.

[34] I. Ali Khan and J. C. Howell. Experimental demonstration of high two-photon time-energy entanglement. *Phys. Rev. A*, 73:31801, 2006.

[35] J.H. Poynting. The wave motion of a revolving shaft, and a suggestion as to the angular momentum in a beam of circularly polarised light. *Proc. R. Soc. Lond. A*, 82(557):560–567, 1909.

[36] R. A. Beth. Mechanical detection and measurement of the angular momentum of light. *Phys. Rev.*, 50(2):115, 1936.

[37] C. G. Darwin. Notes on the theory of radiation. *Proc. R. Soc. Lond. A*, 136(829):36–52, 1932.

[38] M. E. Rose. *Multipole Fields*. John Wiley and Sons, Inc., 1955.

[39] L. Allen, M. W. Beijersbergen, R. J. C. Spreeuw, and J. P. Woerdman. Orbital angular momentum of light and the transformation of Laguerre-Gaussian laser modes. *Phys. Rev. A*, 45:8185–8189, 1992.

[40] L. Allen, S. M. Barnett, and M. J. Padgett. *Optical angular momentum*. Taylor & Francis, 2003.

[41] S. Franke-Arnold, L. Allen, and M. Padgett. Advances in optical angular momentum. *Laser & Photonics Reviews*, 2(4):299–313, 2008.

[42] S. J. Enk and G. Nienhuis. Spin and orbital angular momentum of photons. *Europhys. Lett.*, 25:497, 1994.

[43] D. Bohm. *Quantum theory*. Dover Publications, 1951.

[44] H.C. Ohanian. What is spin? *Am. J. Phys.*, 54:500, 1986.

[45] N. Gisin, G. Ribordy, W. Tittel, and H. Zbinden. Quantum cryptography. *Rev. Mod. Phys.*, 74(1):145–195, 2002.

[46] J. Arlt and K. Dholakia. Generation of high-order bessel beams by use of an axicon. *Optics Comm.*, 177(1-6):297–301, 2000.

[47] M. A. Bandres and J. C. Gutiérrez-Vega. Ince gaussian beams. *Optics Lett.*, 29(2):144–146, 2004.

[48] M. W. Beijersbergen, L. Allen, H. Van der Veen, and J. P. Woerdman. Astigmatic laser mode converters and transfer of orbital angular momentum. *Opt. Commun.*, 96(1-3):123–132, 1993.

[49] V. Bazhenov, M. V. Vasnetsov, and M. S. Soskin. Laser beams with screw dislocations in their wavefronts. *JETP Lett.*, 52:429–431, 1990.

[50] A. T. O'neil, I. MacVicar, L. Allen, and M. J. Padgett. Intrinsic and extrinsic nature of the orbital angular momentum of a light beam. *Phys. Rev. Lett.*, 88(5):53601, 2002.

[51] L. Allen, M. J. Padgett, and M. Babiker. I.V. The orbital angular momentum of light. *Progress in Optics*, 39:291–372, 1999.

[52] A. Aspect, P. Grangier, and G. Roger. Experimental tests of realistic local theories via Bell's theorem. *Phys. Rev. Lett.*, 47:460–463, 1981.

[53] A. Ekert and R. Jozsa. Quantum computation and shor's factoring algorithm. *Rev. Mod. Phys.*, 68(3):733, 1996.

[54] D. Collins, N. Gisin, N. Linden, S. Massar, and S. Popescu. Bell inequalities for arbitrarily high-dimensional systems. *Phys. Rev. Lett.*, 88(4):40404, 2002.

[55] A. Dada, J. Leach, G. Buller, M. J. Padgett, and E. Andersson. Experimental high-dimensional two-photon entanglement and violations of generalized Bell inequalities. *Nat. Phys.*, 7(677-680), 2011.

[56] M. Wieśniak, T. Paterek, and A. Zeilinger. Entanglement in mutually unbiased bases. *New J. of Phys.*, 13:053047, 2011.

[57] H. Bechmann-Pasquinucci and A. Peres. Quantum cryptography with 3-state systems. *Phys. Rev. Lett.*, 85(15):3313–3316, 2000.

[58] H. Bechmann-Pasquinucci and W. Tittel. Quantum cryptography using larger alphabets. *Phys. Rev. A*, 61(6):62308, 2000.

[59] L. Zhang, C. Silberhorn, and I. A. Walmsley. Secure quantum key distribution using continuous variables of single photons. *Phys. Rev. Lett.*, 100(11):110504, 2008.

[60] S. P. Walborn, D. S. Lemelle, M. P. Almeida, and P. H. Souto Ribeiro. Quantum key distribution with higher-order alphabets using spatially encoded qudits. *Phys. Rev. Lett.*, 96(9):90501, 2006.

[61] P. B. Dixon, G. A. Howland, Schneeloch J., and J. C. Howell. Quantum mutual information capacity for high-dimensional entangled states. *Phys. Rev. Lett*, 108:143603, 2012.

[62] M. Avenhaus, M. V. Chekhova, L. A. Krivitsky, G. Leuchs, and C. Silberhorn. Experimental verification of high spectral entanglement for pulsed waveguided spontaneous parametric down-conversion. *Phys. Rev. A*, 79(4):043836, 2009.

[63] H. De Riedmatten, I. Marcikic, H. Zbinden, and N. Gisin. Creating high dimensional entanglement using mode-locked lasers. *Quantum Inf. Comput.*, 2(6):425–433, 2002.

[64] S. Franke-Arnold, S. Barnett, M. Padgett, and L. Allen. Two-photon entanglement of orbital angular momentum states. *Phys. Rev. A*, 65:033823, 2002.

[65] A. Mair, A. Vaziri, G. Weihs, and A. Zeilinger. Entanglement of the orbital angular momentum states of photons. *Nature*, 412:313–316, 2001.

[66] J. S. Bell. On the problem of hidden variables in quantum mechanics. *Rev. Mod. Phys.*, 38(3):447–452, 1966.

[67] J.S. Bell. On the Einstein-Rosen-Podolsky paradox. *Physics*, 1:195–200, 1966.

[68] J. S. Bell. *Speakable and Unspeakable in Quantum Mechanics*. Cambridge University Press, 1987.

[69] L. Hardy. Nonlocality for two particles without inequalities for almost all entangled states. *Phys. Rev. Lett.*, 71(11):1665–1668, 1993.

[70] A. J. Leggett. Nonlocal hidden-variable theories and quantum mechanics: An incompatibility theorem. *Foundations of Physics*, 33(10):1469–1493, 2003.

[71] D. A. Kleinman. Theory of optical parametric noise. *Phys. Rev.*, 174(3):1027, 1968.

[72] D. Burnham and D. Weinberg. Observation of simultaneity in parametric production of optical photon pairs. *Phys. Rev. Lett.*, 25:84, 1970.

[73] S.J. Freedman and J. F. Clauser. Experimental test of local hidden-variable theories. *Phys. Rev. Lett.*, 28:938–941, 1972.

[74] E. Santos. Does quantum mechanics violate the Bell inequalities? *Phys. Rev. Lett.*, 66(11):1388, 1991.

[75] E. Santos. Critical analysis of the empirical tests of local hidden-variable theories. *Phys. Rev. A*, 46(7):3646, 1992.

[76] J. F. Clauser and M. A. Horne. Experimental consequences of objective local theories. *Phys. Rev. D*, 10(2):526, 1974.

[77] Y. Shih and C. Alley. New type of Einstein-Podolsky-Rosen Bohm experiment using pairs of light quanta produced by optical parametric down conversion. *Phys. Rev. Lett.*, 61:2921–2924, 1988.

[78] J. G. Rarity and P. R. Tapster. Experimental violation of Bells inequality based on phase and momentum. *Phys. Rev. Lett.*, 64(21):2495–2498, 1990.

[79] W. Tittel, J. Brendel, H. Zbinden, and N. Gisin. Violation of Bell inequalities by photons more than 10 km apart. *Phys. Rev. Lett.*, 81(17):3563–3566, 1998.

[80] S. P. Walborn, A. N. De Oliveira, R. S. Thebaldi, and C. H. Monken. Entanglement and conservation of orbital angular momentum in spontaneous parametric down-conversion. *Phys. Rev. A*, 69(2):23811, 2004.

[81] Z. Y. Ou and L. Mandel. Violation of Bell's inequality and classical probability in a two-photon correlation experiment. *Phys. Rev. Lett.*, 61(1):50–53, 1988.

[82] P. G. Kwiat, K. Mattle, H. Weinfurter, A. Zeilinger, A. V. Sergienko, and Y. Shih. New high-intensity source of polarization-entangled photon pairs. *Phys. Rev. Lett.*, 75(24):4337–4341, 1995.

[83] P. G. Kwiat, E. Waks, A. G. White, I. Appelbaum, and P. H. Eberhard. Ultrabright source of polarization-entangled photons. *Phys. Rev.A*, 60(2), 1999.

[84] B. Y. Zel'Dovich and D. N. Klyshko. Field statistics in parametric luminescence. *ZhETF Pis ma Redaktsiiu*, 9:69, 1969.

[85] C. K. Hong and L. Mandel. Theory of parametric frequency down conversion of light. *Phys. Rev. A*, 31(4):2409, 1985.

[86] C. H. Monken, P. H. Souto Ribeiro, and S. Pádua. Transfer of angular spectrum and image formation in spontaneous parametric down-conversion. *Phys. Rev. A*, 57(4):3123–3126, 1998.

[87] S. P. Walborn, C. H. Monken, S. Pádua, and P. H. Souto Ribeiro. Spatial correlations in parametric down-conversion. *Phys. Rep.*, 495(4-5):87–139, 2010.

[88] A. M. Yao. Spectral decomposition of entangled photons with an arbitrary pump. *New. J. Phys*, 13(5):053048, 2011.

[89] S. Feng and P. Kumar. Spatial symmetry and conservation of orbital angular momentum in spontaneous parametric down-conversion. *Phys. Rev. Lett.*, 101(16):163602, 2008.

[90] H. H. Arnaut and G. A. Barbosa. Orbital and intrinsic angular momentum of single photons and entangled pairs of photons generated by parametric down-conversion. *Phys. Rev. Lett.*, 85(2):286–289, 2000.

[91] F. M. Miatto, A.M. Yao, and S. M. Barnett. Full characterization of the quantum spiral bandwidth of entangled biphotons. *Phys. Rev. A*, 83(3):033816, 2011.

[92] S. M. Barnett and S. J. D. Phoenix. Bell's inequality and the Schmidt decomposition. *Phys. Lett. A*, 167(3):233–237, 1992.

[93] R. W. Boyd. *Nonlinear optics*. Academic Press, 2003.

[94] H. Vanherzeele and C. Chen. Widely tunable parametric generation in beta barium borate. *Appl. Opt.*, 27(13), 1988.

[95] C. K. Law and J. H. Eberly. Analysis and interpretation of high transverse entanglement in optical parametric down conversion. *Phys. Rev. Lett.*, 92(12):127903, 2004.

[96] F. M. Miatto, D. Giovannini, J. Romero, S. Franke-Arnold, S. M. Barnett, and M. J. Padgett. Bounds and optimisation of orbital angular momentum bandwidths within parametric down-conversion systems. *Eur. Phys. J. D*, 66:178, 2012.

[97] P. Kolenderski, W. Wasilewski, and K. Banaszek. Modeling and optimization of photon pair sources based on spontaneous parametric down-conversion. *Phys. Rev. A*, 80(1):013811, 2009.

[98] N. Boeuf, D. Branning, I. Chaperot, E. Dauler, S. Guerin, G. Jaeger, A. Muller, and A. Migdall. Calculating characteristics of noncollinear phase matching in uniaxial and biaxial crystals. *Opt. Eng.*, 39:1016, 2000.

[99] H. Di Lorenzo Pires, F. Coppens, and M. P. van Exter. Type-i spontaneous parametric down-conversion with a strongly focused pump. *Phys. Rev. A*, 83(3):033837, 2011.

[100] B. J. Pors. *Entangling light in high dimensions*. PhD thesis, University of Leiden, 2010.

[101] D. N. Klyshko. Combined EPR and two-slit experiments: Interference of advanced waves. *Phys. Lett. A*, 132(6-7):299–304, 1988.

[102] E. K. Tan, J. Jeffers, S. M. Barnett, and D. T. Pegg. Retrodictive states and two-photon quantum imaging. *Eur. Phys. J. D*, 22(3):495–499, 2003.

[103] E. K. Tan, J. Jeffers, S. M Barnett, and D. T Pegg. Retrodictive states and two-photon quantum imaging. *Eur. Phys. J. D*, 29(2):309–309, 2004.

[104] S. M. Barnett, D. T. Pegg, and J. Jeffers. Bayes' theorem and quantum retrodiction. *J. Mod. Optic.*, 47(11):1779–1789, 2000.

[105] T. B. Pittman, Y. H. Shih, D. V. Strekalov, and A. V. Sergienko. Optical imaging by means of two-photon quantum entanglement. *Phys. Rev. Lett.*, 52:R3429–R3432, 1995.

[106] T. B. Pittman, D. V. Strekalov, D. N. Klyshko, M. H. Rubin, A. V. Sergienko, and Y. H. Shih. Two-photon geometric optics. *Phys. Rev. A*, 53(4):2804–2815, 1996.

[107] H. Di Lorenzo Pires and M. P. van Exter. Near-field correlations in the two-photon field. *Phys. Rev. A*, 80(5):053820, 2009.

[108] H. Di Lorenzo Pires and M. P. van Exter. Observation of near-field correlations in spontaneous parametric down-conversion. *Phys. Rev. A*, 79:041801(R), 2009.

[109] N. K. Langford, R. B. Dalton, M. D. Harvey, J. L. O'Brien, G. J. Pryde, A. Gilchrist, S. D. Bartlett, and A. G. White. Measuring entangled qutrits and their use for quantum bit commitment. *Phys. Rev. Lett.*, 93(5):53601, 2004.

[110] B. Jack. *Entangling light in high dimensions*. PhD thesis, University of Glasgow, 2011.

[111] J. A. Davis, D. M. Cottrell, J. Campos, M. J. Yzuel, and I. Moreno. Encoding amplitude information onto phase-only filters. *Appl. Opt.*, 38(23):5004–5013, 1999.

[112] P.H. Eberhard. Background level and counter efficiencies required for a loophole-free Einstein-Podolsky-Rosen experiment. *Phys. Rev. A*, 47(2):747–750, 1993.

[113] D. T. Pegg, J. A. Vaccaro, and S. M. Barnett. Quantum-optical phase and canonical conjugation. *Journal of Modern Optics*, 37(11):1703–1710, 1990.

[114] D. T. Pegg and S. M. Barnett. Quantum optical phase. *J. Mod. Optic.*, 44(2):225–264, 1997.

[115] S. M. Barnett and D. T. Pegg. Quantum theory of rotation angles. *Phys. Rev. A*, 41(7):3427, 1990.

[116] S. Franke-Arnold, S. M. Barnett, E. Yao, J. Leach, J. Courtial, and M. J. Padgett. Uncertainty principle for angular position and angular momentum. *New J. Phys.*, 6:103, 2004.

[117] A. K. Jha, B. Jack, E. Yao, J. Leach, R. W. Boyd, G. S. Buller, S. M. Barnett, S. Franke-Arnold, and M. J. Padgett. Fourier relationship between the angle and angular momentum of entangled photons. *Phys. Rev. A*, 78:043810, 2008.

[118] J. P. Torres, A. Alexandrescu, and L. Torner. Quantum spiral bandwidth of entangled two-photon states. *Phys. Rev. A*, 68(5):050301, 2003.

[119] H. Di Lorenzo Pires, H. C. B. Florijn, and M. P. van Exter. Measurement of the spiral spectrum of entangled two-photon states. *Phys. Rev. Lett.*, 104(2):20505, 2010.

[120] M. P. van Exter, P. S. K. Lee, S. Doesburg, and J. P. Woerdman. Mode counting in high-dimensional orbital angular momentum entanglement. *Opt. Express*, 15(10):6431–6438, 2007.

[121] M. P. van Exter, A. Aiello, S. S. R Oemrawsingh, G. Nienhuis, and J. P. Woerdman. Effect of spatial filtering on the Schmidt decomposition of entangled photons. *Phys. Rev. A*, 74(1):012309, 2006.

[122] J. B. Pors, S. S. R. Oemrawsingh, A. Aiello, M. P. Van Exter, E. R. Eliel, G. W. van 't Hoff, and J.P. Woerdman. Shannon dimensionality of quantum channels and its application to photon entanglement. *Phys. Rev. Lett.*, 101(12):120502, 2008.

[123] T. Brougham and S. M. Barnett. Information communicated by entangled photon pairs. *Phys. Rev. A.*, 85:032322, 2012.

[124] J. Leach, E. Bolduc, D. J. Gauthier, and R. W. Boyd. The secure information capacity of photons entangled in high dimensions. *Phys. Rev. A*, 85:060304(R), 2012.

[125] J. P. Torres, Y. Deyanova, L. Torner, and G. Molina-Terriza. Preparation of engineered two-photon entangled states for multidimensional quantum information. *Phys. Rev. A*, 67:052313, 2003.

[126] C. I. Osorio, G. Molina-Terriza, and J. P. Torres. Correlations in orbital angular momentum of spatially entangled paired photons generated in parametric down-conversion. *Phys. Rev. A*, 77:015810, 2008.

[127] B. Jack, P. Aursand, S. Franke-Arnold, D. G. Ireland, J. Leach, S. M. Barnett, and M. J. Padgett. Demonstration of the angular uncertainty principle for single photons. *J. of Opt.*, 13:064017, 2011.

[128] D. Giovannini, F. Miatto, J. Romero, S. M. Barnett, J. P. Woerdman, and M. J. Padgett. Determining the dimensionality of bipartite orbital-angular-momentum entanglement using multi-sector phase masks. *New J. of Phys.*, 14:073046, 2012.

[129] D. N. Klyshko. A simple method of preparing pure states of an optical field, of implementing the Einstein–Podolsky–Rosen experiment, and of demonstrating the complementarity principle. *Soviet Physics Uspekhi*, 31:74, 1988.

[130] T. Markvart. The thermodynamics of optical étendue. *J. Opt. A*, 10:015008, 2008.

[131] A. Yariv. *Quantum Electronics*. Academic Press, 1989.

[132] M. Cirone. Entanglement correlations, Bell inequalities and the concurrence. *Phys. Lett. A*, 339:269274, 2005.

[133] S. M. Barnett and D. T. Pegg. Quantum theory of rotation angles. *Phys. Rev. A*, 41(7):3427, 1990.

[134] A. K. Jha, J. Leach, B. Jack, S. Franke-Arnold, S. M. Barnett, R. W. Boyd, and M. J. Padgett. Angular Two-Photon Interference and Angular Two-Qubit States. *Phys. Rev. Lett.*, 104(1):10501, 2010.

[135] W. K. Wootters. Entanglement of formation of an arbitrary state of two qubits. *Phys. Rev. Lett.*, 80(10):2245–2248, 1998.

[136] A. Vaziri, G. Weihs, and A. Zeilinger. Experimental two-photon, three-dimensional entanglement for quantum communication. *Phys. Rev. Lett.*, 89(24):240401, 2002.

[137] A. Vaziri, G. Weihs, and A. Zeilinger. Superpositions of the orbital angular momentum for applications in quantum experiments. *J. of Opt. B*, 4:S47, 2002.

[138] G. Molina-Terriza, J. P. Torres, and L. Torner. Management of the angular momentum of light: preparation of photons in multidimensional vector states of angular momentum. *Phys. Rev. Lett.*, 88(1):13601, 2001.

[139] D. V. Strekalov, A. V. Sergienko, D. N. Klyshko, and Y. H. Shih. Observation of two-photon ghost interference and diffraction. *Phys. Rev. Lett.*, 74(18):3600–3603, 1995.

[140] C. I. Osorio, G. Molina-Terriza, and J.P. Torres. Orbital angular momentum correlations of entangled paired photons. *J. Opt. A*, 11:094013, 2009.

[141] W. A. T. Nogueira, S. P Walborn, S. Pádua, and C. H. Monken. Generation of a two-photon singlet beam. *Phys. Rev. Lett.*, 92(4):43602, 2004.

[142] R. M. Gomes, A. Salles, F. Toscano, P. H. Souto Ribeiro, and S. P. Walborn. Quantum entanglement beyond gaussian criteria. *P Natl. Acad. Sci. U.S.A.*, 106:21517, 2012.

[143] A. E. Siegman. *Lasers*. CA: University Science Books, 1986.

[144] V. Delaubert, D. A. Shaddock, P. K. Lam, B. C. Buchler, H. A. Bachor, and D. E. McClelland. Generation of a phase-flipped gaussian mode for optical measurements. *J. Opt. A*, 4:393, 2002.

[145] I. Kimel and L. Elias. Relations between hermite and laguerre gaussian modes. *IEEE J. of Quantum Electron*, 29:00, 1993.

[146] M. Abramowitz and I. A. Stegun. *Handbook of mathematical functions*. Dover, 1965.

[147] S. P. Walborn, A. N. De Oliveira, S. Pádua, and C. H. Monken. Multimode Hong-Ou-Mandel interference. *Phys. Rev. Lett.*, 90(14):143601, 2003.

[148] M. J. Padgett and J. Courtial. Poincaré-sphere equivalent for light beams containing orbital angular momentum. *Opt. Lett.*, 24(7):430–432, 1999.

[149] G. C. G. Berkhout, M. P. J. Lavery, J. Courtial, M. W. Beijersbergen, and M. J. Padgett. Efficient sorting of orbital angular momentum states of light. *Phys. Rev. Lett.*, 105(15):153601, 2010.

[150] T. Vértesi, S. Pironio, and N. Brunner. Closing the detection loophole in Bell experiments using qudits. *Phys. Rev. Lett.*, 104(6):60401, 2010.

[151] A. K Pati, P. Parashar, and P. Agrawal. Probabilistic superdense coding. *Phys. Rev. A*, 72(1):012329, 2005.

[152] J. T. Barreiro, T. C. Wei, and P.G. Kwiat. Beating the channel capacity limit for linear photonic superdense coding. *Nat. Phys.*, 4(4):282–286, 2008.

[153] A. Schreiber, K. N. Cassemiro, V. Potoček, A. Gábris, P. J. Mosley, E. Andersson, I. Jex, and Ch. Silberhorn. Photons walking the line: A quantum walk with adjustable coin operations. *Phys. Rev. Lett.*, 104(5):50502, 2010.

[154] C. E. R. Souza and A. Z. Khoury. A Michelson controlled-not gate with a single-lens astigmatic mode converter. *Opt. Express*, 18(9):9207–9212, 2010.

[155] P. A. Schilpp. *Albert Einstein: Philosopher-Scientist*. Tudor, 1951.

[156] Z. Y. Ou, S. F. Pereira, H. J. Kimble, and K. C. Peng. Realization of the Einstein-Podolsky-Rosen paradox for continuous variables. *Phys. Rev. Lett.*, 68(25):3663–3666, 1992.

[157] M. D. Reid. Demonstration of the Einstein-Podolsky-Rosen paradox using nondegenerate parametric amplification. *Phys. Rev. A*, 40:913–923, 1989.

[158] J. F. Clauser, A. Shimony M. A. Horne, and R. A. Holt. Proposed Experiment to Test Local Hidden-Variable Theories. *Phys. Rev. Lett.*, 23:880–884, 1969.

[159] W. Perrie, A. J. Duncan, H. J. Beyer, and H. Kleinpoppen. Polarization correlation of the two photons emitted by metastable atomic deuterium: A test of Bell's inequality. *Phys. Rev. Lett.*, 54:1790–1793, 1985.

[160] L. Allen, J. Courtial, and M. J. Padgett. Matrix formulation for the propagation of light beams with orbital and spin angular momenta. *Phys. Rev. E*, 60:7497–7503, 1999.

[161] J. Leach, M. J. Padgett, S. M. Barnett, S. Franke-Arnold, and J. Courtial. Measuring the orbital angular momentum of a single photon. *Phys. Rev. Lett.*, 88(25):257901, 2002.

[162] N. D. Mermin. The best version of bell's theorem. *Ann. N.Y. Acad. Sci.*, 755(1):616–623, 1995.

[163] N. D. Mermin. Quantum mysteries refined. *Am. J. Phys.*, 62:880, 1994.

[164] J. A Carlson, M. D Olmstead, and M. Beck. Quantum mysteries tested: An experiment implementing hardys test of local realism. *Am. J. Phys.*, 74:180, 2006.

[165] D. Boschi, S. Branca, F. De Martini, and L. Hardy. Ladder proof of nonlocality without inequalities: Theoretical and experimental results. *Phys. Rev. Lett.*, 79(15):2755–2758, 1997.

[166] G. Vallone, I. Gianani, E. B. Inostroza, C. Saavedra, G. Lima, A. Cabello, and P. Mataloni. Testing Hardys nonlocality proof with genuine energy-time entanglement. *Phys. Rev. A*, 83(4):042105, 2011.

[167] M. R. Dennis, R. King, B.Jack, K. O'Holleran, and M. J. Padgett. Isolated optical vortex knots. *Nat. Phys.*, 6:118–121, 2011.

[168] S. Gröblacher, T. Paterek, R. Kaltenbaek, et al. An experimental test of non-local realism. *Nature*, 446(7138):871–875, 2007.

[169] T. Paterek, A. Fedrizzi, S. Gröblacher, T. Jennewein, M. Żukowski, M. Aspelmeyer, and A. Zeilinger. Experimental test of nonlocal realistic theories without the rotational symmetry assumption. *Phys. Rev. Lett.*, 99(21):210406, 2007.

[170] C. Branciard, A. Ling, N. Gisin, C. Kurtsiefer, A. Lamas-Linares, and V. Scarani. Experimental falsification of Leggett's nonlocal variable model. *Phys. Rev. Lett.*, 99(21):210407, 2007.

[171] C. Branciard, N. Brunner, N. Gisin, C. Kurtsiefer, A. Lamas-Linares, A. Ling, and V. Scarani. Testing quantum correlations versus single-particle properties within Leggett's model and beyond. *Nature Phys.*, 4(9):681–685, 2008.

[172] M. D Eisaman, E. A Goldschmidt, J. Chen, J. Fan, and A. Migdall. Experimental test of nonlocal realism using a fiber-based source of polarization-entangled photon pairs. *Phys. Rev. A*, 77(3):32339, 2008.

[173] A. Aspect. Quantum mechanics: To be or not to be local. *Nature*, 446(7138):866–867, 2007.

[174] R. Y. Chiao and J. C. Garrison. Realism or locality: Which should we abandon? *Foundations of Physics*, 29(4):553–560, 1999.

[175] M. V. Berry and M. R. Dennis. Knotted and linked phase singularities in monochromatic waves. *Proc. Royal Soc. A*, 457:2251–2263, 2001.

[176] J. Masajada and B. Dubik. Optical vortex generation by three plane wave interference. *Opt. Comm.*, 198:21–27, 2001.

[177] K. O'Holleran, M. R. Dennis, F. Flossmann, and M. J. Padgett. Fractality of light's darkness. *Phys. Rev. Lett.*, 100:53902, 2008.

[178] R. Ghosh, C. K. Hong, Z. Y. Ou, and L. Mandel. Interference of two photons in parametric down conversion. *Phys. Rev. A*, 34(5):3962–3968, 1986.

[179] M. V. Berry and M. R. Dennis. Knotting and unknotting of phase singularities: Helmholtz waves, paraxial waves and waves in 2 + 1 dimensions. *J. Phys. A: Math. Gen.*, 34:887788, 2001.

[180] D. Kawase, Y. Miyamoto, M. Takeda, K. Sasaki, and S. Takeuchi. Observing quantum correlation of photons in Laguerre-Gauss modes using the Gouy phase. *Phys. Rev. Lett.*, 101(5):50501, 2008.

[181] J. F. Clauser, M. A. Horne, A. Shimony, and R.A. Holt. Proposed experiment to test local hidden-variable theories. *Phys. Rev. Lett.*, 23(15):880–884, 1969.

[182] C. H. van der Wal, A. C. J. Ter Haar, F. K. Wilhelm, R. N. Schouten, C. Harmans, T. P. Orlando, S. Lloyd, and J. E. Mooij. Quantum superposition of macroscopic persistent-current states. *Science*, 290:773–777, 2000.

[183] N. Gullo, S. McEndoo, T. Busch, and M. Paternostro. Vortex entanglement in Bose-Einstein condensates coupled to Laguerre-Gauss beams. *Phys. Rev. A*, 81(5):053625, 2010.

[184] O. M. Auslaender, L. Luan, E. W. J. Straver, J. E. Hoffman, N. C. Koshnick, E. Zeldov, D. A. Bonn, R. Liang, W. N. Hardy, and K. A. Moler. Mechanics of individual isolated vortices in a cuprate superconductor. *Nat. Phys.*, 5:35–39, 2009.

[185] K.T. Kapale and J.P. Dowling. Vortex phase qubit: Generating arbitrary, counterrotating, coherent superpositions in Bose-Einstein condensates via optical angular momentum beams. *Phys. Rev. Lett.*, 95:173601, 2005.

[186] R. Pugatch, M. Shuker, O. Firstenberg, A. Ron, and N. Davidson. Topological stability of stored optical vortices. *Phys. Rev. Lett.*, 98(20):203601, 2007.

[187] C. Nayak, S. H. Simon, A. Stern, M. Freedman, and S. D. Sarma. Non-abelian anyons and topological quantum computation. *Rev. Mod. Phys.*, 80(3):1083, 2008.

[188] W. J. Firth and D. V Skryabin. Optical solitons carrying orbital angular momentum. *Phys. Rev. Lett.*, 79(13):2450–2453, 1997.